A THEORY FOR THE PERFORMANCE OF HOT-FILM SHEAR STRESS PROBES

by

Kenneth Michael Kalumuck

B.S. Purdue University
(1974)

Certificate of Post-Graduate Study in Engineering
Cambridge University (1975)

Mechanical Engineer and S.M., Massachusetts Institute of Technology
(1979)

Submitted to the Department of Mechanical Engineering
in Partial Fulfillment of
of the Requirements
for the Degree of

DOCTOR OF PHILOSOPHY

at the

MASSACHUSETTS INSTITUTE OF TECHNOLOGY

May, 1983

Signature of Author _____
Department of Mechanical Engineering
May 1983

Certified by _____
Thesis Supervisor

Accepted by _____
Chairman, Department Committee on Graduate Studies

A THEORY FOR THE PERFORMANCE OF HOT-FILM SHEAR STRESS PROBES

by

Kenneth Michael Kalumuck

Submitted to the Department of Mechanical Engineering
on May 6, 1983 in partial fulfillment of the
requirements for the Degree of Doctor of Philosophy

ABSTRACT

Wall shear stress affects drag, heat and mass transfer rates, flow separation, and fluid energy losses. Its accurate measurement is, however, difficult. Flush-mounted hot-film probes can be used to measure local wall shear stress even in complicated geometries without disturbing the flow. Their extensive use is currently limited by the need for tedious calibration and by an absence of an adequate *a priori* method of design evaluation.

A comprehensive three-dimensional theory for flush-mounted hot-film probes is presented. The theory considers a probe of arbitrary shape, flush-mounted on a thermally-conducting plane substrate, possessing an arbitrary heat source distribution, and exposed to a steady uniform incompressible shear flow. The complete three-dimensional coupled fluid and substrate energy equations are solved by a combined analytic and numerical Fourier transform technique to obtain selected temperature and heat flux distributions. The effects of wide ranges of Peclet number, substrate conductivity, and geometry are investigated. Predictions show excellent agreement with limiting value theories and are consistent with existing experimental data.

An accurate approximation of probe heat transfer is derived from the observation that coupling between the fluid and substrate heat transfer is weak. A simple analysis indicates that spatial variation of substrate conductivity can influence probe sensitivity to shear. Common experimental probe configurations can produce calibration curves that exhibit this effect.

Applications to general problems of heat or mass transfer to a shear flow over a wall with surface sources are discussed.

Thesis Supervisor: Peter W. Huber

Title: Associate Professor of Mechanical Engineering

Acknowledgements

Many more people have influenced this work or touched my life than I can possibly recount here. To everyone who has been a part of this effort, I extend a deep-felt thanks.

I wish to thank my thesis committee for the aid and support both technical and moral they generously provided. It has been both my benefit and pleasure to have worked with them. I greatly appreciate Peter Huber's willing supervision, insight, advice, and encouragement. I am indebted to Forbes Dewey for continued optimism, a broad perspective, and many helpful discussions. I am grateful to Patrick Leehey for insights into mathematical complexities and discussions of hot-film probes from a user's point of view.

Others who have helped guide me on my wanderings include Tom Jasinski, Mike Jcos, Tony Patera, Judi Steciak, and Don Rolph. The task of preparing this document was significantly lightened by Maureen Hayes. For this and, more importantly, for her unwavering support, she has my deepest gratitude.

I would like to thank my parents, Ann Kalinowski, Jim Cech, Norm Decker, Dave Barr, Mark Moeller, Mike Foycik, Jung-Hoon Chun, Adele Maurer, Rick Vilim, Dick Fenner, Jason Harry, Jake Rosenzweig, and Steve Bussolari for being part of this. I would also like to thank all the members past and present of the fluids and heat transfer labs and of the various incarnations of the Calorics Softball Club for

providing me much I want to remember.

I am grateful to Donna Wilker for "processing" the countless equations and other typing that the "word-processor" would not, could not, or should not, and to the "word-processor" for curbing its previously ravenous appetite for disks. Finally, I would like to acknowledge the support of this research by the Office of Naval Research and the National Institute of Health.

Table of Contents

List of Figures

List of Tables

Nomenclature

a	streamwise probe half length
A	parameter in straight line fit to probe calibration curve, Section 4.5
Ai	Airy function
Ai'	first derivative of Ai
b	spanwise probe half width
b/a	probe aspect ratio
B	parameter in straight line fit to probe calibration curve, Section 4.5
B_m	value of B measured by experiment
B_t	value of B predicted by theory
c	fluid specific heat
G	a Green's function, Chapter 2
Gr	Grashoff number, Section 4.7
h	a heat transfer coefficient
$H(\xi)$	Heaviside function of ξ
H	heat transfer coefficient for total heat transfer from the probe
H_x	local value of H
i	$\sqrt{-1}$
k	thermal conductivity
K	$\equiv k_s/k_f$, the conductivity ratio
K_{eff}	effective average value of K defined in Section 4.5
L^*	characteristic length (dimensional)
L^*_{eff}	effective probe length inferred from probe calibration curve, Section 4.5
L_p	probe streamwise length
L^*_T	upstream thermal penetration length, Section 4.5
Nu	$= \dfrac{P^*_s \cdot 2a^*}{4a^*b^*k_f\bar{T}^*_p}$, probe Nusselt number for total heat transfer

Nu_{fs}	= Nu - Nu(Pe=0), flow-sensitive portion of Nu
$\widetilde{Nu}_{fs}$	a best fit value of Nu_{fs} averaged over K; a function only of Pe and b/a
Nu_{oo}	= Nu(Pe=0, K=0); a function only of b/a
p	Fourier transform variable in x direction
P_s^*	total probe power dissipation
$Pe \equiv \frac{sL_p^{*2}}{\alpha}$	the Peclet number
$Pr \equiv \frac{\nu}{\alpha}$	the Prandtl number
$\widetilde{Pr}$	modified Prandtl number; defined in equation (4.5)
q	Fourier transform variable in the z direction
$q_f(x,z)$	fluid heat flux per unit area in the "+y" direction; equation (2.36a)
$q_s(x,z)$	substrate heat flux per unit area in the "-y" direction; equation (2.36b)
$Q(x,z)$	probe heat generation rate distribution (per unit planform area)
Re	Reynolds number; defined as used on a case by case basis
$s \equiv \frac{dy}{dy}\Big\|_{y=0}$	fluid shear at the wall
t*	probe film thickness in y direction
T	temperature measured above ambient
u	fluid velocity in x direction
W*	volumetric heat generation rate
x	streamwise coordinate
y	coordinate normal to the wall
z	spanwise coordinate

$\alpha = k_f/\rho c$	fluid thermal diffusivity; α also used to denote the probe film temperature coefficient of resistivity in Section 4.6
$\delta(\xi)$	delta function of argument ξ
δ_T	thermal boundary layer thickness
δ_p, δ_q	numerical discretization step sizes
η	argument of Ai; defined in equation (2.19)
η_0	$\eta(y=0)$
μ	fluid dynamic viscosity
$\nu = \mu/\rho$	fluid kinematic viscosity
ρ	fluid density; ρ also used to denote the probe film resistivity in Section 4.6
$\tau_w = \mu s$	fluid shear stress at the wall

Subscripts:

f	fluid
NC	natural convection
p	probe
rad	radiation
s	substrate
∞	infinity

Superscripts:

*	dimensional quantities

$( )^+ = ( )\sqrt{\frac{\tau_w/\rho}{\nu}}$, $( ) = x^*, y^*, z^*$; coordinates expressed in "wall-layer units"

Other:

$\hat{(\ )}$	denotes the two-dimensional Fourier transform of ( ) as defined in equation (2.12)
$\bar{(\ )}$	average value of ( )

1. INTRODUCTION

The shear stress exerted by a flowing fluid on a solid body is one of the fundamental quantities characterizing that flow. Knowledge of this stress is critical to the prediction of drag, pressure drop, fluid energy loss, heat and mass transfer rates, flow separation, and cavitation. Comparison of local shear stress predictions with measured values provides a good test of the accuracy of various theoretical and numerical flow analysis techniques.

Unfortunately, the accurate measurement of wall shear stress remains a difficult task. There exist several excellent comprehensive reviews of the various measurement techniques employed. (See, for example, Winter 1977 and Hanratty and Campbell 1982.) One potentially valuable and versatile instrument for shear stress measurement is the flush-mounted hot-film probe. The use of hot-film probes has a number of advantages. Measurements can be made without significant disturbance to the flow of both liquids and gases in complicated and relatively inacessible flow geometries. Neither the fluid nor the wall need be transparent.

There are, however, currently a number of impediments to the facile and extensive use of hot-films. These include the need for a tedious calibration of each individual probe in conditions as identical as possible to those in which measurements are to be made, the absence of a method of

a priori probe design evaluation, and the lack of an adequate understanding of the details of the physics that govern probe performance. These limitations are true in varying degrees for flows of all levels of complexity. They are present in steady laminar flow and are even more limiting in unsteady and turbulent flows. Central to all of these deficiencies is the absence of a comprehensive theory capable of accurately predicting the details of probe performance over wide ranges of operating and design conditions.

In this paper we develop and apply the first such comprehensive three-dimensional theory for the prediction of probe performance in steady flows.

The fundamental concept underlying the operation of a hot-film probe is simple: a fluid flowing over a heated surface transfers heat away from that surface in an amount related to the shear stress exerted by the fluid on that surface. The detailed quantification of this relationship is the major emphasis of this work.

A typical hot-film shear stress probe consists of a thin metal film deposited on an electrically insulating substrate. In many current designs (figure 1.1), the film is rectangular, has dimensions of order 1mm or less, and is electrically heated by a current supplied by leads attached to either end of the film. The leads are connected to a standard anemometer package of the type used to operate hot-wire velocity probes. The hot-film probe is mounted flush with the surface on which

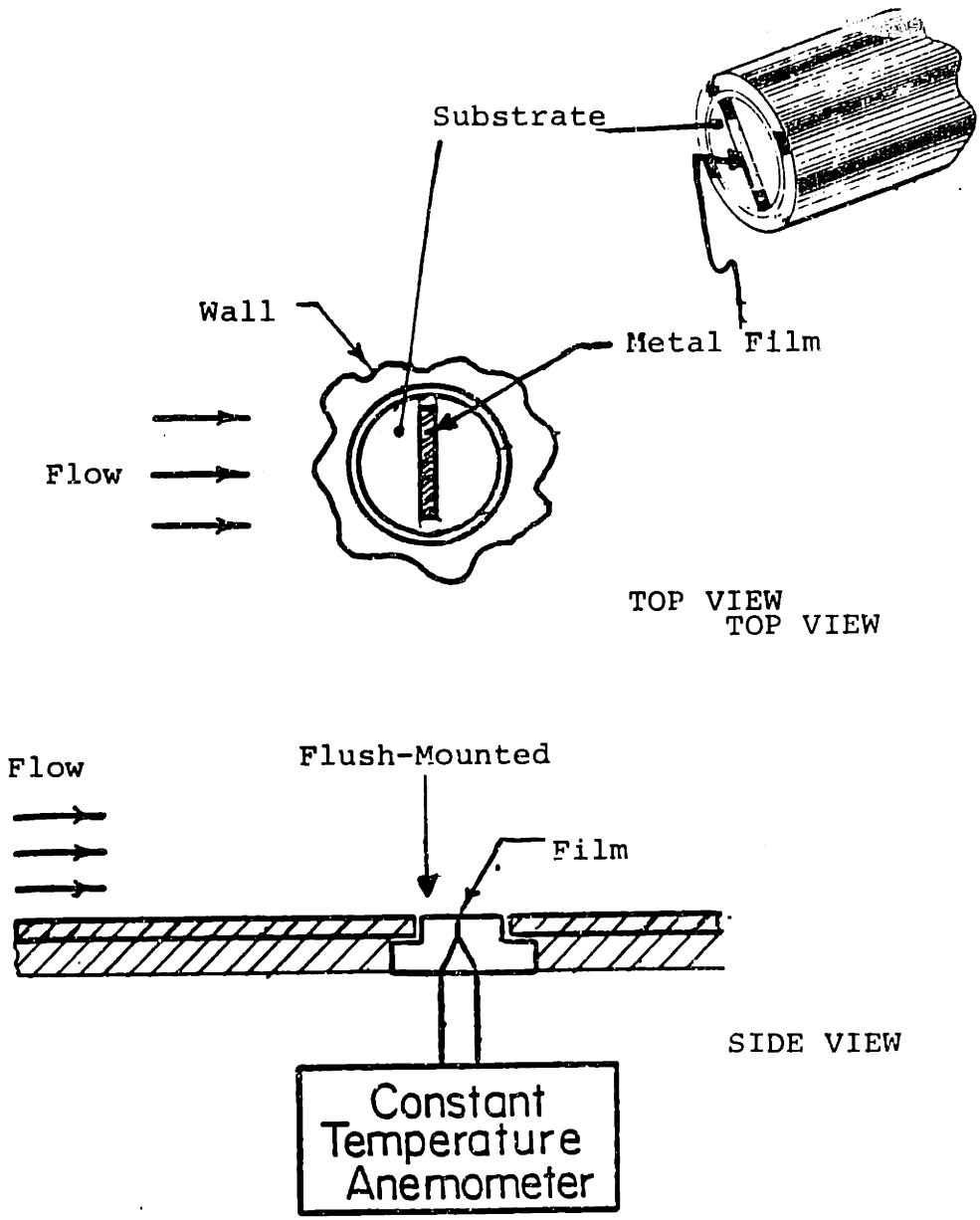

Figure 1.1 Typical hot-film probe configuration. (Taken in part from Hanratty and Campbell 1982 and Blackwelder 1981.)

measurements are desired either by affixing it to the surface or by inserting it in a hole machined in the surface. The probe is usually operated at a temperature kept constant with time. The current, and thus the power (equal to the heat transferred away from the probe) needed to maintain the probe temperature, varies with the shear stress, or, more precisely, the local fluid velocity field. By assuming similar velocity fields for a given flow situation, the specification of the fluid mechanics reduces to the determination of property values and of one parameter: the velocity gradient or shear at the wall $s=(du/dy)_0$. The shear stress τ_w is then:

$$\tau_w = \mu s, \qquad (1.1)$$

where μ is the dynamic viscosity of the fluid.

The procedure currently used for the quantitative measurement of shear stress by hot-films is to place the probe in a flow with a known shear stress under conditions closely matching those for which measurements are to be made. (Not only must the flow conditions be similar, but the thermal properties of the wall in the vicinity of the probe also need to be duplicated.) The probe power consumption is monitored as the known shear stress is varied. This produces a calibration curve whose essential features are schematically depicted in figure 1.2. The methods of determining the stress of the known shear flow are many. A laminar flow whose

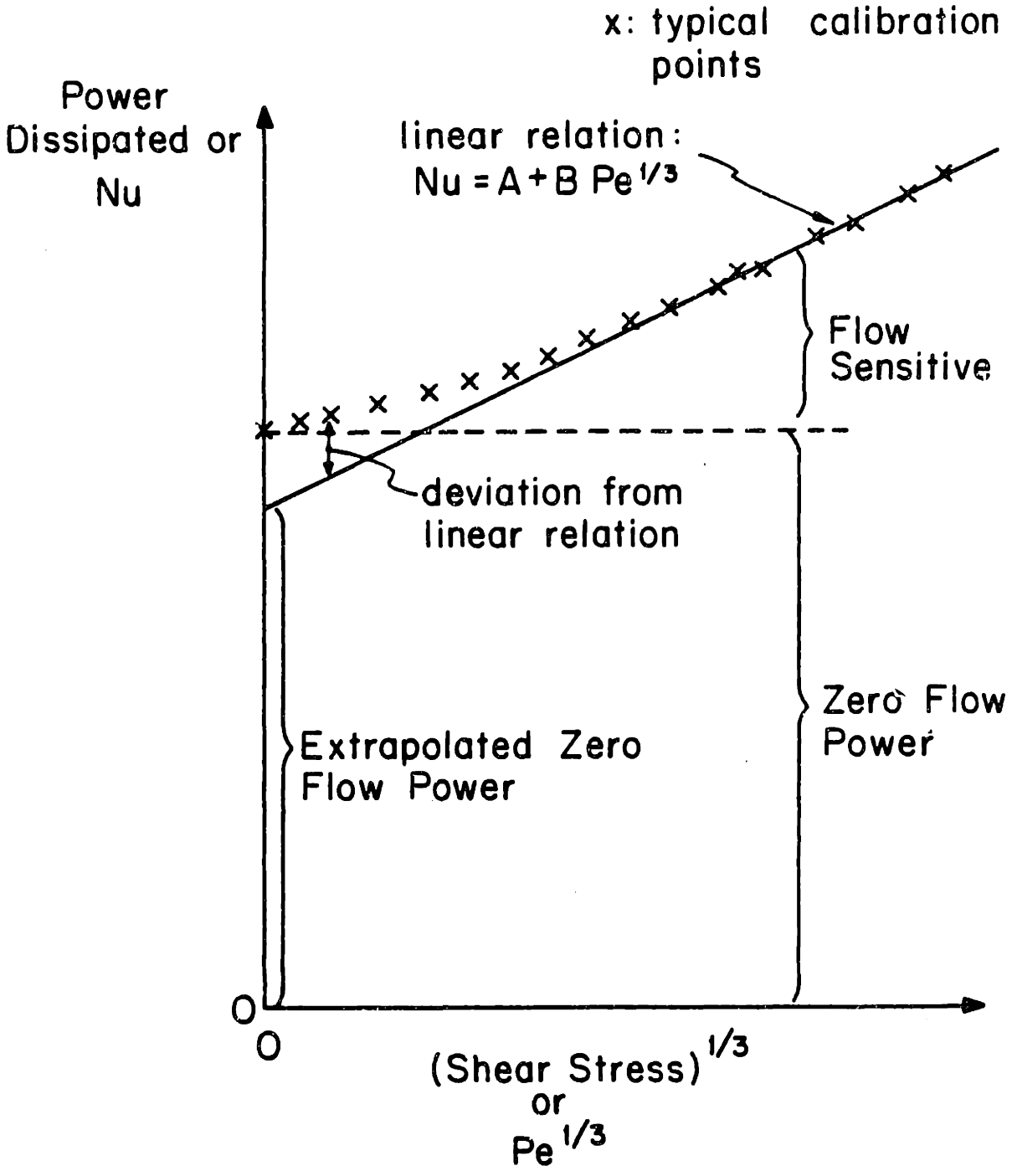

Figure 1.2 Features of typical hot-film calibration curve.

properties are well known such as a pipe or Couette flow can be used; a different shear stress measuring device may be employed; or a global force balance can be made relating a measured pressure drop to a presumed uniform distribution of shear stress over the flow boundaries.

The calibration curve is commonly expressed as a plot of the power dissipated by the probe (or some quantity proportional to it such as the square of the voltage drop across the film) vs. the one-third power of the shear stress. When expressed in this manner, there is usually a linear region of the curve at large values of the shear, as illustrated in figure 1.2. Extrapolation of this line to zero shear yields a positive value of power dissipation. Actual measurements taken at low shear rates produce a curve that deviates from the simple linear relationship (figure 1.2). The measured value of the power dissipation at zero shear is larger than the linearly extrapolated value. The observed linear relation is based on a balance between two modes of heat transfer: streamwise convection and conduction normal to the wall (a simple boundary layer behavior). Departures from this linear behavior are due largely to the influence of other modes of heat transfer and of geometry.

Probe calibration curves can be expressed more universally by proper nondimensionalization of the power dissipation (heat transfer) and the shear stress. The appropriate dimensionless groups for these quantities are the

Nusselt number for total heat transfer and the Peclet number, respectively. These are rigorously defined in Chapter 2.

From a practical standpoint, one is interested in the sensitivity of this device. The measured quantity (power) varies only as the one-third power of shear stress - a rather weak variation. This low resolution (even lower in the non-linear region) is an inherent drawback of hot-films. However, other techniques possess other limitations, and this resolution problem can be dealt with. As a first approximation, the calibration curve can be characterized by two parameters: the slope of the linear region which gives the heat transfer sensitivity to shear, and the value of the power dissipation at zero shear. This latter quantity can be viewed as a background signal or "d.c. bias" which does not provide information useful in determining the shear stress. We have found it to be a strong function of the relative fluid and substrate thermal conductivities and of probe geometry. For many cases of practical interest, this "bias" is very large. For example, for an air flow and a glass substrate, the flow sensitive portion may be only 1-2% of the measured power dissipation.

The linear relation between heat transfer and the one-third power of the shear stress can be obtained analytically by considering a fluid with a uniform shear (i.e., a linear velocity profile) and a heated strip that is very narrow in the streamwise direction and infinitely long in

the spanwise direction. Convection then balances conduction into the fluid from the strip. The relation can be obtained from a similarity analysis (see, for example, Ling 1963) or from an integral analysis of the thermal boundary layer (see, for example, Bellhouse and Schultz 1966). Here, we present a simple derivation based on an order of magnitude analysis.

Consider the conditions depicted in figure 1.3: a fluid of thermal diffusivity α flows over a heated surface with a velocity given by u=sy where s is the velocity gradient or shear at the surface. A thermal boundary layer begins at the upstream edge of the heated region (x=0). Its thickness at any location is denoted by $\delta_T(x)$. We then have

$$\delta_T^2 = \alpha t ,$$

where t is the time for thermal diffusion to proceed a distance . This time is the time it takes the fluid at y=(x) to traverse the distance x. Thus:

$$t = \frac{x}{u} = \frac{x}{s\delta_T} ;$$

$$\delta_T^2 \sim \frac{\alpha x}{s\delta_T} ;$$

and

$$\delta_T \sim \left(\frac{\alpha x}{s}\right)^{1/3} .$$

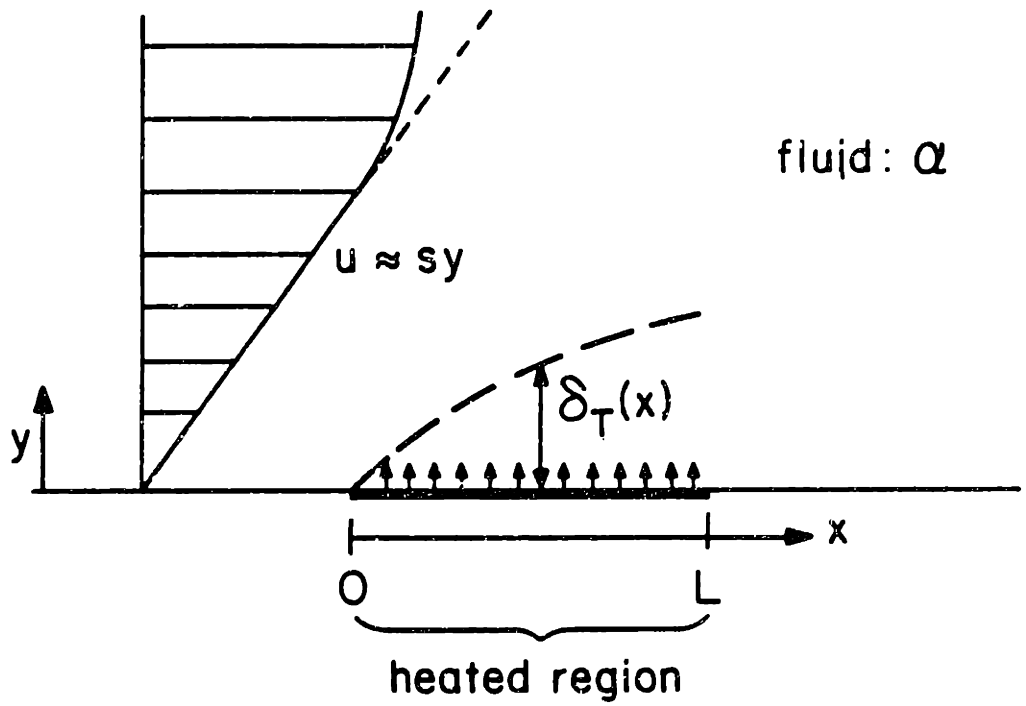

Figure 1.3 Thermal boundary layer growth in a uniform shear flow.

The temperature gradient at y=0 and thus the heat transfer q varies inversely with thermal boundary layer thickness:

$$q \sim \frac{1}{\delta_T} \sim \left(\frac{s}{\alpha x}\right)^{1/3},$$

or, recalling (1.1):

$$q \sim \left(\frac{\tau_w}{\alpha x}\right)^{1/3}.$$

Thus the one-third power relation is obtained.

Shear stress measurements can also be made using electrochemical probes which, conceptually, are very similar to hot-film probes. They rely on a relationship between shear stress and the transfer of mass from a probe via an electrochemical reaction rather than the transfer of heat. Analytically, this results in an identical set of governing equations in the fluid. The major difference is the lack of participation by the substrate in the transfer process. Thus, much of the analysis presented in this work is also applicable to the performance of these mass transfer probes. (See, for example, Hanratty and Campbell, 1982.)

The heat transfer - fluid shear relation is complicated by geometric effects and the presence of the thermally conducting substrate. A significant portion of the heat generated by the probe flows directly into the substrate and not directly to the fluid. (In many applications, this mode

of heat transfer dominates.) Heat is also exchanged between the substrate and the fluid surrounding the probe. Probe performance thus depends upon the coupled effects of convection in the fluid and three-dimensional conduction in both the fluid and the substrate.

Previous analyses of probe performance have been primarily confined to rectangular probes or probes of infinite spanwise extent, although other geometries have been employed in practice and may offer advantages in various flow situations. The introduction of other probe geometries is hindered by an inability to predict their performance. Thus, we present a theory capable of analyzing probes of arbitrary geometry. Even for steady flows, no theory has yet dealt with both convection in the fluid and conduction in both media for probes of arbitrary geometry. A summary of the characteristics of several previously developed steady flow models is presented in table 1.1.

Examination of table 1.1 shows that the most common assumptions of previous theories are two-dimensionality and an adiabatic substrate. These neglect perhaps the two strongest influences on probe performance. In some of the earliest applicable work, Leveque (1928) obtained a similarity solution for flow over a heated uniform temperature section of an otherwise adiabatic wall. He considered only two modes of heat transfer - fluid conduction normal to the wall and convection parallel to it. Ling (1963) expanded upon this

Model	Geometry	Streamwise conduction	Substrate conductivity	Probe condition*
Leveque (1928)	2-d	-	-	U T
Ling (1963)	2-d	x	-	U T
Tanner (1967)	pseudo 3-d	-	x	U Q; rectangular
Spence & Brown (1968)	2-d	-	-	U T; quadratic velocity profile
Davies & Kimber (1972)	2-d	x	x	U Q
Ackerberg, et. al. (1978)	2-d	x	-	U T; small Peclet number
Pardo (1980)	2-d	x	x	U T
Current work	3-d	x	x	arbitrary shape and source distribution

*U T : uniform temperature
U Q : uniform heat source

Table 1.1 Steady Flow Hot-Film Models.

work by including streamwise fluid conduction effects in the leading and trailing edge regions. Both models apply only to high Peclet number flows. Ackerberg, et. al. (1978) analyzed flows at low Peclet numbers. Davies and Kimber (1972) and Pardo (1980) developed two-dimensional models that include the effects of substrate conduction. Tanner (1967), in probably the most comprehensive work to date, included the effects of three-dimensional substrate conduction, but neglected both streamwise and spanwise conduction in the fluid thus essentially combining a three-dimensional substrate model and a two-dimensional large Peclet number fluid analysis. Spence and Brown (1968) investigated the effects of a streamwise pressure gradient by incorporating a quadratic velocity profile for flow over an adiabatic wall.

The theory presented in this paper considers an arbitrarily shaped probe (or set of probes) flush-mounted on a plane thermally conducting substrate, possessing an arbitrary heat source distribution, and exposed to a steady uniform incompressible shear flow. We employ the complete, three-dimensional fluid and substrate energy equations coupled through their associated boundary conditions. These are solved to obtain detailed temperature and heat flux distributions from which probe performance measures such as total power consumption and average probe temperature can be calculated. The procedure entails Fourier transformation of the governing equations, analytic solution in wavenumber

space, and numerical inversion. Solutions can be limited to any plane parallel to the surface, thereby decreasing the computational work. The results of a parametric study spanning several orders of magnitude of the governing parameters are presented in Chapter 3. This study highlights the importance of properly accounting for the effects of probe geometry, substrate conduction, and three-dimensional fluid conduction. The results are discussed and compared with the predictions of other models and experimental data in Chapter 4. We have found that for certain conditions probe performance can be predicted by a simplifying approximation that decouples the calculation of heat transfer to the fluid from that to the substrate.

One of the major disagreements between existing theory and measurements is the sensitivity of heat transfer to shear - i.e., the slope of probe calibration curves. Theoretical predictions are typically low by a factor of two to three. This discrepancy has been almost universally attributed to conduction in a simple substrate increasing the "effective length" of the probe in the streamwise direction. (See, for example, Brown 1967 or Murthy and Rose 1978.) Our investigations show that conduction through a homogeneous substrate does influence the shear sensitivity but can explain only part of the deviation of previous theory from measured values. However, a survey of the typical methods of probe use reveals that the substrate is usually far from homogeneous due

to the mounting of the probe within a wall of thermal conductivity different than that of the probe substrate, and attempts to thermally isolate the probe from the wall by layers of various "insulating" materials, air gaps, etc. A simple analysis (Chapter 4) shows that the effect of a streamwise variation in substrate conductivity is to create a flow-sensitive average or "effective" conductivity which qualitatively accounts for the observed calibration curve slopes.

Our investigations have produced insights into the desirable features of probes in steady flows. They also point to directions for both analysis and design of probes to operate in unsteady and turbulent flows. The transport of mass and vorticity in shear flows represent problems precisely analogous to the transport of heat and, thus, are amenable to solution by our theory. Due to the linearity of the governing equations and the arbitrariness of the source geometry and distribution, our theory should be applicable to a broad class of problems including those of generalized heat and mass transfer with surface sources, multiple film probes, and heated wires imbedded in the surface. Such capabilities and various possible enhancements to the technique are discussed in Chapter 5.

2. Analysis

2.1 Physical Model

Our model is designed to deal with flush-mounted probes of arbitrary planform geometry, and to account for convection in the fluid and diffusion in all directions in both the fluid and the substrate. We model the probe as a heat source of arbitrary but specified distribution and geometry located on a plane conducting wall (figure 2.1). The fluid above the probe flows with a uniform shear - i.e., a linear velocity profile. This assumption and the inclusion of nonlinear velocity profiles are discussed in Section 5.2. The governing equations are the three-dimensional fluid and solid energy equations:

$$\nabla^{*2} T_f^* - \frac{s}{\alpha} y^* \frac{\partial}{\partial x^*} T_f^* = 0, \quad y^* \geq 0 \tag{2.1}$$

$$\nabla^{*2} T_s^* = 0, \quad y^* \leq 0 \tag{2.2}$$

where

$$\nabla^{*2} = \frac{\partial^2}{\partial x^{*2}} + \frac{\partial^2}{\partial y^{*2}} + \frac{\partial^2}{\partial z^{*2}},$$

s = fluid velocity gradient ($u^* = sy^*$),

u = fluid velocity in the x direction,

T = temperature measured above ambient,

$\alpha = k_f/\rho c$, fluid thermal diffusivity,

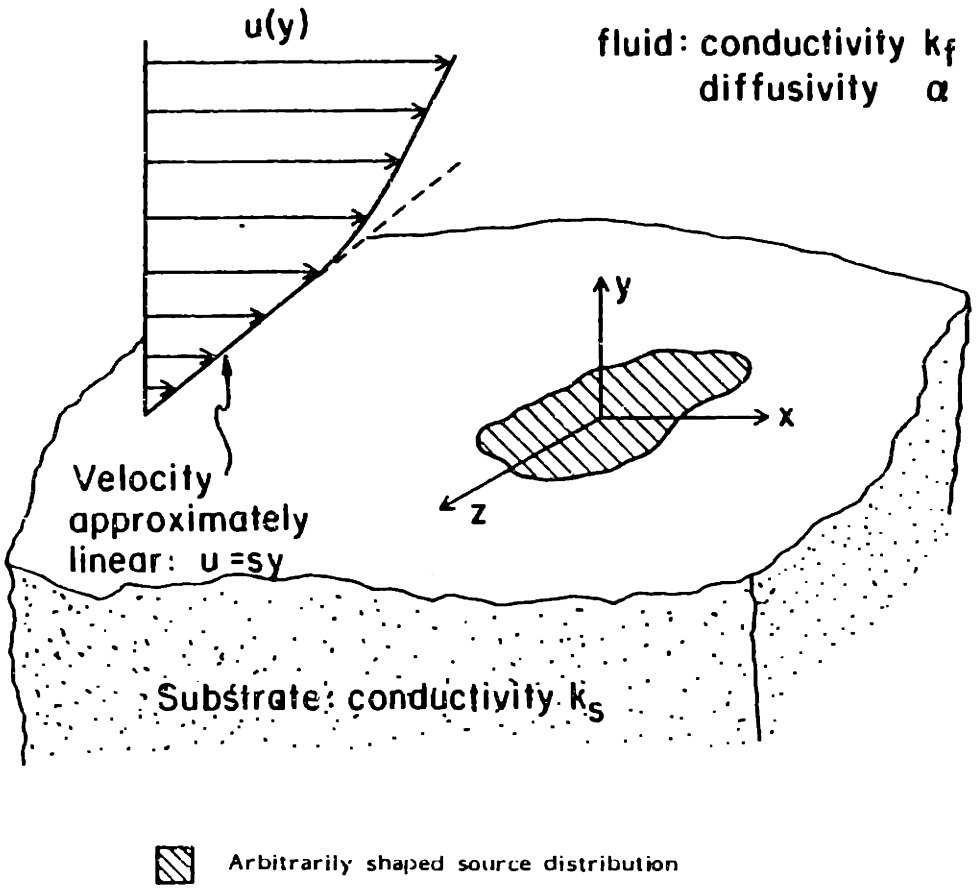

Figure 2.1 Idealized arbitrarily-shaped hot-film probe and its environment.

k_f = fluid thermal conductivity,

ρ = fluid density,

c = fluid specific heat,

* : denotes dimensional quantities,

f : as a subscript denotes fluid quantities, and

s : as a subscript denotes solid (substrate) quantities.

The temperature field is continuous at the fluid-solid interface. The heat flux is also continuous at this interface, except at the probe which acts as a source of heat. Thus:

$$T_f^* = T_s^* \quad \text{at } y^* = 0 \tag{2.3}$$

$$k_s \frac{\partial T_s^*}{\partial y^*} - k_f \frac{\partial T_f^*}{\partial y^*} = Q^* (x^*, z^*) \text{ at } y^* = 0 \tag{2.4}$$

where k is the thermal conductivity and Q* is the arbitrtary (but specified) probe heat source distribution. To impose (2.3) across the probe, we assume that the heated film thickness in the y* direction is vanishingly small and that there is no temperature drop across the probe - i.e., the thermal conductivity of the probe film is infinite. The validity of these assumptions is discussed in Section 4.6. At sufficiently large distances from the probe, the temperature must attain the ambient value, or

$$T_f^*,\ T_s^* \to 0 \text{ as } x^*,\ y^* \text{ or } z^* \to \pm\infty \tag{2.5}$$

These equations can be cast in a form more amenable to analysis by appropriate nondimensionalization. We define

$$L^* \equiv \sqrt{\alpha/s}$$

$$P_s^* \equiv \int_{-\infty}^{\infty}\int_{-\infty}^{\infty} Q^*\, dx^*\, dz^*$$

where L^* is a characteristic length for thermal diffusion in the fluid and P_s^* is the total power output of the probe. We introduce the dimensionless quantities:

$$x = x^*/L^*,\quad y = y^*/L^*,\quad z = z^*/L^*$$

$$T = T^* k_f L^*/P_s^*$$

$$K = k_s/k_f$$

$$Q(x,z) = Q^*(x^*,z^*) \cdot L^{*2}/P_s^*$$

Equations (2.1)-(2.5) can now be expressed as:

$$\nabla^2 T_f - y\frac{\partial T_f}{\partial x} = 0,\quad y \geq 0 \tag{2.6}$$

$$\nabla^2 T_s = 0,\quad y \leq 0 \tag{2.7}$$

$$T_f = T_s,\quad y = 0 \tag{2.8}$$

$$K\frac{\partial T_s}{\partial y} - \frac{\partial T_f}{\partial y} = Q(x, z),\quad y = 0 \tag{2.9}$$

$$T_f,\ T_s \to 0 \quad \text{as } x,\ y,\ z \to \pm\infty. \tag{2.10}$$

The solution of (2.6)-(2.10) depends only on the conductivity ratio K and the source distribution Q(x,z). The shear s is part of the definition of a characteristic diffusion length (equal to $\sqrt{\alpha/s}$). Other parameters are introduced when the form of Q(x,z) is specified. The use of as the characteristic length rather than the probe streamwise length - as is more conventional - leads to a more generalized solution. (This characteristic length is used by Ling (1963) for leading and trailing edge solutions where the fluid streamwise conduction term is retained.) Use of this length scale renders (2.6) and (2.7) independent of probe design. The influence of a particular probe is introduced through boundary condition (2.9).

The use of a probe dimension as a length scale introduces a parameter into the fluid domain governing equation. If the characteristic dimension chosen is the streamwise probe length (as used by Tanner, 1967, for example), the governing equation for the fluid analogous to (2.6) is

$$\nabla^2 T_f - \left(\frac{s L_p^{*2}}{\alpha}\right) y \frac{\partial}{\partial x} T_f = 0. \tag{2.11}$$

The solution of (2.11) depends on the parameter

$$\frac{s L_p^{*2}}{\alpha},$$

conventionally defined to be the Peclet number. Although the fluid energy equation (2.11) now contains a parameter, the boundary condition analogous to (2.9) will be somewhat more general. Further advantages of our approach are discussed in the next Section where the solution of (2.6-2.10) is presented.

Our dimensionless lengths have a form similar to the dimensionless law-of-the-wall lengths used in wall-bounded turbulent flows (White 1974, p.473). Our dimensionless length x differs from the turbulent wall layer length x^+ by a factor of the square of the Prandtl number:

$$x = x^+ \sqrt{Pr} = x^* \frac{\sqrt{\tau_w/\rho}}{\nu} \sqrt{\frac{\nu}{\alpha}} .$$

Similarly,

$$y = y^+ \sqrt{Pr}$$

$$z = z^+ \sqrt{Pr} .$$

Here, Pr is the Prandtl number, x^+ is the length x* expressed in wall layer units, and τ_w is the wall shear stress.

2.2 General Temperature Field and Heat Flux Solutions

Solution of (2.6-2.10) yields a complete three-dimensional description of the temperature fields and heat flux distributions for a given probe heat source distribution. The temperature field T(x,y,z) is obtained by a

combination of analytical and numerical techniques. This approach is similar to that used by Tanner (1967) and Davies and Kimber (1972) to solve simplified forms of the governing equations. Solutions to the energy equations in both the fluid (2.6) and solid (2.7) domains are obtained by first analytically performing Fourier transformations in the streamwise and spanwise directions. These two-dimensional transformations reduce the partial differential equations (2.6) and (2.7) to ordinary differential equations whose solutions are then found. The arbitrary constants of these solutions are evaluated from transformed forms of boundary conditions (2.8) - (2.10). The two-dimensional inversion integral is then calculated numerically because of the complexity of the expressions involved.

Temperature Field

We define the two-dimensional Fourier transform of a function f(x,z) to be

$$\hat{f}(p,q) = \int_{-\infty}^{\infty}\int_{-\infty}^{\infty} e^{2\pi i(px + qz)} f(x,z)\, dx\, dz. \qquad (2.12)$$

The inverse transform is then

$$f(x,z) = \int_{-\infty}^{\infty}\int_{-\infty}^{\infty} e^{-2\pi i(px + qz)} \hat{f}(x,z)\, dx\, dz. \qquad (2.13)$$

Here, $i = \sqrt{-1}$, and p and q are modified wavenumbers such that

$$p = 1/\lambda_x$$

$$q = 1/\lambda_z$$

where λ_x and λ_z are the wavelengths of components in the x and z directions respectively.

Fourier transformation of (2.6)-(2.10) in the streamwise and spanwise directions leads to a set of coupled ordinary differential equations in wavenumber space:

$$\frac{d^2}{dy^2}\hat{T}_f - 4\pi^2 \left(p^2 + q^2 - i\frac{p}{2\pi} y\right) \hat{T}_f = 0 \qquad (2.14)$$

$$\frac{d^2}{dy^2}\hat{T}_s - 4\pi^2 (p^2 + q^2)\, \hat{T}_s = 0 \qquad (2.15)$$

$$\hat{T}_f = \hat{T}_s \quad , y = 0 \qquad (2.16)$$

$$K \frac{d}{dy}\hat{T}_s - \frac{d}{dy}\hat{T}_f = \hat{Q} \quad , y = 0 \qquad (2.17)$$

$$\hat{T}_f \to 0 \quad , \quad y \to +\infty \qquad (2.18a)$$

$$\hat{T}_s \to 0 \quad , \quad y \to -\infty. \qquad (2.18b)$$

By use of the new independent variable,

$$\eta \equiv (2\pi p)^{1/3} e^{-\pi i/6} \left(y + i\, 2\pi \frac{p^2 + q^2}{p}\right) \qquad (2.19)$$

differential equation (2.14) can be put in the form of Airy's

equation:

$$\frac{d^2}{d\eta^2}\hat{T}_f - \eta\,\hat{T}_f = 0. \tag{2.20}$$

The solutions of (2.20) and (2.15) subject to the boundary conditions at infinity (2.18) can be expressed in terms of two arbitrary constants C_f and C_s that are functions of p and q:

$$\hat{T}_f(y) = C_f(p,q) \cdot Ai(\eta) \quad , \quad y \geq 0 \tag{2.21}$$

$$\hat{T}_s(y) = C_s(p,q) \cdot e^{2\pi\sqrt{p^2+q^2}\,y} \quad , \quad y \leq 0. \tag{2.22}$$

By the use of the coupling conditions (2.15) and (2.16) at y=0, C_f and C_s are found to be:

$$C_f = \frac{\hat{Q}}{K \cdot 2\pi\sqrt{p^2+q^2}\,Ai(\eta_0) - \frac{(2\pi p)^{1/3}}{e^{\pi i/6}}\,Ai'(\eta_0)} \tag{2.23}$$

$$C_s = C_f \cdot Ai(\eta_0) \tag{2.24}$$

where

$$\eta_0 = \eta(y=0) = e^{\pi i/3}(2\pi)^{4/3}\frac{p^2+q^2}{p^{2/3}}. \tag{2.25}$$

Of particular interest is the temperature distribution at the wall (y=0). We define

$$\hat{T}_o \equiv \hat{T}_f (y = 0) = \hat{T}_s (y = 0) = C_s \tag{2.26}$$

Thus, the complete temperature field in wavenumber space can be expressed as:

$$\hat{T}_f (y) = \hat{T}_o \frac{Ai(n)}{Ai(n_o)} , \quad y \geq 0 \tag{2.27}$$

$$\hat{T}_s (y) = \hat{T}_o e^{2\pi\sqrt{p^2 + q^2}\, y} , \quad y \leq 0 \tag{2.28}$$

$$\hat{T}_o = \frac{\hat{Q}}{K\, 2\pi\sqrt{p^2 + q^2} - \frac{(2\pi p)^{1/3}}{e^{\pi i/6}} \frac{Ai'(n_o)}{Ai(n_o)}} . \tag{2.29}$$

In calculating the temperature field at some value of y, it is not necessary to first determine $\hat{T}_o$; expressions (2.27) and (2.28) are written in terms of $\hat{T}_o$ merely as a matter of convenience.

Expressions (2.27)-(2.29) represent a Green's function solution (in wavenumber space) for our model. We can therefore restate the solution as:

$$\hat{T} (y) = \hat{Q} \cdot \hat{G} (y) \tag{2.30}$$

where $\hat{G}$ is the two-dimensional transform of the Green's function for the temperature distributon and is defined to be:

$$\hat{G} (y) = \hat{G}_o \frac{Ai(n)}{Ai(n_o)} , \quad y \geq 0$$

$$= \hat{G}_o e^{2\pi \sqrt{p^2 + q^2}\, y} , \quad y \leq 0 \tag{2.31}$$

$$\hat{G}_o = \frac{1}{K \cdot 2\pi\sqrt{p^2 + q^2} - \frac{(2\pi p)^{1/3}}{e^{\pi i/6}} \frac{Ai'(n_o)}{Ai(n_o)}} . \tag{2.32}$$

Consistent with this Green's function interpretation of our solution, a particular temperature field is represented in wavenumber space as the product of a source distribution $\hat{Q}$ and the Green's function $\hat{G}(y)$. The Green's function component $\hat{G}$ depends only on the conductivity ratio K and is thus completely determined by the probe's environment and independent of the details of the probe geometry and heat source distribution. This rendering of $\hat{G}$ to be a function solely of K is made possible by the selection of $\sqrt{\alpha/s}$ as the characteristic length. The source component $\hat{Q}$ depends upon the probe geometry and heat distribution as well as the flow conditions, but is not influenced in any way by the substrate. In addition to providing a conceptually tractable form for the solution, this approach also enables one to focus on the specification of $\hat{Q}(p,q)$ - or, more appropriately, $Q(x,z)$. One can investigate the desirable properties of $\hat{Q}$ once $\hat{G}$ is known and can also calculate $\hat{G}$ once and save it to use with various source distributions.

The desired temperature field T(x,y,z) is found by application of inversion integral (2.13):

$$T(x,y,z) = \int_{-\infty}^{\infty}\int_{-\infty}^{\infty} e^{-2\pi i(px + qz)}\, \hat{T}(p,y,q)\,dpdq$$

$$= \int_{-\infty}^{\infty}\int_{-\infty}^{\infty} e^{-2\pi i(px + qz)}\, \hat{Q}(p,q) \cdot \hat{G}(p,y,q)\,dpdq \qquad (2.33)$$

This operation may also be viewed as the convolution of Q(x,z), the distribution of heat generation, with G(x,y,z), the temperature distribution produced by a point source of heat located at (x,y,z)=(0,0,0). The resulting convolution integral is identical to a superposition integral:

$$T(x,y,z) = \int_{-\infty}^{\infty}\int_{-\infty}^{\infty} Q(x',z') \cdot G(x - x', y, z - z')dx'dz' \qquad (2.34)$$

One may thus examine solution characteristics in eitner physical or wavenumber space - whichever is the more convenient.

Heat Flux

The heat flux crossing any plane parallel to the wall is easily obtained. The heat flux in the direction of increasing absolute value of y* - i.e., away from the wall - at any value of (x*,y*,z*) is given by

$$q_f^* = -k_f \frac{\partial}{\partial y^*} T_f^*, \qquad y^* \geq 0 \qquad (2.35a)$$

$$q_s^* = k_s \frac{\partial}{\partial y^*} T_s^*, \qquad y^* \leq 0 \qquad (2.35b)$$

Nondimensionalizing as before,

$$q_f = -\frac{\partial T_f}{\partial y}, \quad y \geq 0 \qquad (2.36a)$$

$$q_s = K \frac{\partial T_s}{\partial y} \quad , \quad y \leq 0 \tag{2.36b}$$

where

$$q_{f,s} = q^*_{f,s} \frac{\alpha}{s P^*_s} . \tag{2.37}$$

The two-dimensional Fourier transform of (2.37) is:

$$\hat{q}_f = - \frac{d}{dy} \hat{T}_f \tag{2.38a}$$

$$\hat{q}_s = K \frac{d}{dy} \hat{T}_s . \tag{2.38b}$$

The differentiation in (2.38) can be carried out after substituting for $\hat{T}_f$ and $\hat{T}_s$ from (2.30)-(2.32). The resulting expressions are:

$$\hat{q}_f = -\hat{Q} \frac{(2\pi p)^{1/3}}{e^{\pi i/6}} \frac{Ai'(\eta)}{Ai(\eta_0)} \hat{G}_0$$

$$= \frac{-(2\pi p)^{1/3}}{e^{\pi i/6}} \frac{Ai'(\eta)}{Ai(\eta)} \hat{T}_f \tag{2.39a}$$

$$\hat{q}_s = \hat{Q} \cdot K \cdot 2\pi \sqrt{p^2 + q^2}\, e^{2\pi \sqrt{p^2 + q^2}\, y} \cdot \hat{G}_0$$

$$= K \cdot 2\pi \sqrt{p^2 + q^2}\, \hat{T}_s . \tag{2.39b}$$

The fluxes $q_f(x,y,z)$ and $q_s(x,y,z)$ are then obtained by application of inversion integral (2.13).

The heat flux expression of most interest is that at y=0. This represents the heat exchange between the substrate and

the fluid. Expressions (2.39a,b) become:

$$\hat{q}_f(y=0) = \frac{-\hat{Q}}{K\sqrt{\eta_0}\,\dfrac{Ai(\eta_0)}{Ai'(\eta_0)} - 1} \tag{2.40a}$$

$$\hat{q}_s(y=0) = \hat{Q} \cdot \frac{K\sqrt{\eta_0}\,\dfrac{Ai(\eta_0)}{Ai'(\eta_0)}}{K\sqrt{\eta_0}\,\dfrac{Ai(\eta_0)}{Ai'(\eta_0)} - 1} . \tag{2.40b}$$

Condition (2.17) may be rewritten as

$$\hat{q}_s(y=0) + \hat{q}_f(y=0) = \hat{Q}. \tag{2.41}$$

It is interesting to examine the values of (2.40a) and (2.40b) at (p,q) = (0,0). These represent the integrals over all (x,z) at y=0 of q_f and q_s, respectively, i.e., the integrals over the entire fluid - substrate interface. These values are $\hat{Q}(0,0)$ and 0, respectively. Thus, the net flux into the substrate is zero; all the heat transferred from the probe ultimately ends up in the fluid. Much of this heat, however, flows first to the substrate, and then to the fluid. The exchange of heat between the fluid and the substrate is further discussed later.

2.3 Numerical Evaluation

The complexity of integrands (2.30)-(2.32) and (2.39)

necessitates a numerical evaluation of the inversion integral. The inversion is performed by applying a set of numerical one-dimensional Fast Fourier Transforms (FFT's), first in one variable and then in the other. The integrand is first numerically evaluated at a finite set of discrete values of (p,q). The Airy function and its derivative are evaluated from series expansions. Taylor series are used for small values of the argument, and asymptotic series are used for larger values. Tests were performed to determine the number of terms to use in the expansions to achieve an accuracy of better than 0.2% (compared to tabulated values (Abramowitz and Stegun, 1972) and to determine the appropriate argument value at which to change from evaluation by Taylor series to evaluation by asymptotic series. Details of these expansions are presented in Appendix A.

The transform of the source distribution, $\hat{Q}(p,q)$, can be found analytically for relatively simple source distributions (e.g., uniform heat generation over a rectangular probe), or can be obtained numerically for more complicated distributions. If $\hat{Q}$ is obtained analytically, it must also be numerically evaluated at the appropriate values of (p,q) prior to inversion. All operations are performed using complex arithmetic.

Aside from this negligible error introduced by the numerical evaluation of the integrand, numerical inversion leads to two potential sources of error inherent in any

numerical evaluation of an infinite integral: that due to discretization and that due to truncation. The discretization process, occurring in (p,q) space, determines the smallest resolvable "wavenumber". This is equivalent to specifying the largest wavelength component of the computed temperature distribution. Effectively, one is unable to distinguish between the computed temperature distribution and the distribution due to an infinite array of identical probes whose spacing is this "longest wavelength". Truncation of the inversion integral places a limit on the maximum "wavenumber" that can be represented. This fixes the smallest wavelength component of the computed temperature distribution, and determines the minimum resolution of this temperature field. Thus, the spacing of the points at which the temperature is computed is specified by the truncation of the inversion integral, while the spatial extent of the temperature field is determined by the discretization.

As with simpler numerical integrations, errors from these sources can be reduced to negligible levels through judicious truncation and discretization. In practice, we have found that the discretization size was of much greater importance than the truncation limits. The appropriate values of p and q at which to truncate the integration are determined by requiring the resultant temperature distributions to be smooth enough that there is no discernible ripple. Selection of the proper discretization (δp, δq) is further complicated by the

sigularity of integrands (2.27)-(2.29) at (p,q)=(0,0). An appropriate average integrated value of the integrand at (p,q)=(0,0) is used to deal with this singularity. An inequality constraint between the chosen values of δp and δq arises from the approximations made in dealing with this singularity. This constraint, its derivation, and the method of treating the singularity are presented and discussed in Appendix B.

Through numerical experimentation, we have developed a criterion to determine the discretization error. A physically realistic temperature field decays asymptotically to zero with increasing distance from the probe. The computed temperature fields are found to decay to some small fraction of the maximum temperature that, in general, is very close to zero, but which can be either positive or negative. We have also found that the slowest decay occurs along the x axis - i.e., in the streamwise direction. The probe Nusselt numbers based on average probe temperature (as defined in the next Section) were computed for a series of cases in which the values of δp and δq were decreased. The Nusselt number exhibits an asymptotic behavior when it is plotted against various quantities indicative of temperature field decay. The criterion we employ involves two such quantities: the ratio of the absolute value of the minimum temperature of the entire field to the maximum temperature and the ratio of the absolute value of the minimum temperature along the x axis to the

maximum temperature. For the tests run, we found the Nusselt number to be within 1% of its asymptotic value when both these ratios were 0.01 or less. These tests are presented in figure 2.2 where the ratio of the computed probe Nuselt number to its asymptotic value is plotted against the larger of these two temperature ratios. We adopted the criterion that both these temperature ratios must be less than or equal to 0.01.

The average probe temperature is found by performing a two-dimensional integration of the computed probe temperature field using a Simpson's rule quadrature. The total number of points contributing to the average typically varied between 25 and 91. A few cases were outside of this range. The probe Nusselt number is then calculated using this value of the average temperature. Some approximation error is introduced into the calculation of the average temperature from the computed temperature field by this integration procedure.

2.4 Heat Source Distribution Specification

Rectangular Uniform Source

Calculations for a specific probe design require the specification of the source (probe) heat generation distribution $Q(x,z)$, or more precisely the transform of that distribution, $\hat{Q}(p,q)$. The source distribution introduces additional length scales. In the case of a rectangular probe,

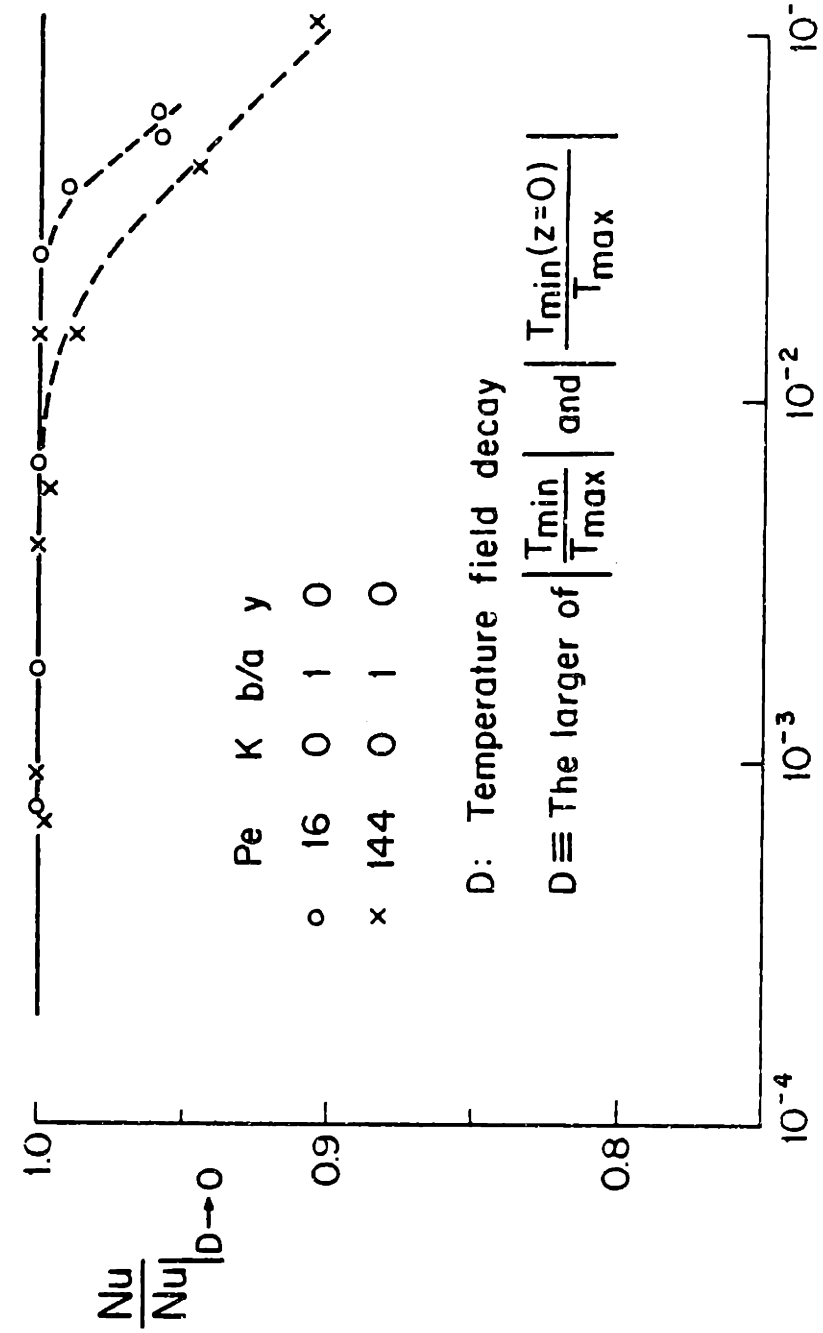

Figure 2.2 Tests of criterion for estimating numerical error.

those are the streamwise and spanwise probe lengths which we denote by 2a* and 2b* respectively or, in dimensionless form, as 2a and 2b. Additional parameters dealing with the details of the heat source distribution over the probe may also be needed. A simple case which should be a good approximation to true probe operating conditions is that of uniform heat generation throughout the probe:

$$Q^*(x^*, z^*) = \frac{P_s^*}{4a^* b^*} \cdot H\left(1 - \left|\frac{x^*}{a^*}\right|\right) \cdot H\left(1 - \left|\frac{z^*}{b^*}\right|\right) \qquad (2.42)$$

or in dimensionless form

$$Q(x, z) = \frac{1}{4ab} \cdot H\left(1 - \left|\frac{x}{a}\right|\right) \cdot H\left(1 - \left|\frac{z}{b}\right|\right) \qquad (2.43)$$

where H is the Heaviside function defined as:

$$H(\xi) = 0, \ \xi < 0$$

$$H(\xi) = 1, \ \xi \geq 0.$$

Specification of a uniform heat generation rate does not require the distribution of heat flux to either the fluid or the substrate to be uniform. Rather, since no provision is made for conduction within the probe, the total amount of heat transferred away from the probe is the same at all (x,z) locations on the probe and is equal to the sum of two components: the heat transferred directly to the fluid and the heat transferred directly to the substrate. The relative sizes of these two components of the heat transfer can and do exhibit spatial variation over the probe.

The two-dimensional Fourier transform of distribution (2.43) is:

$$\hat{Q}(p, q) = \frac{\sin (2\pi ap)}{2\pi ap} \cdot \frac{\sin (2\pi bq)}{2\pi bq} . \qquad (2.44)$$

The form of expression (2.44) introduces some additional numerical considerations which are descussed in Appendix B.

The transform space Green's function expressions (2.31) and (2.32) contain only the parameter K. The rectangular uniform heat generation rate probe expression (2.44) introduces the additional parameters a and b. It is both conventional and convenient to use instead the related parameters probe aspect ratio (b/a) and Peclet number. The Peclet number Pe is a measure of the relative effects of convection and conduction and is conventionally defined to be:

$$Pe \equiv \frac{s L_p^{*2}}{\alpha} . \qquad (2.45)$$

Realizing that the streamwise probe length $L_p^* = 2a^*$, and using the characteristic length $\sqrt{\alpha/s}$ as before, we can write:

$$Pe = 4a^{*2} s/\alpha = 4a^2$$

$$2a = \sqrt{Pe} .$$

Thus the dimensionless streamwise probe length 2a is equal to the square root of the Peclet number, and the parameters a and b are simply related to the two design parameters, Peclet

number and probe aspect ratio.

Probe Nusselt Number

We define a Nusselt number based on the fluid thermal conductivity, the total heat transferred from the probe (the sum of the heat transferred directly to the fluid and that transferred directly to the substrate), the spatially averaged probe temperature $\bar{T}_p^*$, the streamwise length of the probe, and the probe area as follows:

$$Nu = \frac{P_s^* \, 2a^*}{\bar{T}_p^* \, 2a^* \, 2b^* \, k_f} \tag{2.46}$$

or, in terms of the dimensionless variables previously defined,

$$Nu = \frac{1}{\bar{T}_p \cdot 2b}. \tag{2.47}$$

This definition of Nusselt number is consistent with that of other researchers and can be easily formed from experimentally-measurable quantities.

Two-dimensional Geometry

A two-dimensional probe geometry can be represented by

$$\hat{Q}(p, q) = \frac{\sin(2\pi a p)}{2\pi a p} \cdot \delta(q). \tag{2.48}$$

This expression is derived by taking the limit of (2.44) as b approaches infinity. The discrete representation of the delta function in (2.48) is equivalent to a discretization of (2.44) such that $\delta q = 1/2b$. Thus (2.48) is evaluated at the zeroes of its sine function. As discussed earlier, this has the effect of specifying the longest spanwise wavelength of any component of the temperature distribution to be 2b. We use this formulation in our two-dimensional computations. As expected, the computed temperatures show no spanwise variation.

It is of course possible, and computationally more efficient, to analyze two-dimensional cases by noting that the integrand need only be evaluated at one value of q - i.e., q=0 - and that the inverse transform of a delta function is unity. Thus, only the inversion integral in p needs to be evaluated. These two formulations are equivalent. The former formulation, however, provides an easy method of evaluating two-dimensional probes from the full three-dimensional model by appropriate selection of δq.

Other Source Distributions

A nonrectangular probe or a nonuniform heat generation rate will change the form of $Q(x,z)$ and of $\hat{Q}(p,q)$. For cases in which the transform of Q is not readily obtainable in analytic form, it may be found numerically. In principle, any probe heat generation distribution can be handled. Of

particular interest are the distributions due to a point source of heat on a conducting wall and that due to a finite line source. The former represents a fundamental solution that is not previously known. Here, $Q = \delta(x)\,\delta(z)$ and $\hat{Q}=1$. The latter represents a model for dealing with an increasingly popular variant on the hot-film for the measurement of shear stress - the buried wire (Section 5.3). In this case,

$$Q = \delta(x) \cdot H\left(1 - \left|\frac{z}{b}\right|\right).$$

The capability of handling such diverse probe types is one of the strengths of our technique.

2.5 Zero Flow Solution

Solution of expressions (2.27) - (2.29) for the limiting case of zero flow - i.e., pure conduction in a stagnant fluid in contact with a conducting substrate - is not possible due to the nondimensionalization by the characteristic length ($\sqrt{\alpha/s}$). As the shear goes to zero, this length becomes infinite. Thus, a separate method of analysis is called for. It is possible, however, to perform calculations for very small values of Pe. We have experienced no problems in obtaining results for values of Pe as low as 0.06. Such low Pe results should asymptotically approach those for Pe=0 calculated here. This provides an independent check on the validity of our calculations at low shear rates. This

matching is excellent and is presented in Section 4.2.

To obtain a solution for zero flow, we use the probe half length a* as the characteristic length for nondimensionalization of the governing equations. Of (2.6) - (2.1), only the fluid domain equation (2.6) changes for the case of zero flow. The complete set of governing equations and boundary conditions with a* as the length scale is thus:

$$\nabla^2 T_f = 0, \quad y \geq 0 \tag{2.49}$$

$$\nabla^2 T_s = 0, \quad y \leq 0 \tag{2.7}$$

$$T_f = T_s, \quad y = 0 \tag{2.8}$$

$$K \cdot \frac{\partial}{\partial y} T_s - \frac{\partial}{\partial y} T_f = Q(x, z), \quad y = 0 \tag{2.9}$$

$$T_{f,s} \to 0 \quad \text{as} \quad x, y, z \to \pm \infty. \tag{2.10}$$

The solution of this set of equations for an arbitrary heat flux distribution can be obtained by superposition of the solution for a point source of heat along the boundary of a half space. The temperature field due to conduction of heat into a half space from an arbitrary heat source distribution $Q^*(x^*, y^*=0, z^*)$ is given by:

$$T^*(x^*, y^*, z^*) = \frac{1}{2\pi} \int_{-\infty}^{\infty} \int_{-\infty}^{\infty} \frac{Q^*(x^{*\prime}, z^{*\prime})\, dx^{*\prime}\, dz^{*\prime}}{\left[(x^* - x^{*\prime})^2 + y^{*2} + (z^* - z^{*\prime})^2\right]^{1/2}}. \tag{2.50}$$

In dimensionless form, then, the temperature distribution can be expressed as:

$$T_f(x, y, z) = \frac{1}{2\pi} \int_{-\infty}^{\infty} \int_{-\infty}^{\infty} \frac{q_f(x', z')\ dx'\ dz'}{\left[(x - x')^2 + y^2 + (z - z')^2\right]^{1/2}} \qquad (2.51)$$

$$T_s(x, y, z) = \frac{1}{2\pi K} \int_{-\infty}^{\infty} \int_{-\infty}^{\infty} \frac{q_s(x', z')\ dx'\ dz'}{\left[(x - x')^2 + y^2 + (z - z')^2\right]^{1/2}} \qquad (2.52)$$

where

$$q_f(x, z) = - \frac{\partial T_f}{\partial y} (x, y=0, z) \qquad (2.53)$$

$$q_s(x, z) = K \frac{\partial T_s}{\partial y} (x, y=0, z). \qquad (2.54)$$

Combining (2.8), (2.51), and (2.52), we have

$$\int_{-\infty}^{\infty} \int_{-\infty}^{\infty} \left\{ \frac{1}{K} q_s(x', z') - q_f(x', z') \right\} \frac{dx'\ dz'}{\left[(x - x')^2 + (z - z')^2\right]^{1/2}} = 0. \qquad (2.55)$$

Thus,

$$q_s(x, z) = K\, q_f(x, z) \qquad (2.56)$$

or,

$$\frac{\partial T_s}{\partial y} (x, y=0, z) = \frac{\partial T_f}{\partial y} (x, y=0, z). \qquad (2.57)$$

The dimensionless temperature gradients at the wall are equal and opposite. Since $T_f = T_s$ at $y=0$, equations (2.49) and (2.7) and their associated boundary conditions are identical except

for the sign of y. Thus, $T_f(x,y,z)=T_s(x,-y,z)$; the temperature distribution is symmetric about the interface y=0. The interface is an adiabatic boundary except at the probe.

The expressions for the flux into the fluid and into the solid in terms of the source distribution are found to be:

$$q_f(x, z) = \frac{1}{K + 1} Q(x, z) \tag{2.58}$$

$$q_s(x, z) = \frac{K}{K + 1} Q(x, z). \tag{2.59}$$

The temperature distribution in both the fluid and the solid is then expressible as:

$$T(x, y, z) = \frac{1}{2\pi(K + 1)} \int_{-\infty}^{\infty} \int_{-\infty}^{\infty} \frac{Q(x', z')\, dx'\, dz'}{\left[(x - x')^2 + y^2 + (z - z')\right]^{1/2}}. \tag{2.60}$$

This is the general expression for the temperature at any location for conduction in two adjacent media with a source of arbitrary geometry and distribution between them. In practice, the probe is of finite extent, and the infinite integral in (2.60) reduces to an integral over the area of the probe. From (2.60) it is easily seen that the temperature field for any conductivity ratio K is simply expressible in terms of that of the adiabatic wall (K=0) case:

$$T(K) = \frac{T(K = 0)}{K + 1}. \tag{2.61}$$

The Nusselt number, as before, is found to be:

$$Nu = \frac{1}{\bar{T}_p \cdot 2b} \tag{2.47}$$

where $\bar{T}_p$ is the average probe temperature found by integration of (2.60) over the probe surface and b is the dimensionless spanwise probe half length equal to b*/a* and thus equivalent to aspect ratio. This solution is not valid for a two-dimensional probe (b equal to infinity) since there is no steady state solution to pure conduction from a line source of heat.

The average temperature of a rectangular probe of uniform heat flux distribution as given by Carslaw and Jaeger (1959, p.265) can be expresed in terms of our dimensionless quantities as:

$$\bar{T}_p = \frac{1}{2\pi b^2}\left\{ b^2 \sinh^{-1}\frac{1}{b} + b \cdot \sinh^{-1} b + \frac{1}{3}\left(1 + b^3 - (1+b^2)^{3/2}\right)\right\} \tag{2.62}$$

Thus the Nusselt number for zero flow over a rectangular probe possessing a uniform heat source distribution can be obtained using equations (2.47), (2.61), and (2.62). Other geometries and source distributions may require performing the integration in (2.60) as well as further integration of the resulting probe temperature distribution to obtain the average probe temperature.

3. Model Predictions

We report here predictions for rectangular uniform source distribution probes in the range:

$$0.0625 \leq Pe \leq 400$$

$$0 \leq K \leq 50$$

$$0.5 \leq b/a \leq \infty$$

These values cover the vast majority of operating conditions for hot-film applications (Chapter 4). Predictions have been obtained with no change in the physical model or the governing equations nor with any extreme value approximations.

The majority of the predictions reported here are wall temperature field calculations - from which quantities such as Nusselt number are obtained. Temperature fields at various distances from the wall were also calculated. Such detailed predictions are useful in determining the regions of the probe's environment which affect its performance and the sensitivity of these regions to operating conditions and design parameters. Calculated heat flux distributions are also presented.

Temperature fields at various values of y and wall heat flux distributions are presented in this Chapter primarily to indicate the capabilities of our technique. A detailed parametric study of probe Nusselt number is also reported.

3.1 Temperature Fields

Temperature distributions taken from one predicted temperature field are presented in figure 3.1. Predicted temperatures normalized by the average probe temperature for a square probe mounted on an adiabatic wall at a Peclet number of 36 are shown plotted against distance from the probe center in both the streamwise and spanwise directions. The peak temperature is seen to occur downstream of the probe midpoint. Our calculations predict that the streamwise location of this maximum depends upon Peclet number and conductivity ratio. The temperature distributions decay monotonically in all directions from this maximum value. The spanwise temperature is symmetric about the probe center, while the streamwise profile is skewed such that the downstream decay is much slower than the upstream decay. The details of this streamwise distribution also vary with Pe and K.

The effect of K and Pe on the streamwise wall temperature distributions is indicated in figures 3.2 and 3.3. Figure 3.2 presents these temperature distributions for a fixed value of K and three values of Pe. Figure 3.3 similarly presents the distributions for a fixed value of Pe and four values of K. The distributions have been normalized by the average probe temperature of each case. The effects of Pe and K are, in a sense, opposing in that as Pe increases the temperature distribution is skewed to the downstream side of the probe

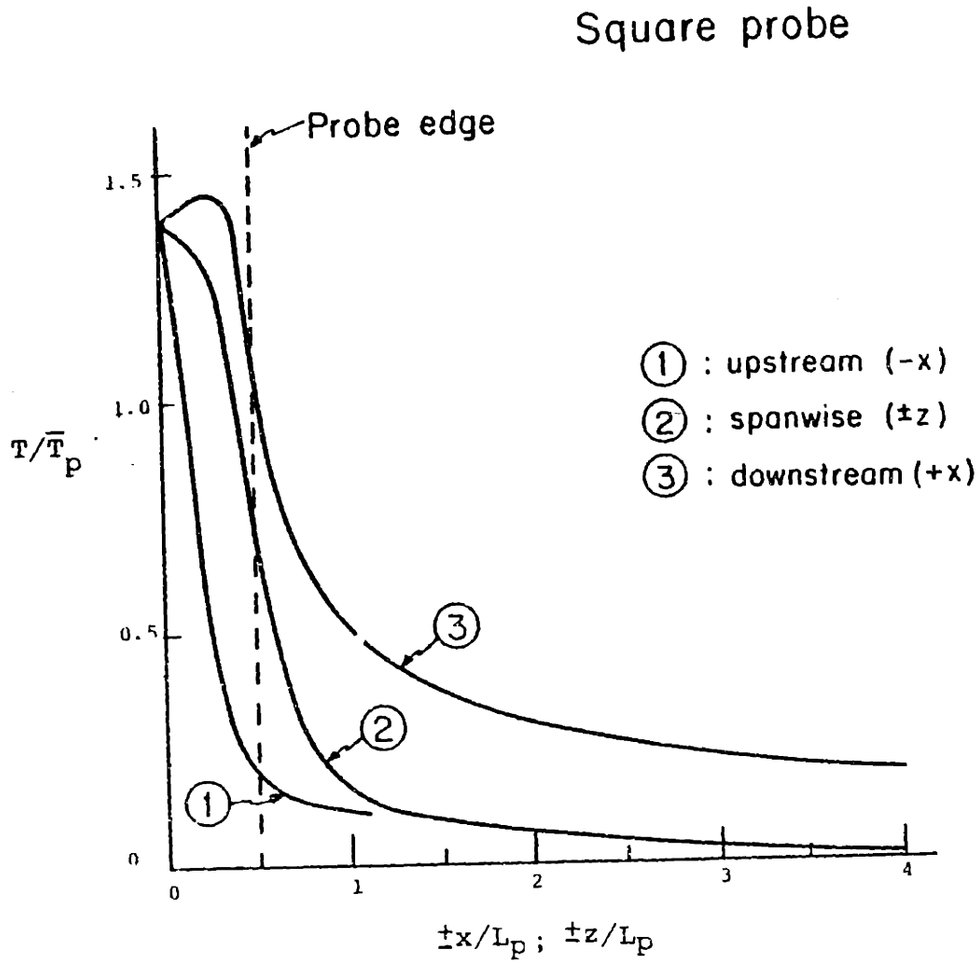

Figure 3.1 Comparison of streamwise and spanwise predicted temperature distributions (Pe=36; K=0; b/a=1).

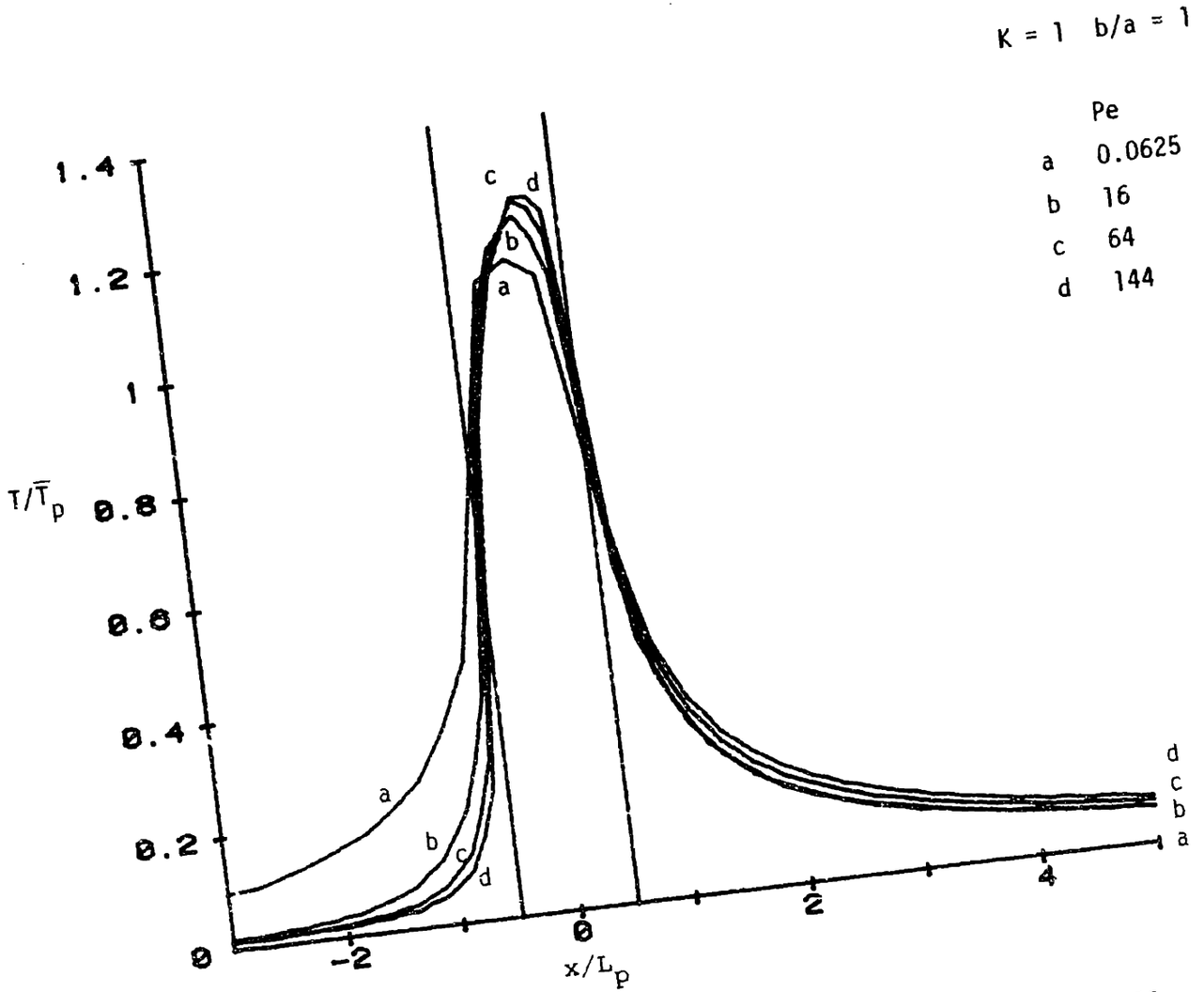

Figure 3.2 Predicted wall (y=0) streamwise temperature distribution variation with Peclet number (K=1; b/a=1; z=0).

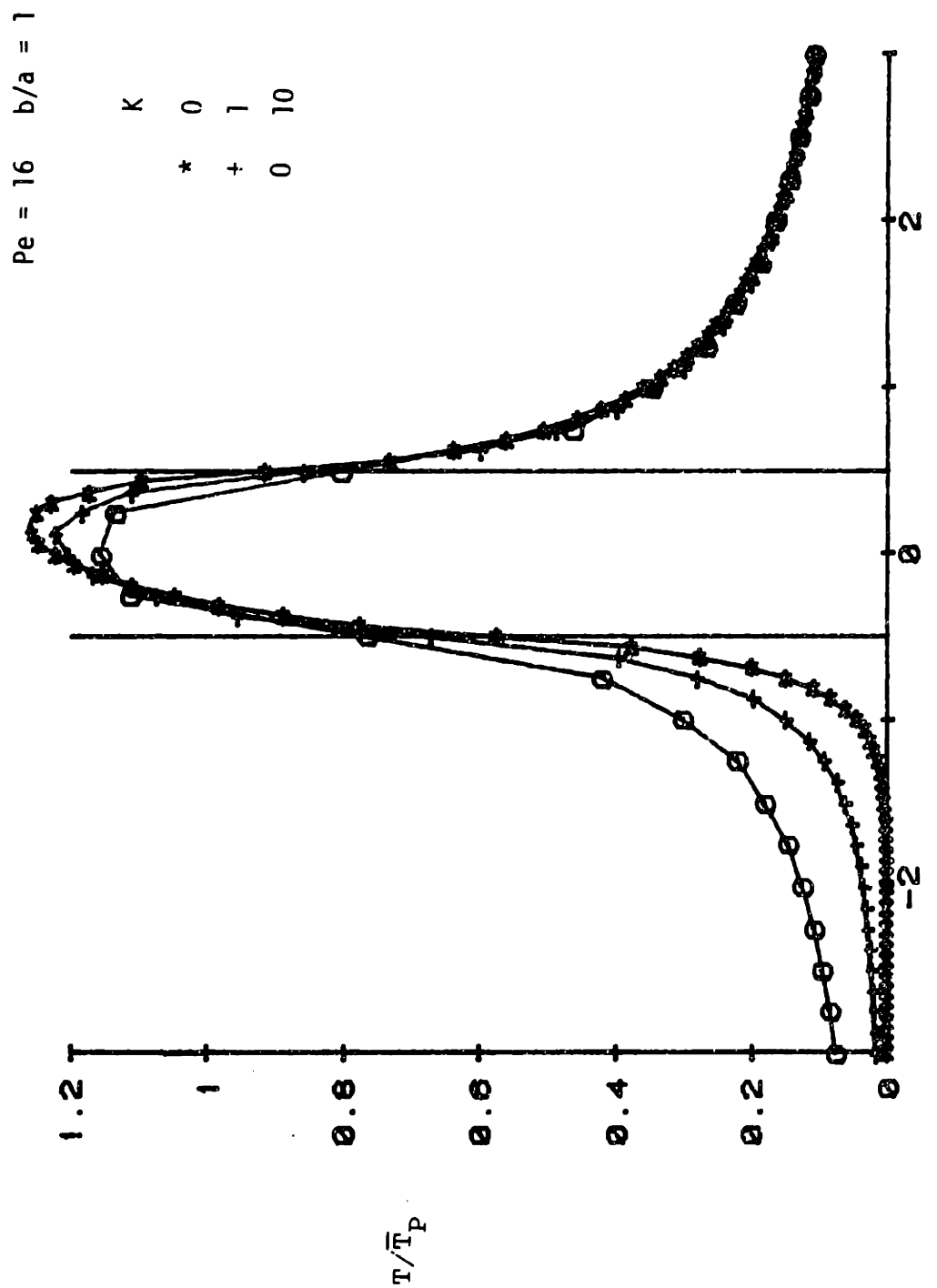

Figure 3.3 Predicted wall (y=0) streamwise temperature distribution variation with conductivity ratio (Pe=16; b/a=1; z=0).

while increased values of K make the distribution more symmetric about x=0. Large values of K and small values of Pe will also lead to a much more uniform distribution of probe temperature - i.e., there will be less spread between the maximum and minimum probe temperatures.

A more graphic portrayal of the temperature field behavior is obtained by examining the contour plots of figure 3.4 where surface isotherms along the y = 0 surface in the vicinity of the probe are plotted normalized by average probe temperature. The values of the parameters of Pe, K, and b/a associated with the temperature distributions of figure 3.4 were chosen to illustrate a variety of representative surface temperature behavior. An exhaustive presentation of such distributions from a detailed parametric study would clearly be prohibitive.

The temperature field in the fluid over any plane parallel to the wall is also easily obtained. As an example of such a calculation, a set of streamwise slices through calculated temperature distributions for y/2a = 0, 0.25, and 0.5 are presented in figure 3.5 for values of Pe=64, K=1, and b/a=1. Figure 3.6 presents a contour plot of isotherms for the calculated temperature field at y/2a = 0.5 from which the streamwise distribution in figure 3.5 is taken. The isotherms of figure 3.6 should be compared to those of figure 3.4 (y=0). As y increases, figures 3.5 and 3.6 exhibit the expected flattening of the temperature field, movement downsteam of the

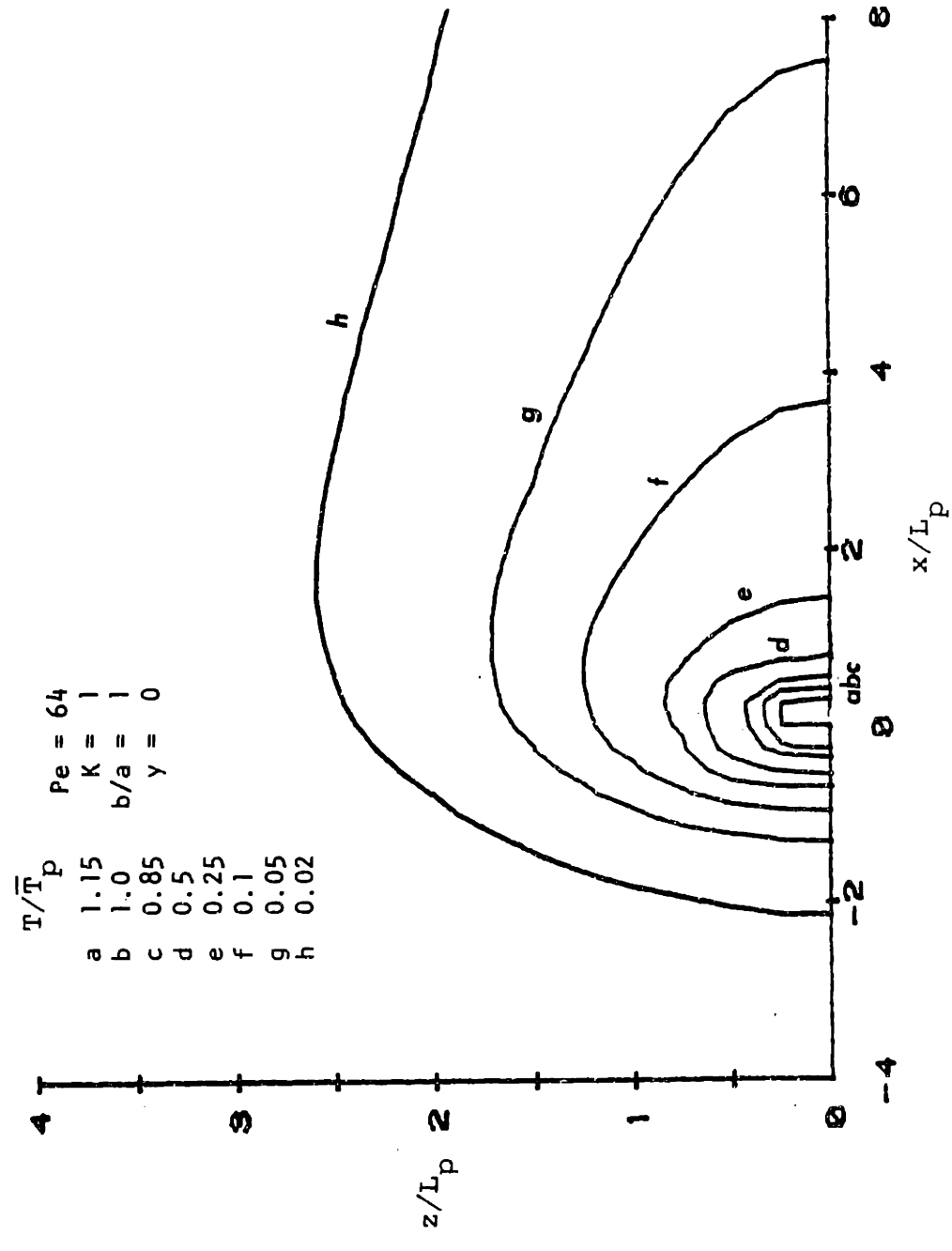

Figure 3.4 Predicted wall (y=0) isotherms normalized by the average probe temperature:
a) Pe=64; K=1; b/a=1.

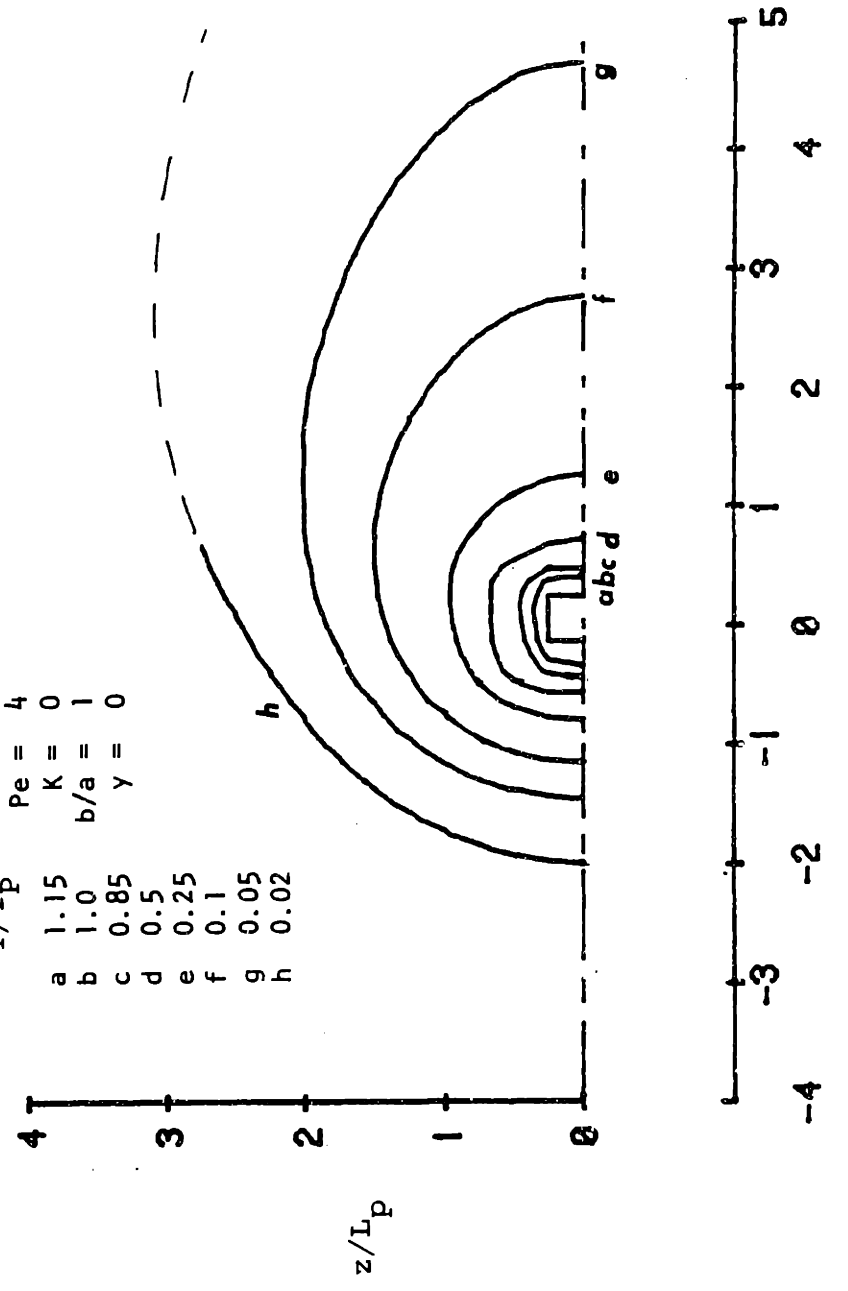

Figure 3.4 (continued)
b) Pe=4; K=0; b/a=1.

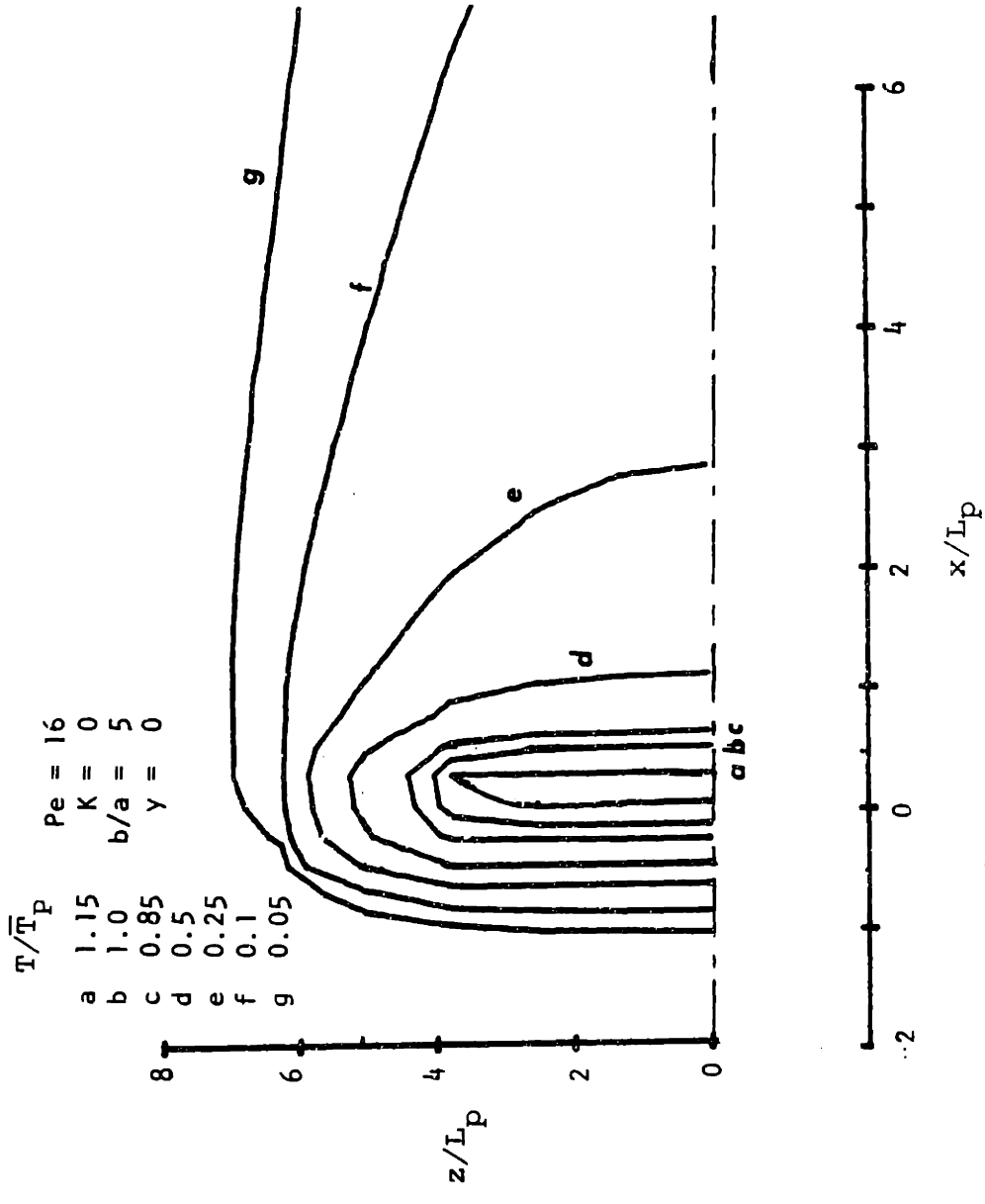

Figure 3.4 (continued)
c) Pe=16; K=0; b/a=5.

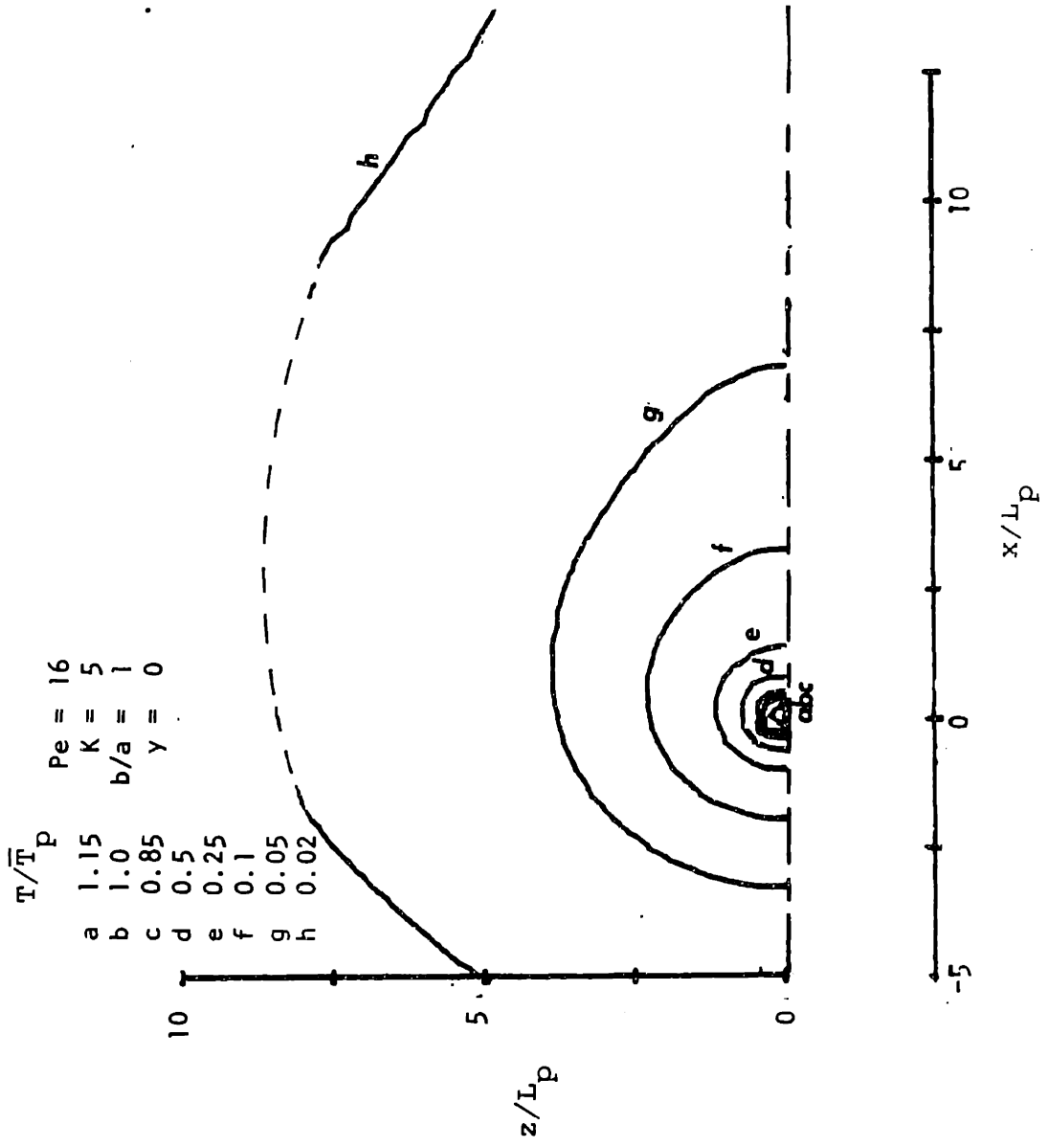

Figure 3.4 (continued)
d) Pe=16; K=5; b/a=1.

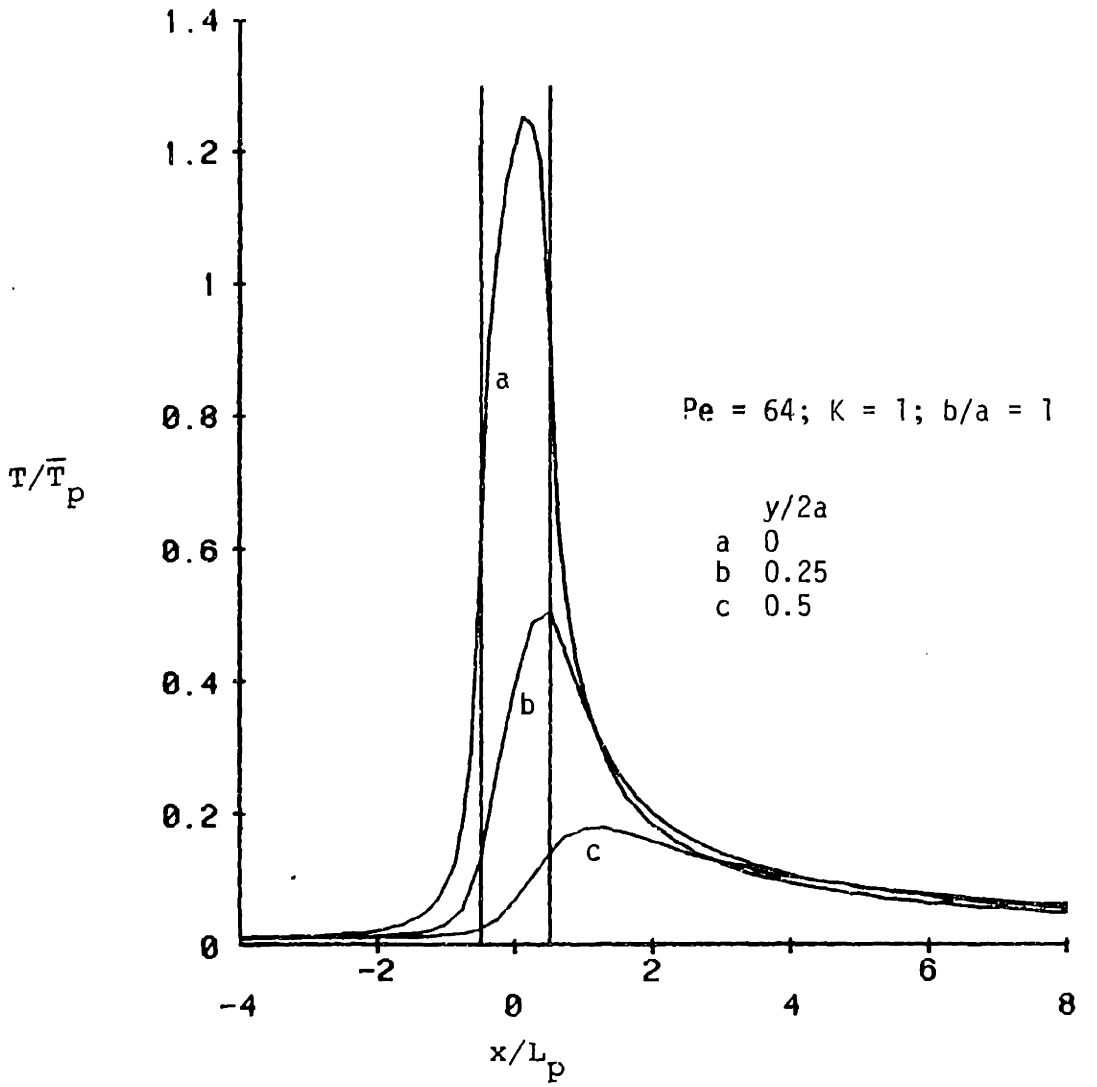

Figure 3.5 Predicted streamwise temperature distribution variation with y (Pe=64,; K=1; b/a=1; z=0).

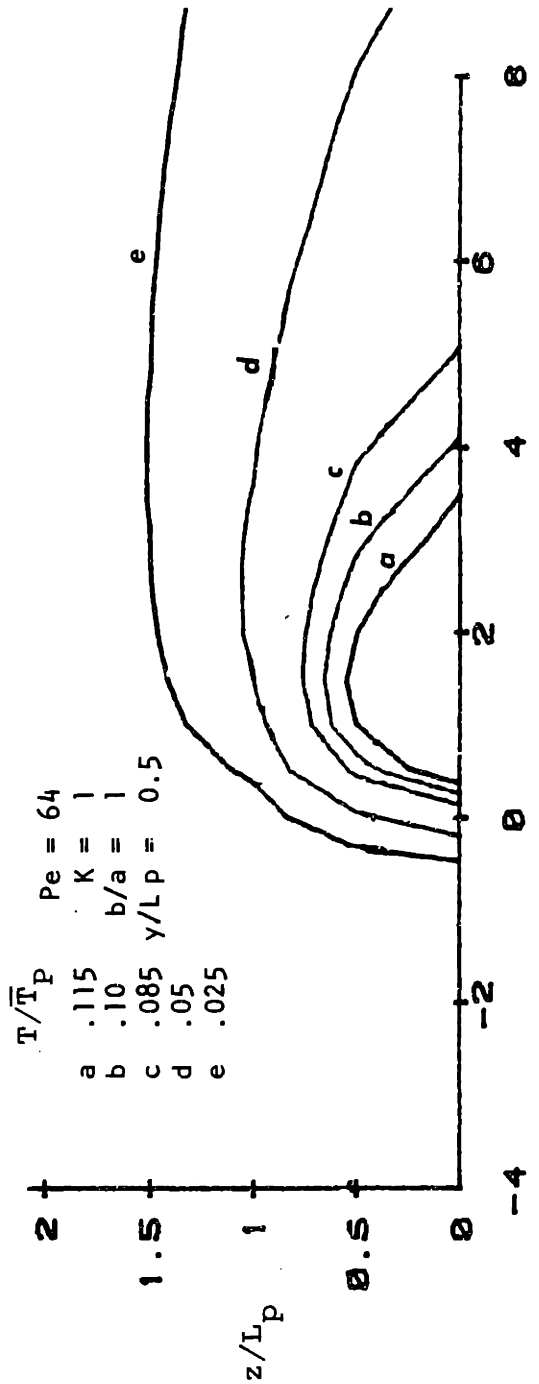

Figure 3.6 Predicted fluid isotherms along the plane $y/L_{p=0.5}$ (Pe=64; K=1; b/a=1).

peak temperature, and the decay with y of the distribution as a whole. Detailed investigations of the behavior of the temperature fields for $y > 0$ as a function of the governing parameters were not performed. Such an investigation could determine the extent of penetration of the thermal boundary layer into the fluid as a function of (x,z) and thus the region of the fluid velocity field that affects probe performance. This should be of greater importance for situations of high K in which the region of thermal penetration along the wall extends for large distances from the probe. Temperature fields within the substrate can be obtained using (2.28), but were not investigated in the present work.

3.2 Heat Flux Distributions

The partition between the fluid and the substrate of the heat generated in the probe and the flow of that heat between the two media is obtained from (2.40). Such information is of use in determining the details of substrate participation in probe performance and in proper probe substrate design. The heat flux crossing any plane parallel to the fluid-substrate surface can be obtained from (2.39). The procedure is very similar to that used for the temperature field calculations. We have found that calculation of the heat flux at a set of points different than that of the temperature field is better

numerically. This topic is discussed in Appendix B. Typically, the discretization chosen led to an evaluation of the flux at a "grid" of points spaced uniformly over the region of computation such that the number of points over the probe was 15 x 15 -i.e., 225.

Calculated heat flux distributions at the fluid-substrate surface (y=0) are presented in figure 3.7. Shown are lines of constant heat flux normal to the y=0 plane that have been normalized by the uniform source density Q. The sign convention chosen is that flux into the substrate is positive. These predictions show that the heat flow is from the substrate to the fluid over the majority of the region surrounding the probe. However, there exists a region downstream of the probe in which heat flows from the fluid to the substrate. This region extends for a significant distance downstream of the probe and has a spanwise extent comparable to that of the probe. The magnitude of the heat exchange between the fluid and substrate in the spanwise region in the vicinity of the ends of the probe is comparable to that in the upstream and downstream regions along z=0.

Figure 3.8 presents streamwise slices along z=0 of the heat flux into the substrate normal to the y=0 plane expressed as a fraction of the source density Q. The bounds of the probe are marked by the vertical bars at x/2a = -0.5, 0.5. The relation between the flux into the fluid, q_f, and the flux into the substrate, q_s, at y=0 can be obtained by combining

Figure 3.7 Contours of the predicted distribution of heat flux to the substrate (y=0):
a) Pe=16; K=1; b/a=1.

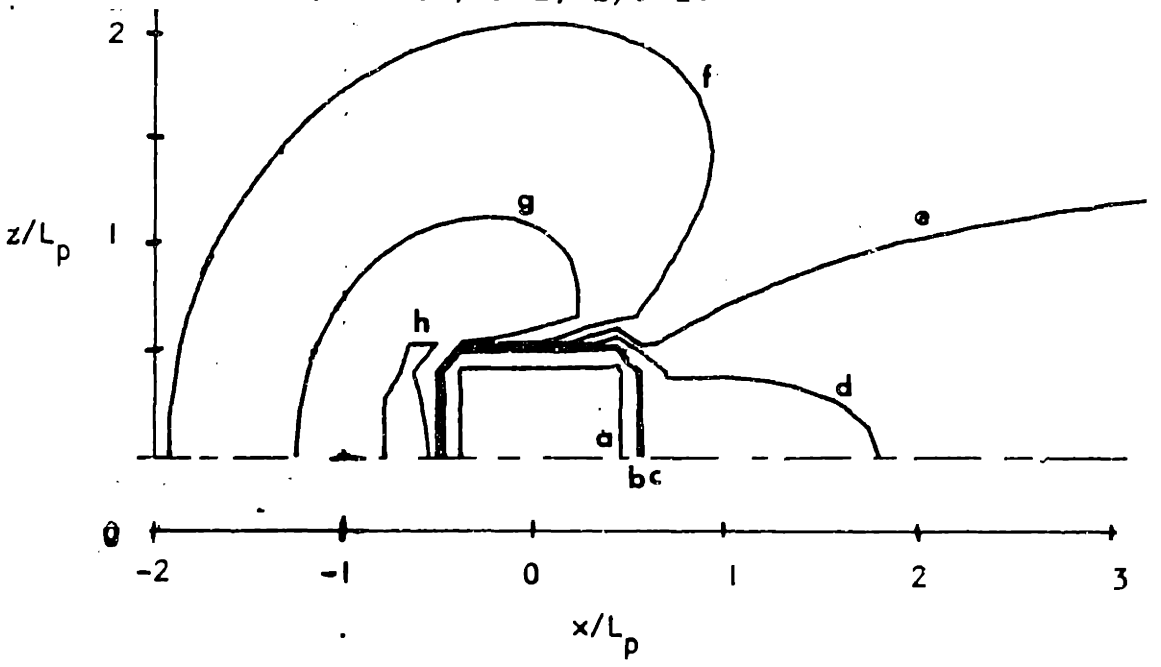

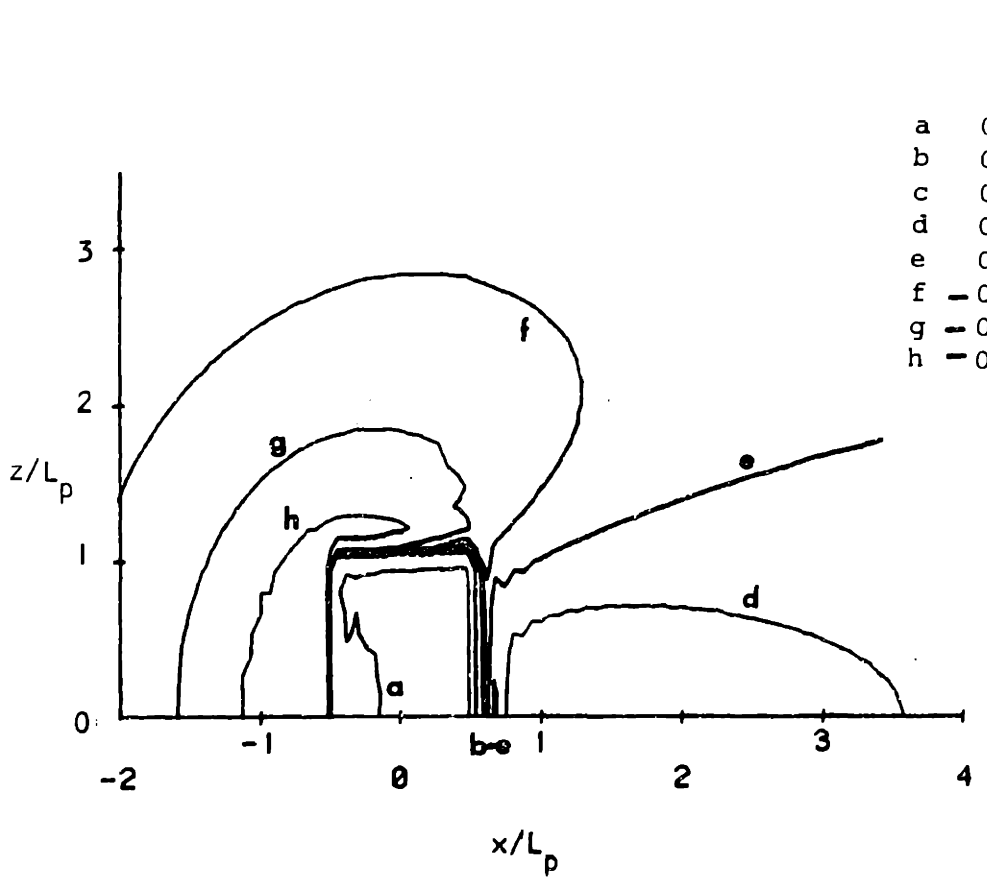

Figure 3.7 (continued)
b) Pe=16; K=1; b/a=2.

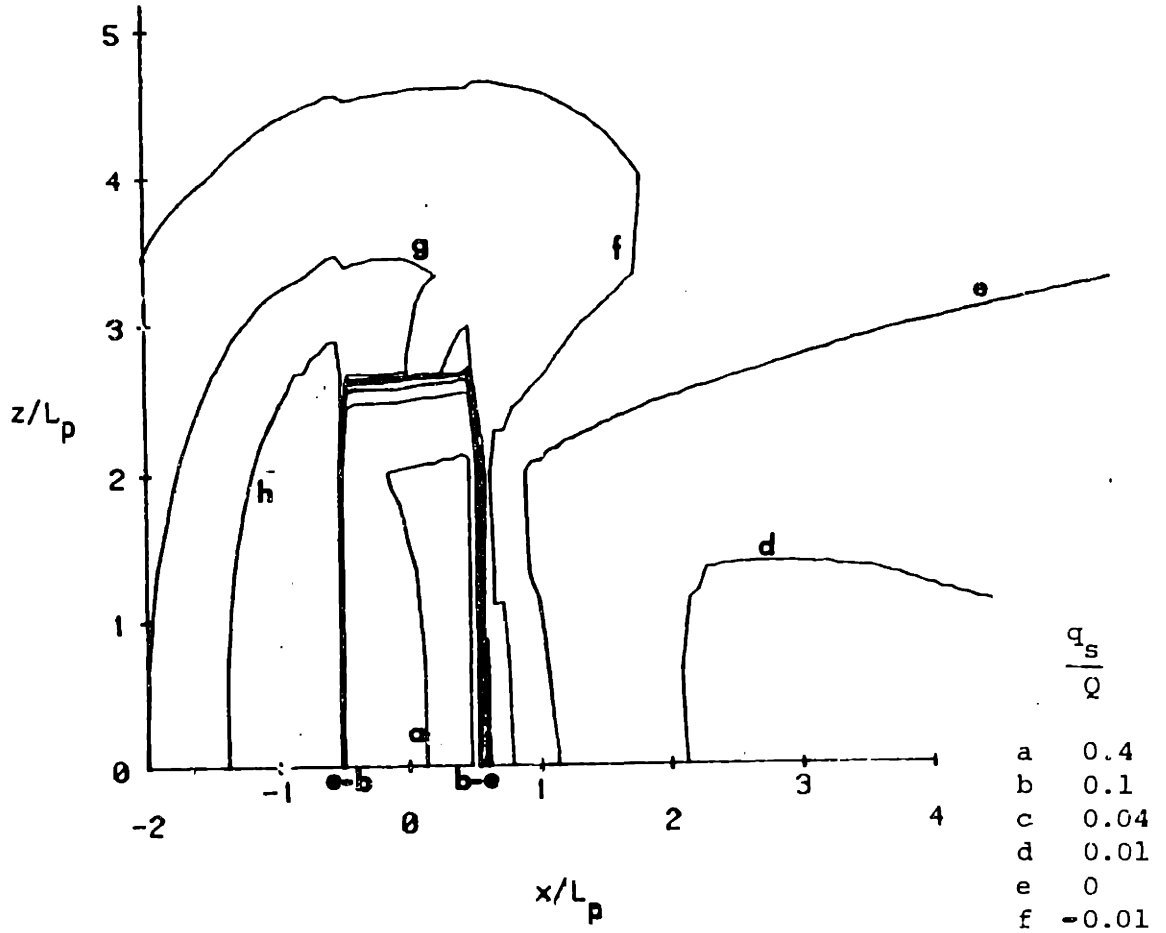

Figure 3.7 (continued)
c) Pe=16; K=1; b/a=5.

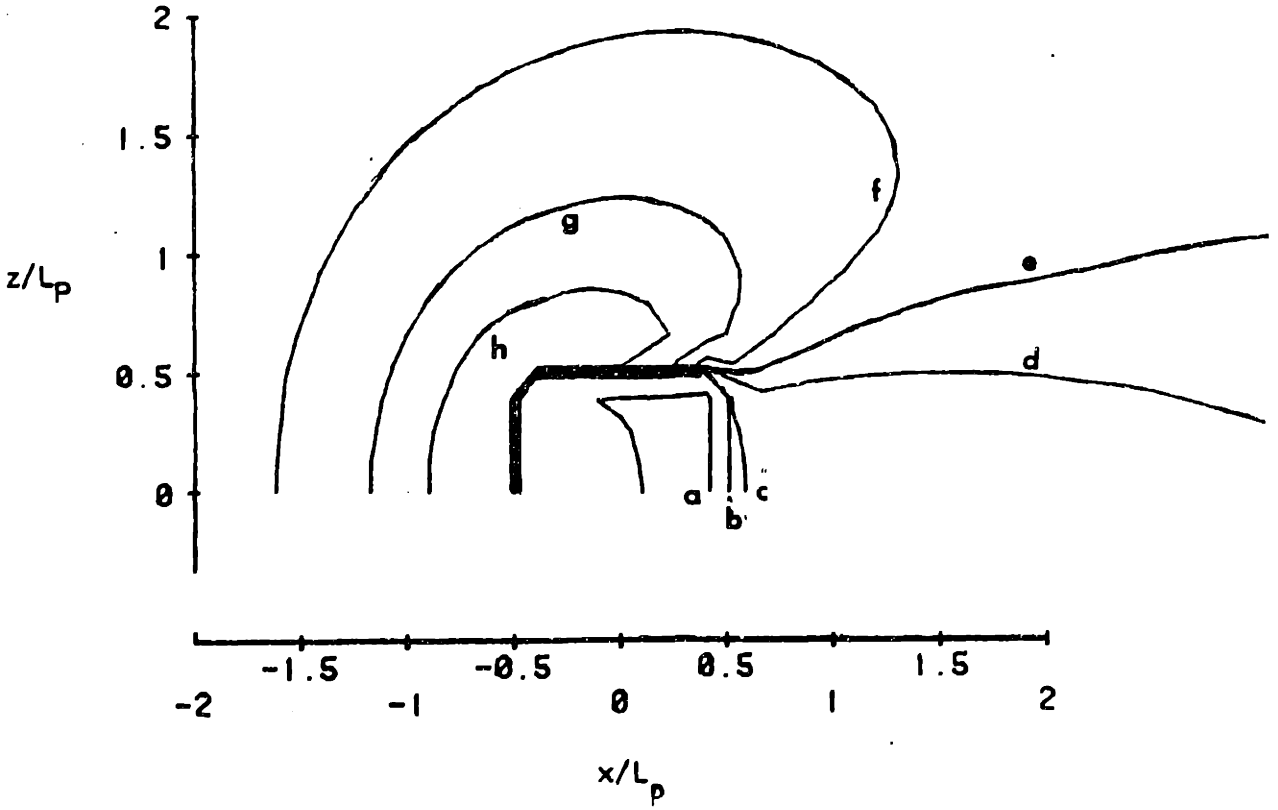

Figure 3.7 (continued)
d) Pe=64; K=1; b/a=1.

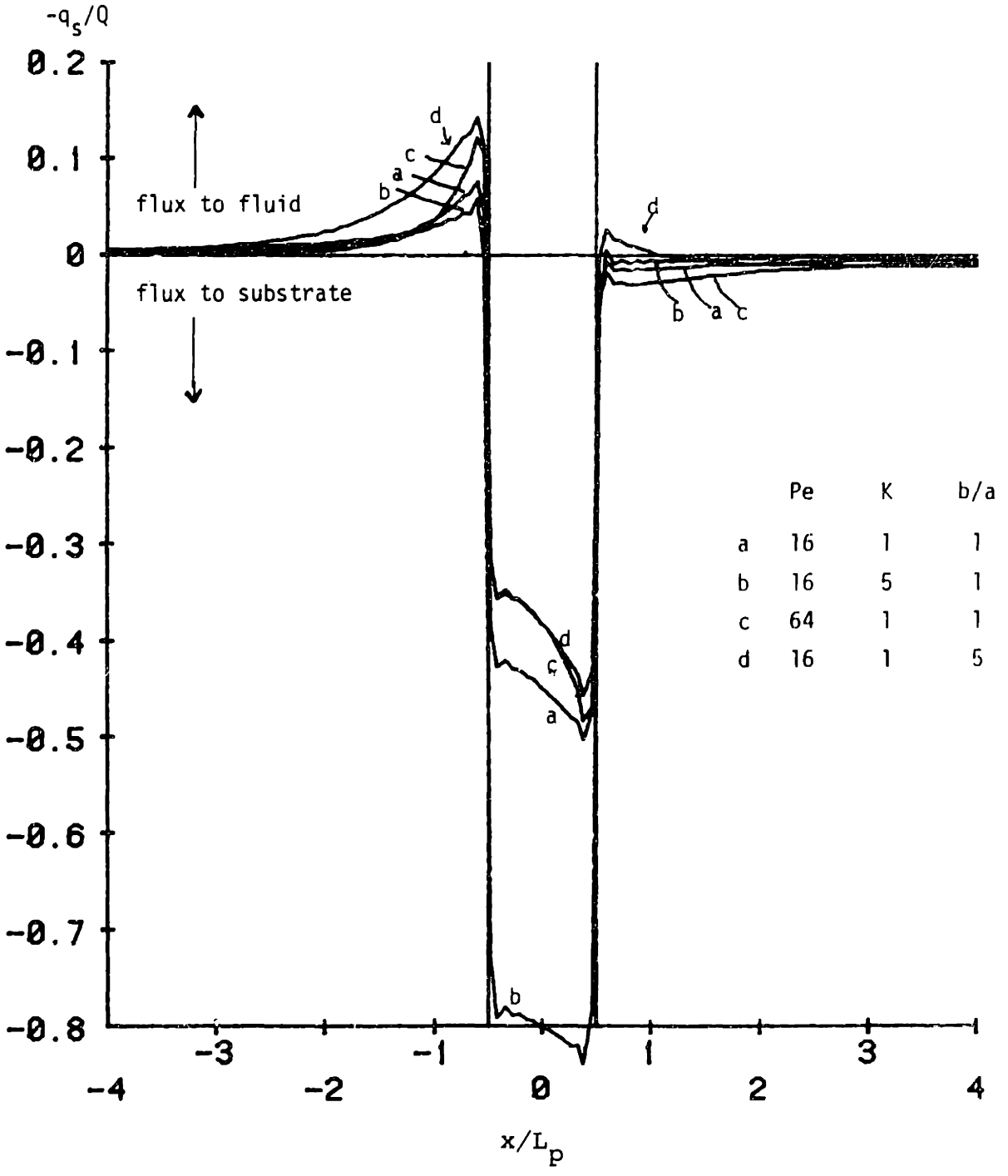

Figure 3.8 Predicted streamwise wall (y=0) heat flux distributions (z=0).

(2.9) and (2.36):

$$q_s(x,z) + q_f(x,z) = Q(x,z),\ y=0, \tag{3.1}$$

where q_f and q_s are defined in (2.36). Realizing that the source term Q is zero for (x,z) not on the probe, we can write:

$$q_f/Q = 1 - q_s/Q,\ y=0,\ (x,z) \text{ on the probe;} \tag{3.2a}$$

$$q_f = -q_s,\ y=0,\ (x,z) \text{ not on the probe.} \tag{3.2b}$$

Thus, the heat flux transferred directly to the fluid from the probe is easily obtained from the flux into the substrate by using (3.2). The vertical axis in figure 3.8 is oriented such that flux into the substrate is increasing downward. The upstream and downstream regions of figure 3.8 exhibit the character observed in the contour plots of figure 3.7.

The ripple observed in these distributions is believed to be due to a numerical problem related to Gibb's phenomenon (Kreysig 1967, p. 469) that is inherent in the technique we have used. The basic problem arises from the use of Fourier components to approximate a function having a step change. The use of a finite number of components results in an overshoot at the step and a damped oscillatory error in the vicinity of the step. The heat flux undergoes a step-like

jump at the probe edges due to the presence of the heat source. This error can be reduced by increased computational effort. We do not believe this to be necessary for our present purposes, nor do we believe that the small ripple present near the probe edges affects any of the investigations reported in this work. This is not a problem for the temperature field calculations because the variations in temperature are more gradual than those in heat flux.

These figures indicate the strong influence that substrate conductivity has on the fraction of heat generated by the probe that flows directly into the fluid. For large conductivity ratios, the heat transfer from the probe is dominated by transfer directly to the substrate rather than to the fluid. These figures also reveal that the region of heat exchange between the substrate and the fluid extends for several probe lengths in all directions from the probe. The ratio of the heat transferred directly to the fluid to that transferred directly to the substrate is highest near the leading edge and decreases smoothly along the probe. This is not unexpected because the transfer rate to the fluid decreases as the fluid is warmed by flowing along the probe. To make more detailed conclusions as to the effects of Pe, K, and b/a on the y=0 surface heat flux distributions, a study of a much wider variation of these parameters would be needed. Figures 3.9 and 3.10 present some additional details of the flux distributions. Figure 3.9 presents two parallel

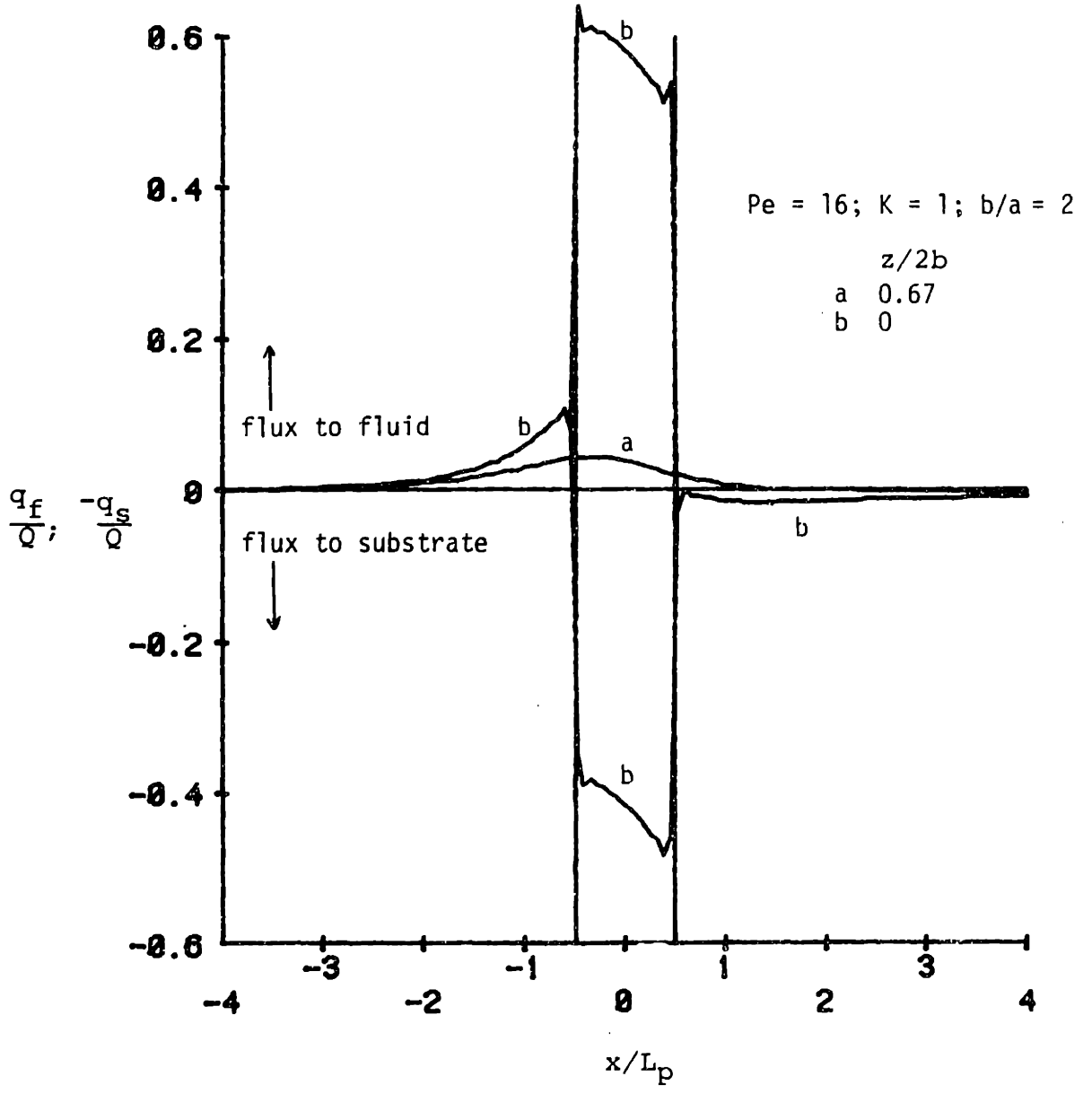

Figure 3.9 Streamwise distribution of predicted wall (y=0) heat flux at two spanwise locations (Pe=16; K=1; b/a=2).

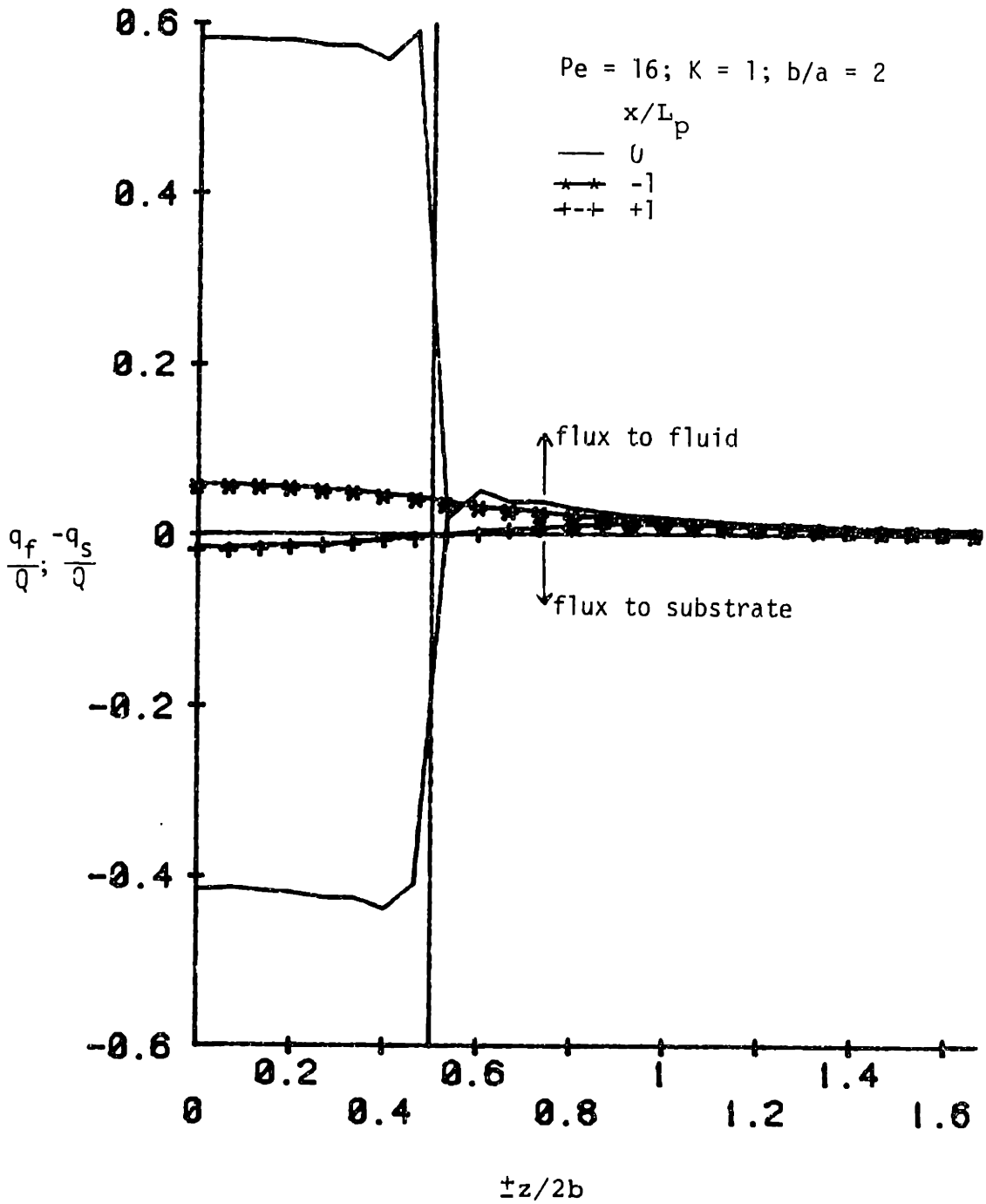

Figure 3.10 Comparison of predicted spanwise wall (y=0) heat flux distributions at three streamwise locations (Pe=16; K=1; b/a=2).

streamwise slices of the heat flux. One slice is at z=0 as in figure 3.8 and one is located at z/2b=0.67; i.e., at a spanwise location beyond the probe edge. In the region over the probe, both the flux directly to the substrate and that directly to the fluid are displayed. (The flux directly into the fluid is obtained from that into the substrate using (3.2).) The spatial variation of the partition between the fluid and the substrate of the heat generated by the probe is easily seen in this figure. The flux at z/2b=0.67 is of magnitude comparable to that near the probe along z=0 and is everywhere flowing from the substrate to the fluid. Figure 3.10 presents spanwise slices of the flux distributions at x/2a = -1, 0, and 1. The spanwise distributions illustrate the difference in the character of the upstream and downstream regions and the lateral extent of these regions of heat flow between the fluid and the substrate.

Inspection of figure 3.7 reveals that the behavior of the flux in the region downstream of the probe is sensitive to aspect ratio. For b/a=5, the region of flux to the substrate does not begin at the probes trailing edge but rather at a distance of about a half probe length beyond the trailing edge. The direction of the heat flux through the entire surface immediately surrounding the probe is from the substrate to the fluid. This is in contrast with the smaller aspect ratio probes where the region of flux from the fluid to the substrate begins immediately downstream of the probe.

This trend is taken to the extreme for the two-dimensional probe as illustrated in figure 3.11. The character of the downstream region is very different than that of the three-dimensional probes: there is no region of heat flow from the fluid to the substrate. The downstream flux very much resembles the mirror image of the upstream flux somewhat reduced in magnitude. Other trends with increasing aspect ratio are also extended: a greater portion of the probe heat flows directly to the fluid, the magnitude of the flux immediately upstream of the probe is moderately increased, and the partitioning of the probe heat between the fluid and the substrate is less uniform.

3.3 Parametric Study of Probe Nusselt Number

Governing Parameters

Examination of the governing equations (2.1-2.5) reveals 11 physical quantities that govern the problem:

T^*, the temperature,

s, the fluid shear,

k_f and k_s, the fluid and solid thermal conductivities,

α, the fluid thermal diffusivity,

P_s^*, the total power dissipation,

a^* and b^*, the characteristic source dimensions, and

x^*, y^*, and z^*, the local spatial coordinates.

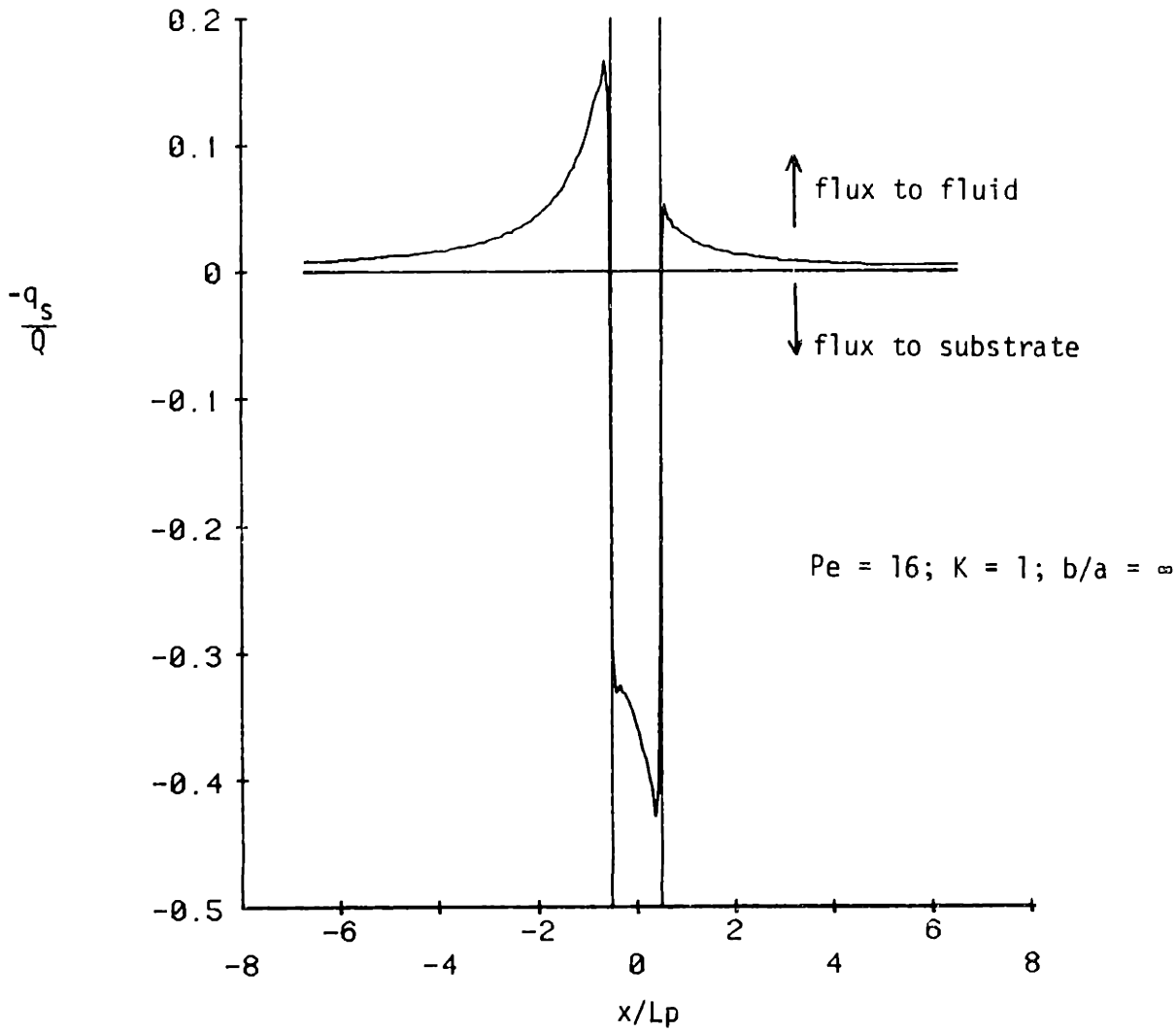

Figure 3.11 Predicted two-dimensional streamwise wall (y=0) heat flux distribution (Pe=16; K=1; z=0).

These quantities contain a total of four independent dimensions - length, time, mass, and temperature. Thus, solutions to the governing equations are expressible as a relation between four dimensionless groups that are functions of three dimensionless spatial variables. The groupings chosen for this purpose have been defined in Section 2.1 and are listed here:

T, a dimensionless temperature,

Pe, the Peclet number

K, the conductivity ratio,

b/a, the probe aspect ratio, and

x, y, z, dimensionless spatial coordinates.

An averaged quantity such as mean probe temperature or Nusselt number lacks spatial dependence. Thus the Nusselt number is expressible as a function of three independent parameters: Nu=Nu(Pe,K,b/a) where Nu is based on average probe temperature and the total heat transferred from the probe as defined in (2.46).

If the source distribution is a point source of heat, the number of independent parameters is reduced by one and we can write

$$T=T(Pe,K,x,y,z).$$

Predicted Nusselt Number Dependence

This Section presents a parametric study of the effects of Peclet number, conductivity ratio and aspect ratio on probe

Nusselt number for rectangular uniform heat source probes in the range:

$$0 \leq Pe \leq 400$$

$$0 \leq K \leq 50$$

$$0.5 \leq b/a \leq \infty$$

The predicted relationships between probe Nusselt number and these parameters are illustrated in figures 3.12-3.21. These figures are presented for several purposes:

- -to illustrate our technique's ability to deal with a great diversity of flow conditions, substrate conductivity, and probe geometry;
- -to indicate the large variations in Nu that result from this diversity of governing parameters thus underscoring the necessity of using a technique that properly accounts for the physics; and
- -to provide a base of information for probe design and development.

A complete listing of the Nusselt numbers for the 74 cases calculated in this study as well as the corresponding zero Peclet number values is presented in Appendix E. The two most common geometries investigated in this study are a square probe and a two-dimensional probe. These were selected to illustrate the extremes of three-dimensionality and two-dimensionality.

Figure 3.12 shows the predicted Nu vs $Pe^{1/3}$ behavior parametric in conductivity ratio K for a fixed aspect ratio

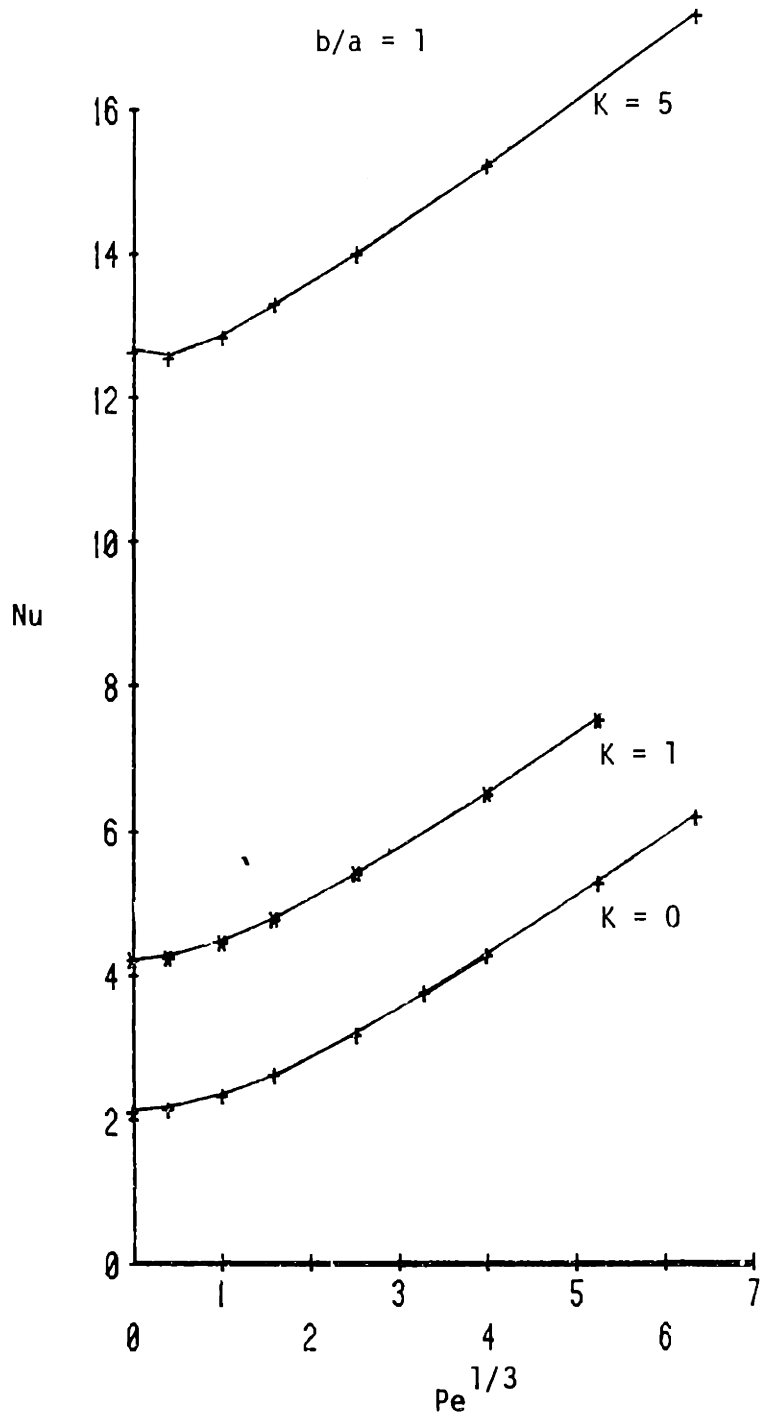

Figure 3.12 Predicted probe calibration curve variation with conductivity ratio (b/a=1; K=0-5).

probe (b/a=1). Such curves represent the predicted "calibration curves" analogous to those obtained in laboratory calibrations. The curves exhibit the familiar linear relationship between Nu and $Pe^{1/3}$ at moderate to large Pe. They also highlight the very strong influence of substrate conductivity. As K increases, the curves retain a similar shape but are translated upwards to larger Nu so that the change in Nu with shear (Pe) becomes only a small fraction of the total Nusselt number - i.e., the heat transfer is dominated by conduction. For example, for K=5 and b/a=1, the change in Nu between Pe=1 and Pe=34 is 2.4, while Nu=12.7 for zero flow (Pe=0). Thus for an increase in Pe by a factor of 64, the total heat transfer increases only about 15%. For larger conductivity ratios, this fraction becomes even smaller. This domination of the heat transfer by conduction is further illustrated in figure 3.13 where the calibration curves of figure 3.12 are replotted with those of larger K - up to K=50. Such curves obtained for probes of other aspect ratios show similar trends. Figure 3.14 presents Nu as a function of Pe for a variety of conductivity ratios for a two-dimensional probe. The sensitivity of Nu to K is substantial although less than that of a square probe.

The predicted influence of aspect ratio is presented in figure 3.15 for a probe mounted on an adiabatic wall. The effect of varying the aspect ratio is much less dramatic than that of varying the conductivity ratio, but it is still quite

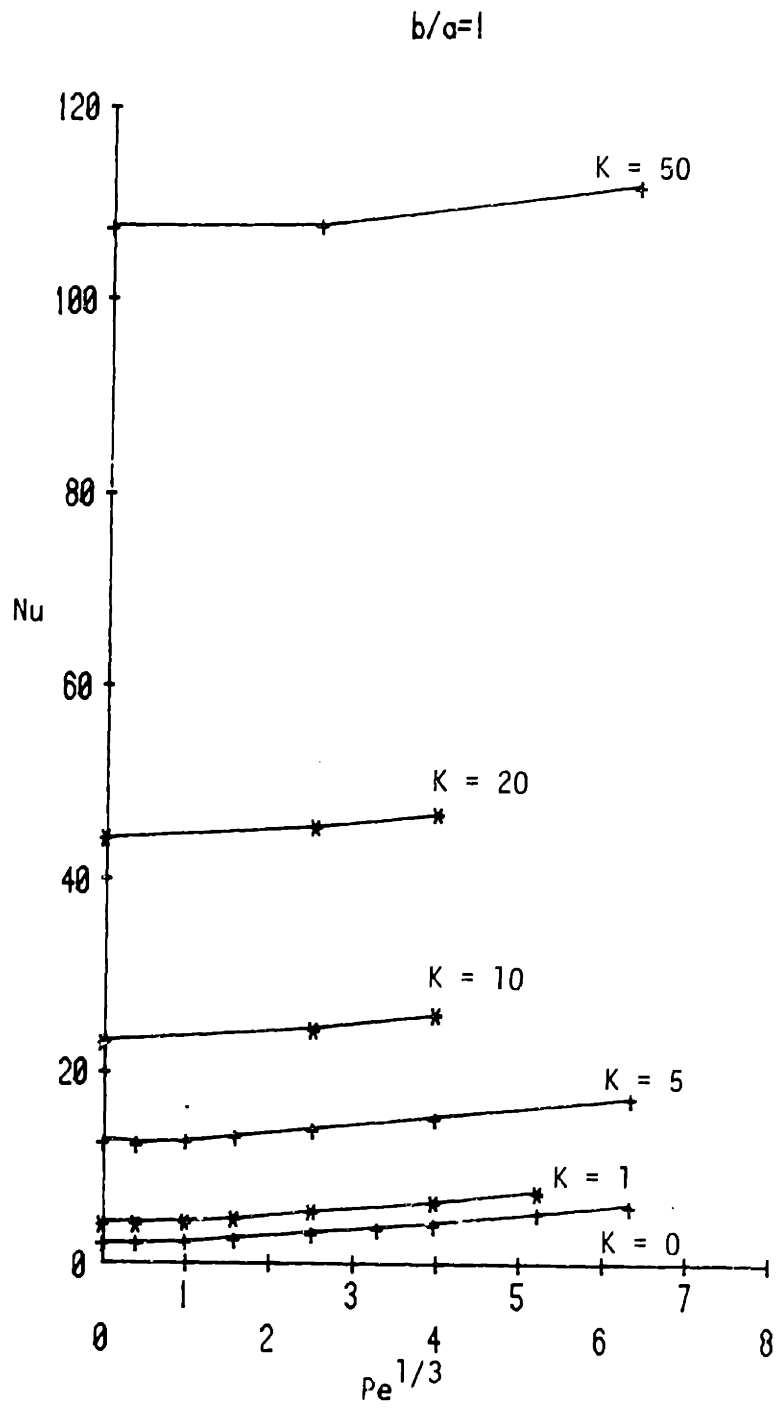

Figure 3.13 Predicted probe calibration curve variation with conductivity ratio (b/a=1; K=0-50).

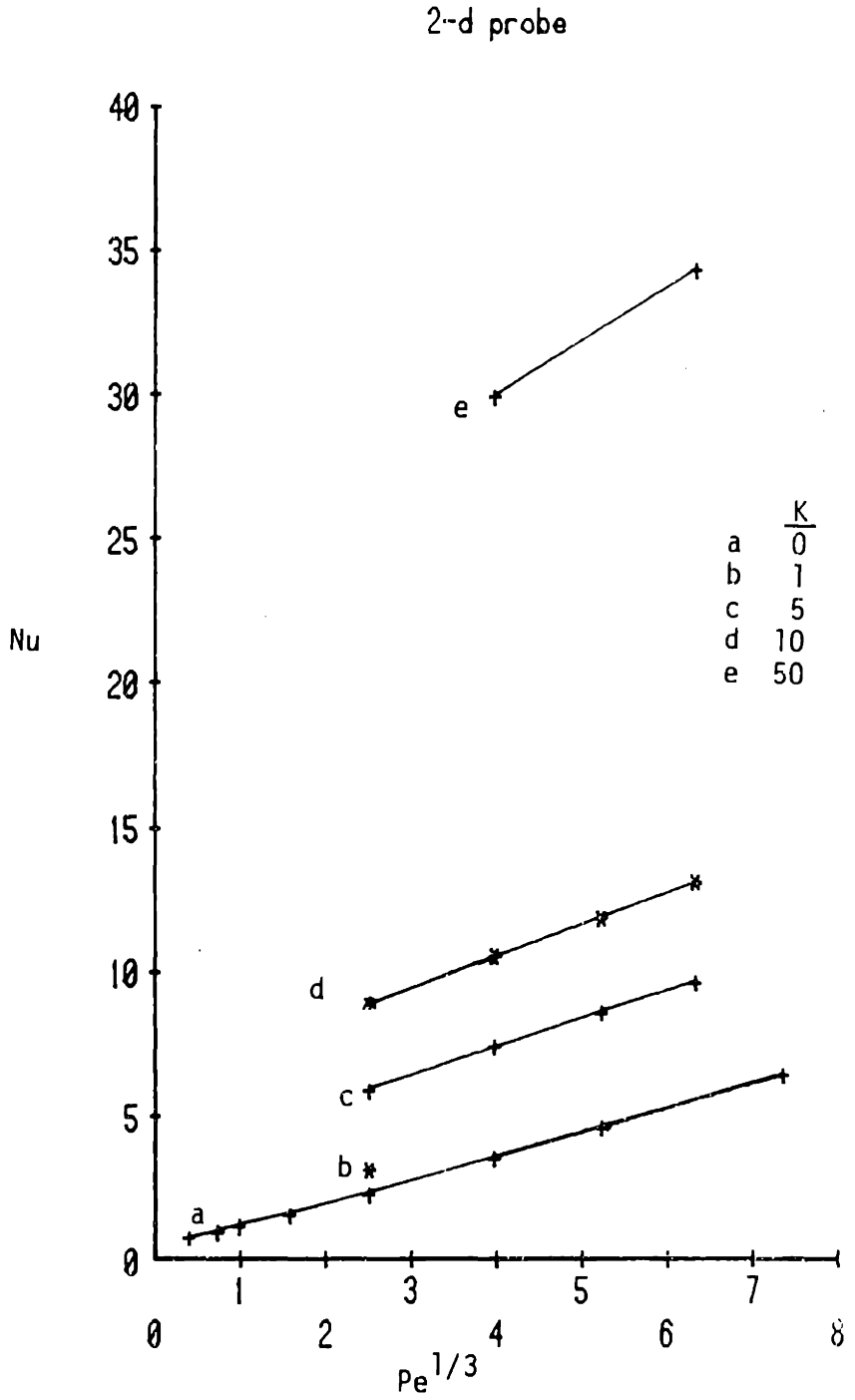

Figure 3.14 Predicted probe calibration curve variation with conductivity ratio for a two-dimensional probe.

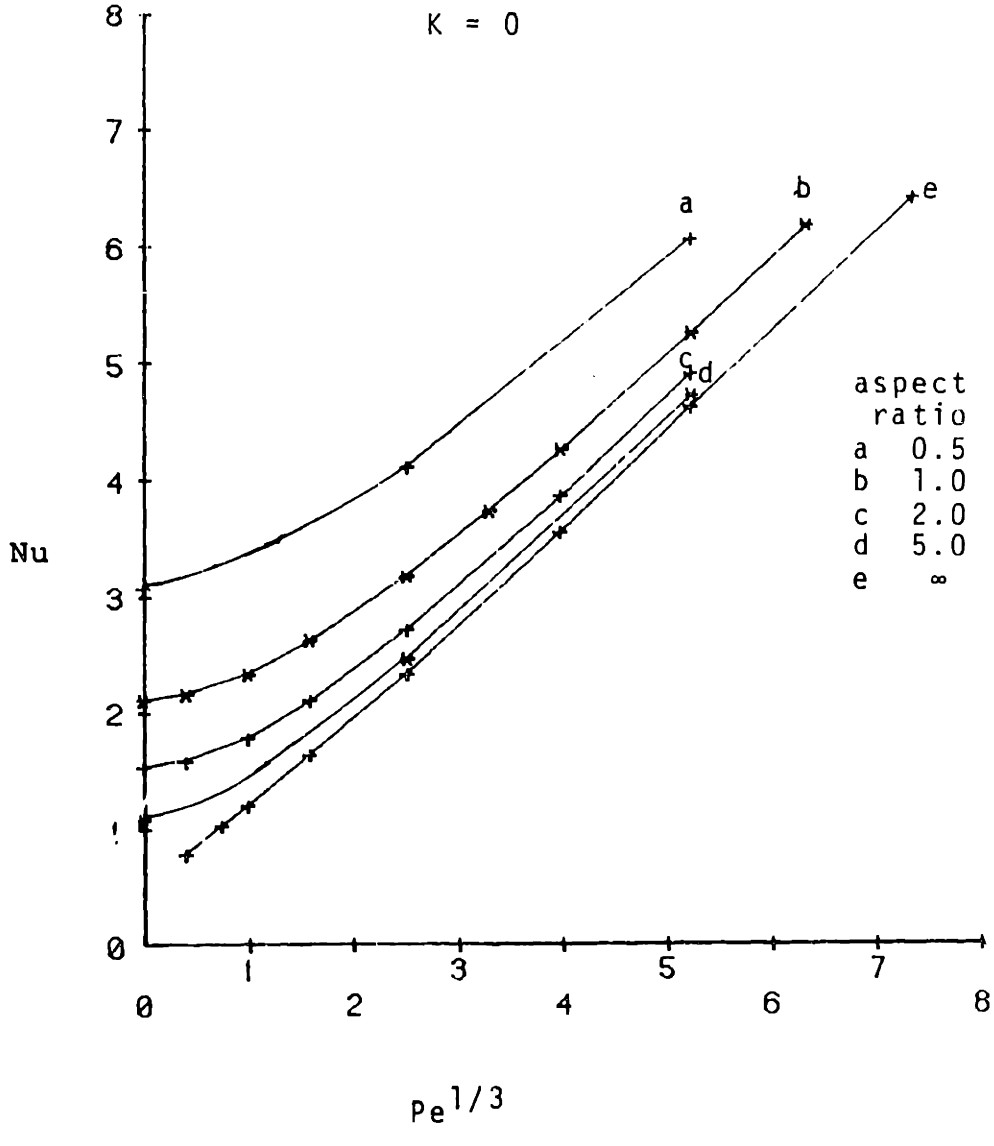

Figure 3.15 Predicted probe calibration curve variation with aspect ratio (K=0).

significant. Predicted values of Nu decrease asymptotically to those for infinite aspect ratio as b/a increases. The absolute difference between the predicted values of Nu for a square probe and a two-dimensional probe is largest for small Pe and decreases with increasing Pe. Similar trends are exhibited when substrate conductivity is included as is shown in figure 3.16 for a value of K=5. The difference in the Nusselt numbers of square and two-dimensional probes is much larger for K=5 than for K=0. (This is also illustrated in figures presented later in this Section.) The sensitivity of probe Nusselt number to aspect ratio is greatly enhanced by large conductivity ratios.

Figures 3.17-3.21 present the predicted Nusselt number variation with conductivity ratio parametric in Peclet number and aspect ratio. The most striking feature of these figures is the strongly linear relation between Nu and K, particularly for small aspect ratios. The slope of these lines is a function primarily of aspect ratio and nearly independent of the flow and the conductivity ratio - as illustrated by the nearly parallel nature of the curves in figures 3.17 and 3.18. The intercept at K=0 is a function of both Peclet number and aspect ratio. The case of pure conduction to the substrate and a stagnant fluid exhibits this behavior exactly as shown by combining (2.63) and (2.47) to obtain:

$$Nu(Pe=0,K,b/a) = (K+1)\ Nu(Pe=0,K=0,b/a). \qquad (3.3)$$

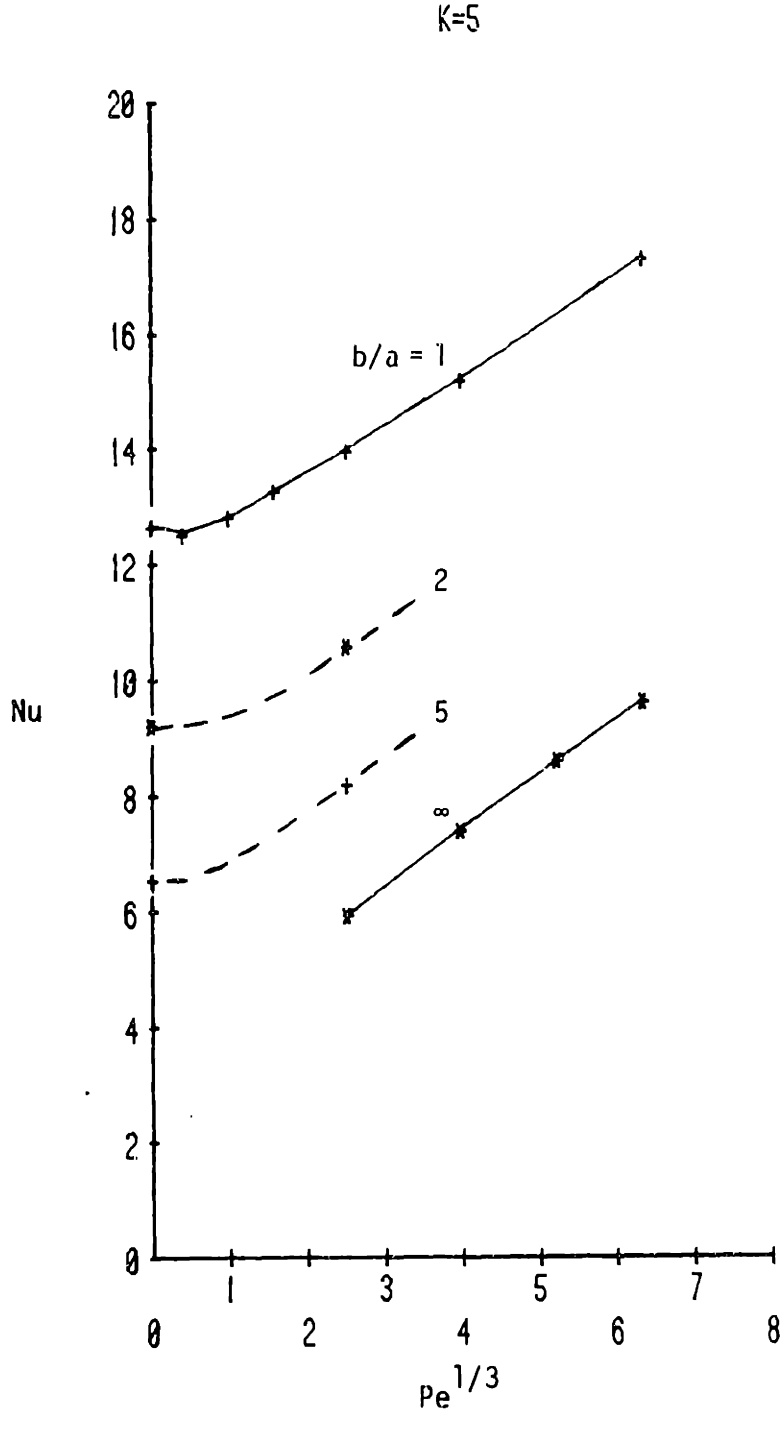

Figure 3.16 Predicted probe calibration curve variation with aspect ratio (K=5).

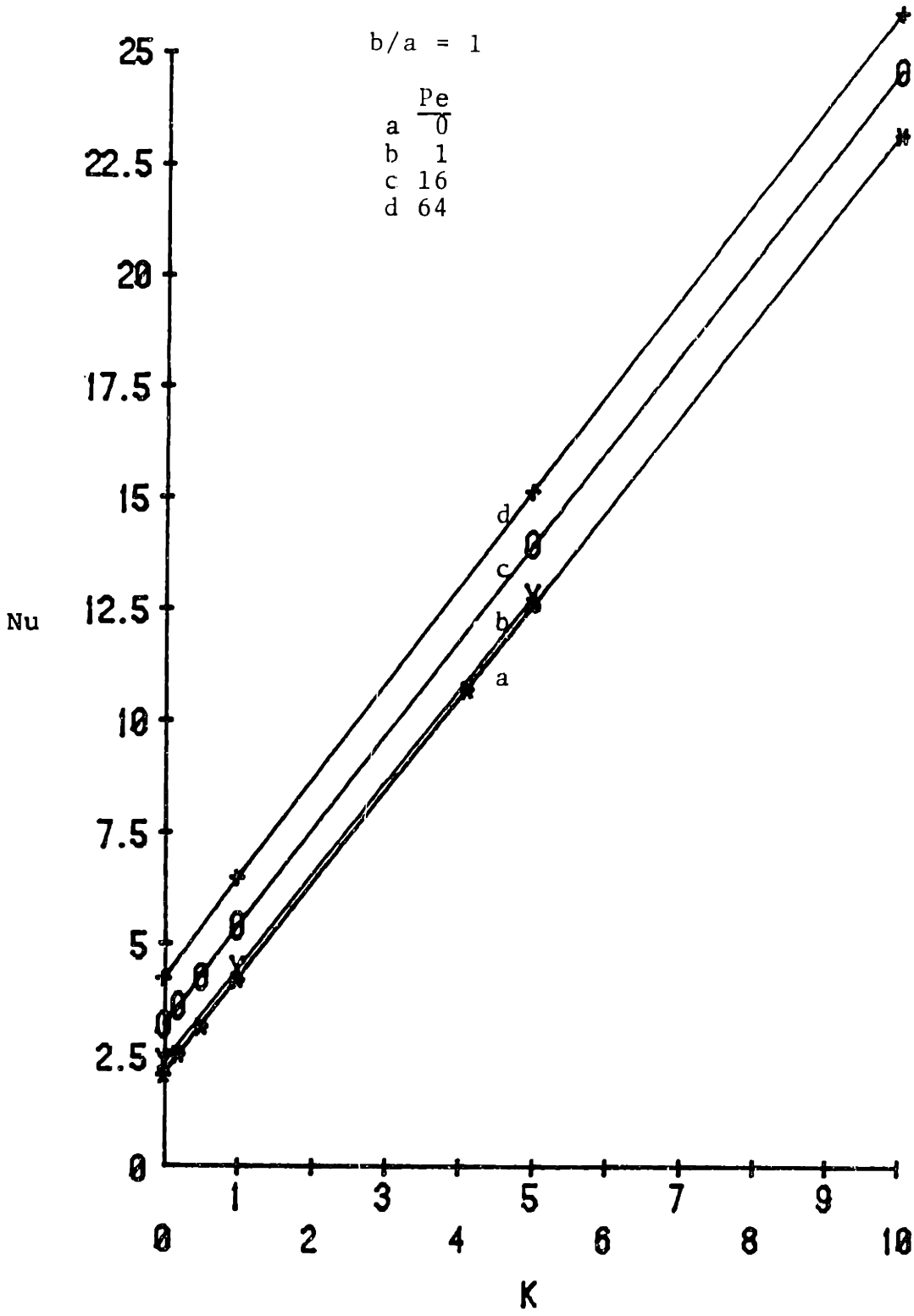

Figure 3.17 Relation between predicted probe Nusselt number and conductivity ratio (b/a=1; K=0-10).

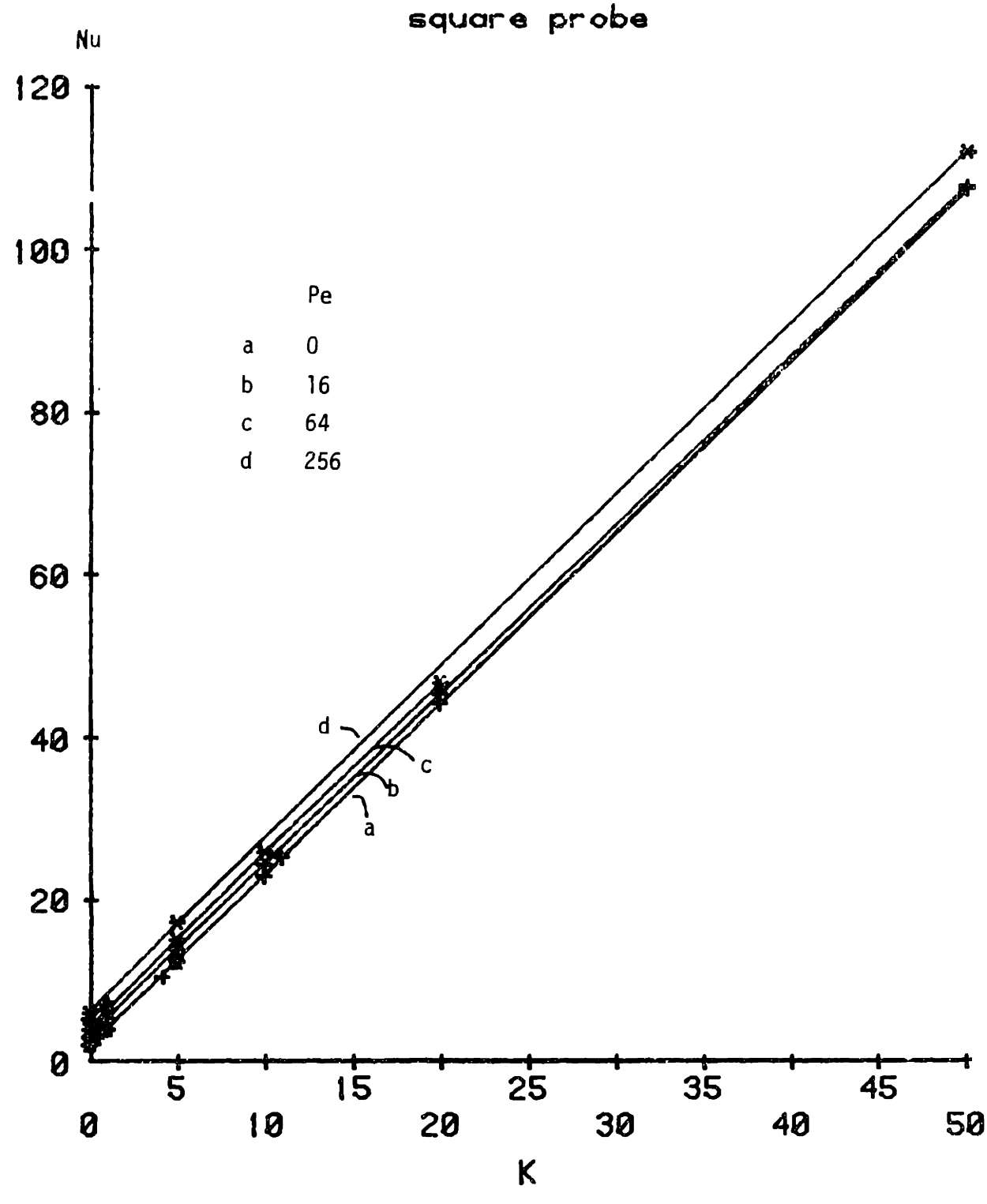

Figure 3.18 Relation between predicted probe Nusselt number and conductivity ratio (b/a=1; K=0-50).

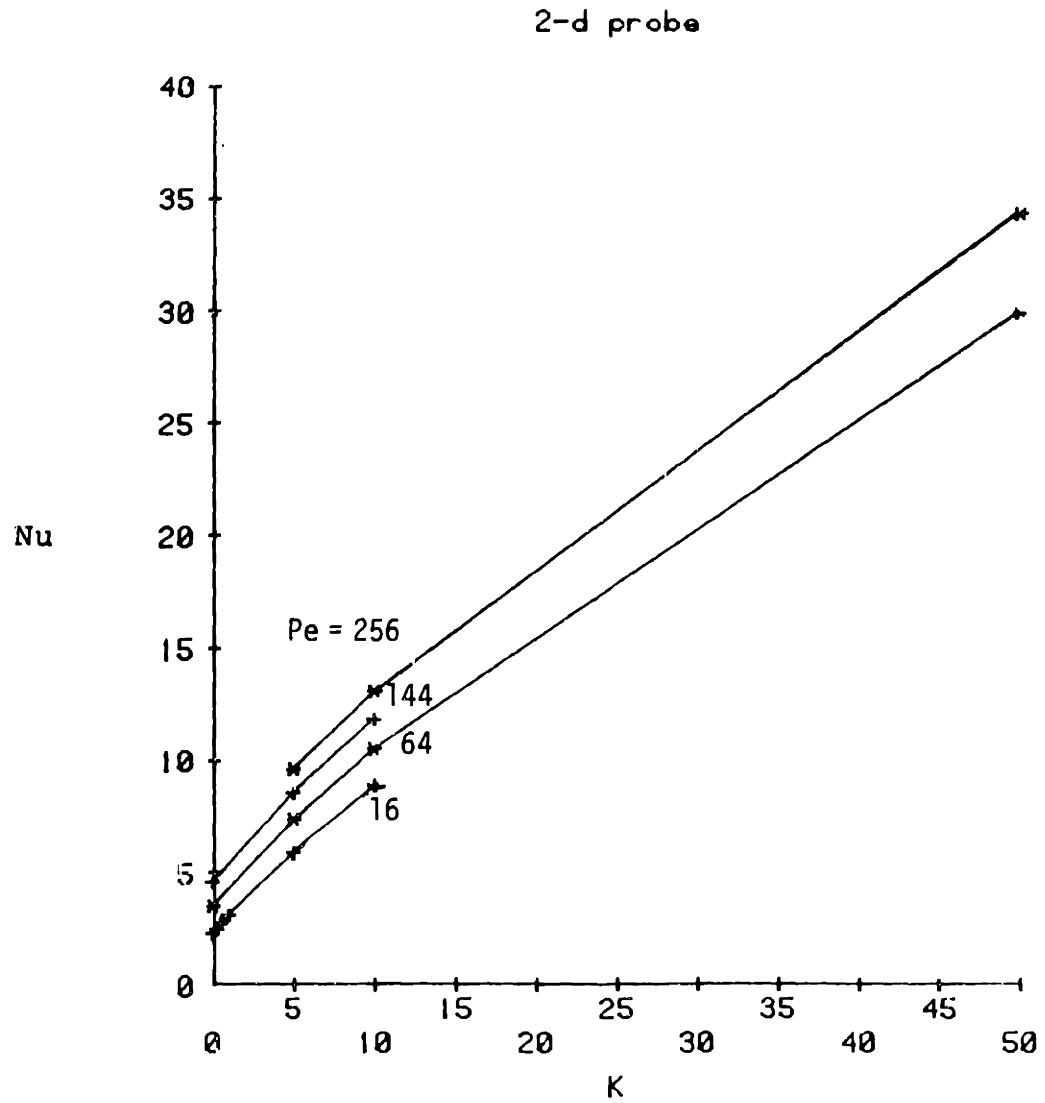

Figure 3.19 Relation between predicted probe Nusselt number and conductivity ratio for a two-dimensional probe.

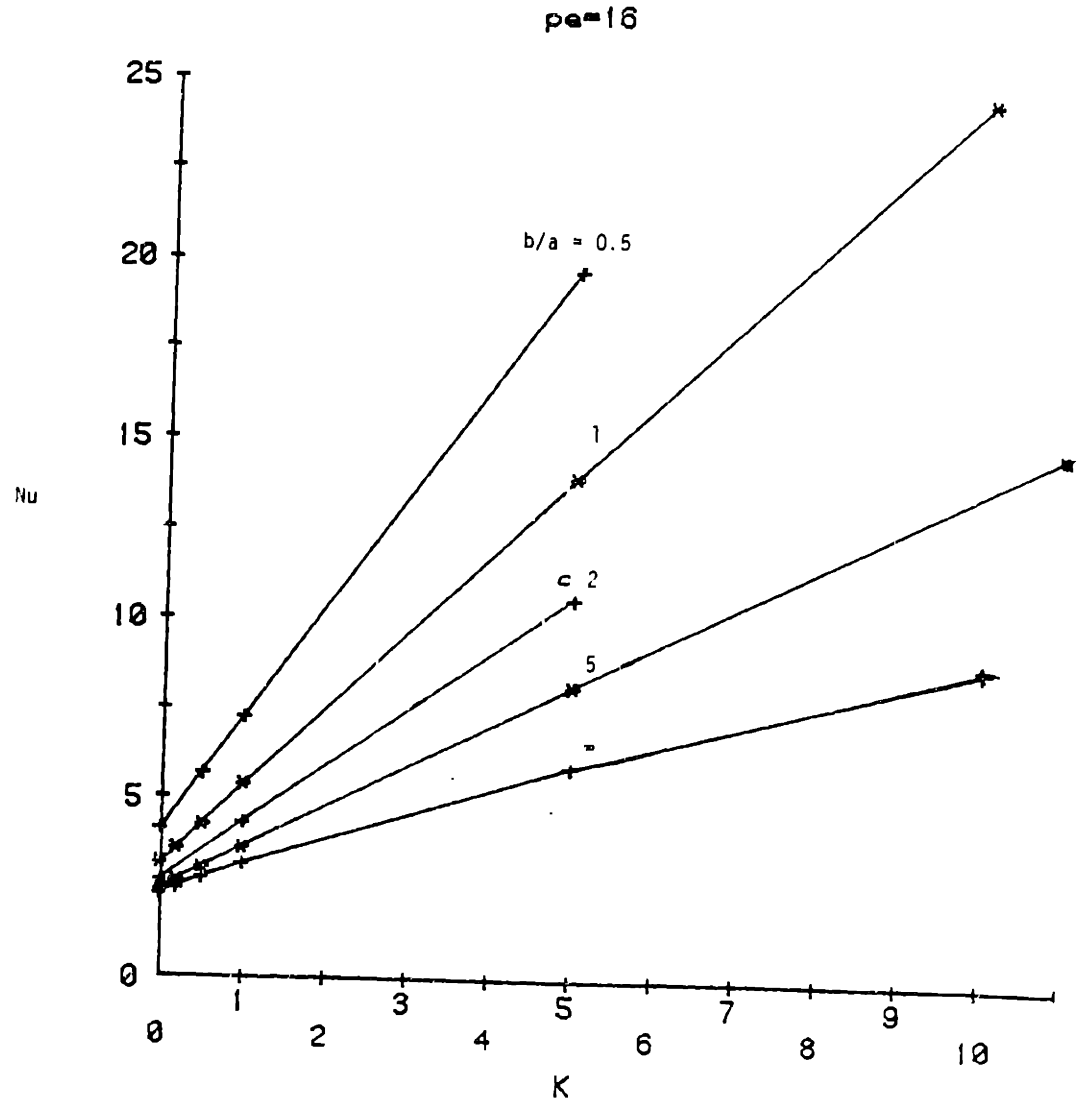

Figure 3.20 Predicted probe Nusselt number variation with conductivity ratio (Pe=16).

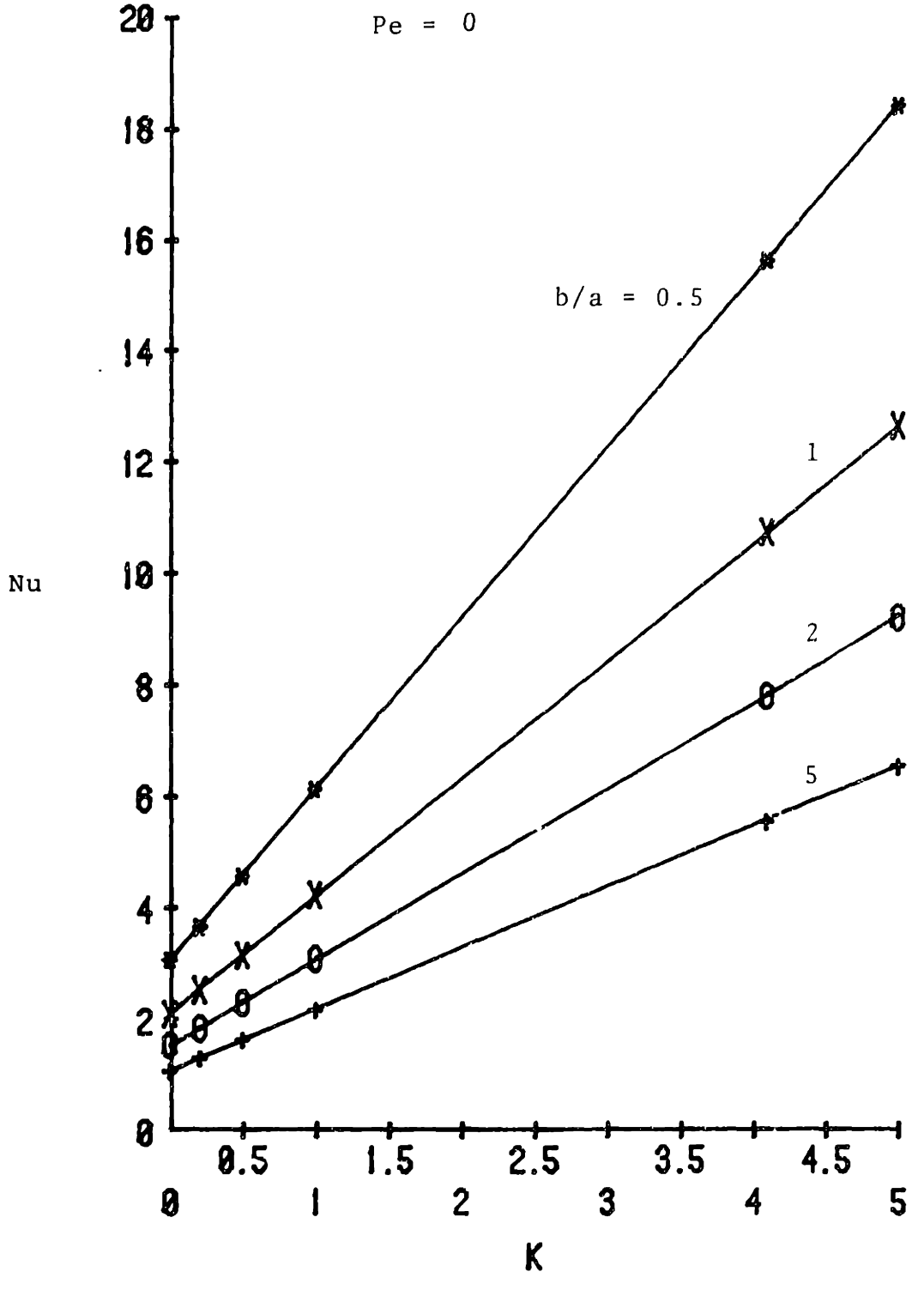

Figure 3.21 Predicted probe Nusselt number variation with conductivity ratio (Pe=0).

The Nusselt numbers of two-dimensional probes exhibit the least linearity, but even their nonlinearity is minor over large ranges of K. The implications of this behavior are discussed in Chapter 4.

4. Discussion

In this Chapter we first examine the ranges of Peclet number and conductivity ratio that are encountered in hot-film applications for typical flows and a wide range of fluids and substrate materials. A comparison of our predictions with previous theory and experiment shows excellent agreement with limiting value theories and consistency with available experimental data. The coupling between the fluid and substrate heat transfers is found to be weak. This leads to a simplified expression that accurately approximates our probe Nusselt number predictions. Effects of spatial variation of substrate conductivity are briefly examined. A substrate composed of materials of different thermal conductivities is found to influence the slope of probe calibration curves. Estimates of the effects of natural convection, thermal radiation, conduction within the heated film, and temperature dependent probe resistivity are presented.

4.1 Probe Operating Conditions

Previous and potential uses of hot-film probes cover wide ranges of conductivity ratio and Peclet number. Both of these parameters depend upon the probe's environment as well as its design: for a given flow situation, the thermal properties of the fluid and the shear stress are environmentally imposed

while the probe size and substrate conductivity can be specified by the design.

Relation Between Reynolds and Peclet Numbers

One of the most common ways of describing a flow is to specify its Reynolds number. The Reynolds number is related to momentum exchange and is usually based on the characteristics of the flow field as a whole (e.g., a pipe diameter or a free stream velocity). The Peclet number with which we deal, however, is based on heat exchange and local quantities that are measured on the scale of the probe. To relate the Peclet number to the Reynolds number, it is necessary to specify the fluid properties, the flow field, and the specific probe design.

It is instructive to examine the relationships between the probe Pe and the flow Re for some nominal probe sizes. Recall that the Peclet number is expressible as:

$$Pe = L_p^2 = L_p^{+2}\, Pr$$

Expanding L_p^+,

$$Pe = L_p^{*\,2}\, \frac{\tau_w}{\rho\, \nu^2}\, Pr$$

$$= \left(\frac{L_p^*}{L^*}\right)^2 \frac{\tau_w}{\rho V^{*2}} \left(\frac{L^* V^*}{\nu}\right)^2 Pr$$

where L^* is the flow field characteristic length and V^* is its

characteristic velocity. The quantity L^*V^*/ν is simply the flow Reynolds number Re. Thus we can write:

$$Pe = \frac{\tau_w}{\rho V^{*2}} Re\ Pr \left(\frac{L_p^*}{L^*}\right)^2 \qquad (4.1)$$

The first term on the right, $\tau_w/\rho V^{*2}$, is the familiar quantity proportional to the friction factor in internal flows and to the skin friction coefficient in external flows. This quantity is expressible as a function of Reynolds number and perhaps other parameters (e.g., roughness). In many applications, however, it can be simply related to a power of the Reynolds number:

$$\frac{\tau_w}{\rho V^{*2}} = \frac{C}{Re^n} \qquad (4.2)$$

where C and n are constants determined by the specific flow. Thus the Peclet number depends upon the Reynolds number, the Prandtl number, the flow shear stress - Reynolds number relation, and the relative sizes of the probe and the characteristic flow length.

Combining (4.1) and (4.2) yields:

$$Pe = C\ Re^{2-n}\ Pr \left(\frac{L_p^*}{L^*}\right)^2 \qquad (4.3)$$

or

$$Pe = C\ Re^{2-n}\ \tilde{Pr} \qquad (4.4)$$

where

$$\tilde{Pr} = Pr\left(\frac{L_p^*}{L^*}\right)^2 . \qquad (4.5)$$

$\tilde{Pr}$ can be viewed as a modified Prandtl number representing the ratio of the characteristic time for diffusion of heat in the vicinity of the probe (L_p^{*2}/α) to the characteristic time for diffusion of momentum in the main flow (L^{*2}/ν). Values of C and n for laminar and turbulent flows over smooth flat plates and through smooth pipes are presented in table 4.1 as examples.

Figure 4.1 illustrates the relation between Reynolds number and Peclet number for smooth pipes. The relation is presented as a family of curves parametric in $\tilde{Pr}$. Also marked are the curves for air and water flows at room temperature for values of $L_p^*/D=0.005$ where D is the pipe diameter (e.g., $L_p^*=0.1$mm and D=2cm, which are fairly typical values.) Figure 4.2 presents the same type of curves for boundary layer flow over a smooth flat plate. It is apparent from these plots that a large range of Peclet number is encountered by consideration of even relatively ordinary flows. It is also apparent that the Peclet number is most sensitive to the probe streamwise length - L_p^* - or more specifically to the size of L_p^* relative to the characteristic flow length.

	Flat Plate Boundary Layer	Pipe Flow
V^*	freestream velocity	mean velocity
L^*	distance from leading edge	diameter
Laminar:		
C	0.332	8
n	0.5	1
Turbulent:		
C	0.0288	0.04
n	0.2	0.25

$$\frac{\tau_w}{\rho V^{*2}} = \frac{C}{Re^n} \qquad Re = \frac{V^* L^*}{\nu}$$

$$Pe = C\, Re^{2-n}\, Pr \left(\frac{L_p^*}{L^*} \right)^2$$

Table 4.1 Parametric Values for Shear Stress-Reynolds Number Relation. (See White 1974 and Rohsenow and Choi 1961.)

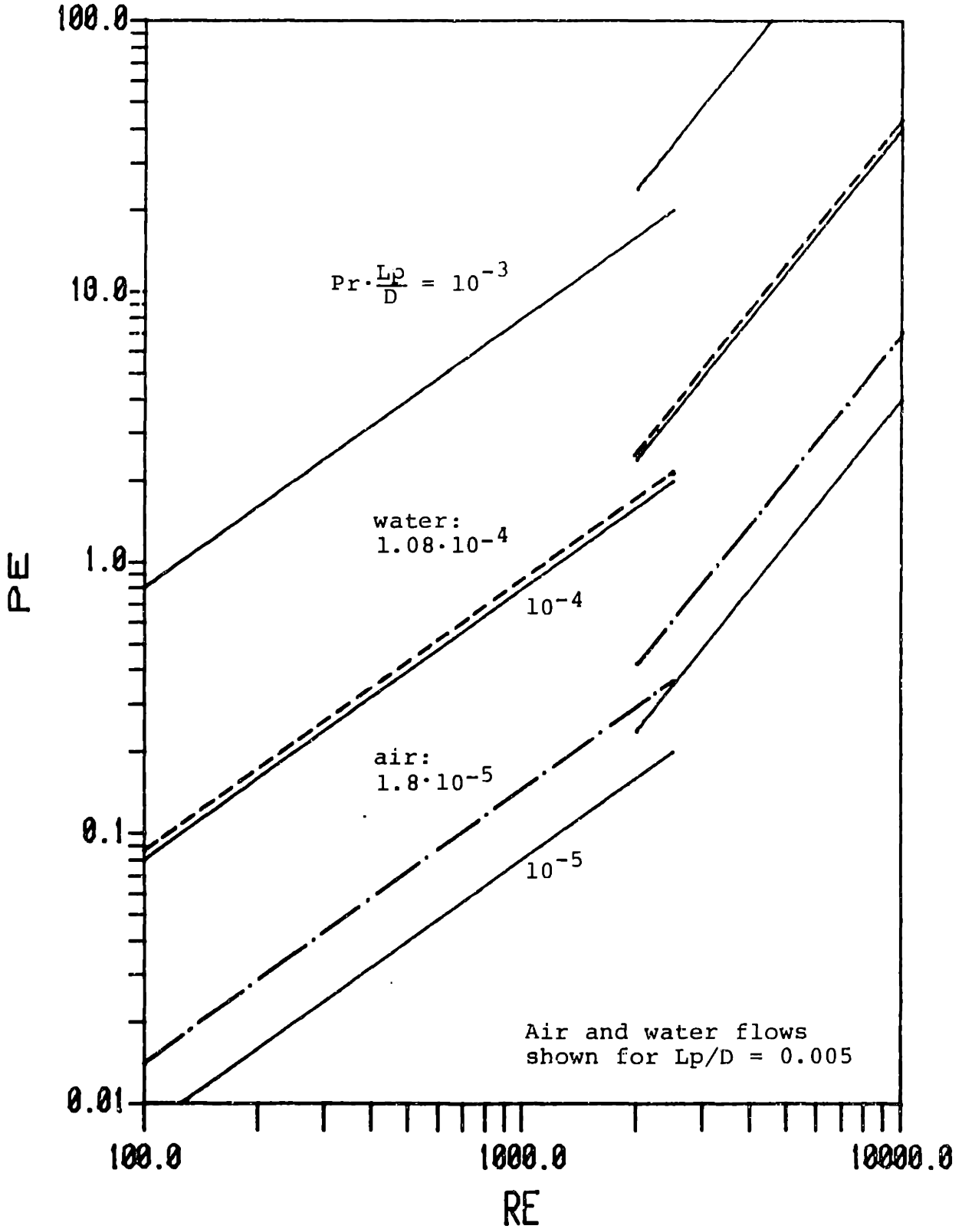

Figure 4.1 Relation between Reynolds and Peclet numbers for flow in smooth pipes.

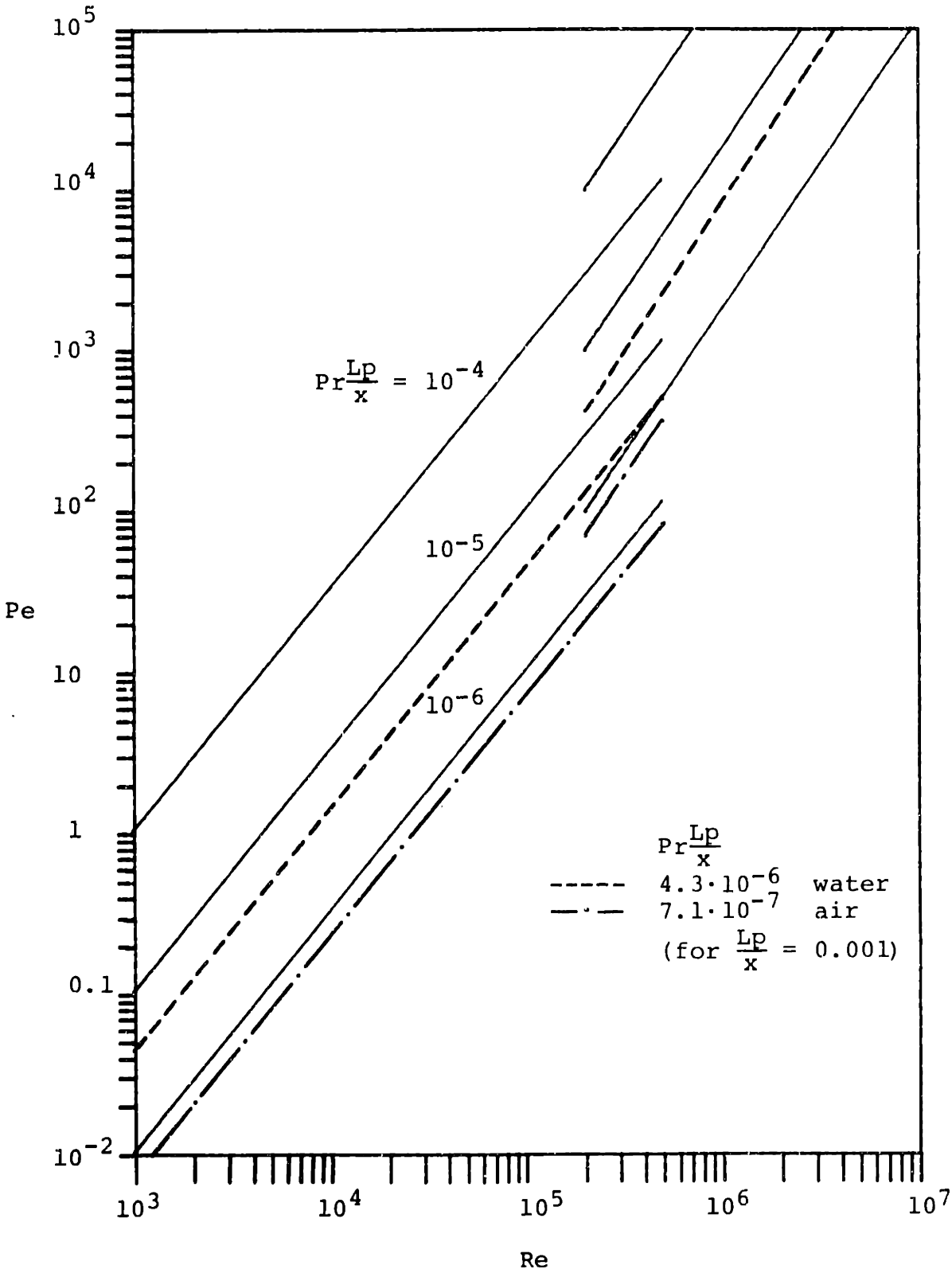

Figure 4.2 Relation between Reynolds and Peclet numbers for flow over smooth flat plates.

Thermal Conductivity Ratios

Thermal conductivities of materials vary widely. Thus, the value of K also varies widely depending upon the probe substrate material and the fluid in which measurements are made. (As we demonstrate in Section 4.5, probe performance may also depend on the conductivity of the material in the immmediate vicinity of the probe even if it is not part of the fabricated substrate. Such material might be part of the wall in which the probe is mounted.) Values of thermal conductivity are also somewhat temperature dependent. Table 4.2 lists the thermal conductivities of several common fluids and a wide range of solid materials evaluated at temperatures typical of the "film" temperature (the average of the probe and ambient temperatures) for operation in that medium. Also tabulated are the values of K for the various fluid - substrate combinations. The conductivities of most ceramics lie within a factor of two of those for pyrex and quartz. Similarly, the conductivities of most plastic materials are within about a factor of two of that of plexiglas.

In steady state, it is desirable to have a small K to decrease the background component of the measurement. This suggests one should select the lowest possible thermal conductivity material for the substrate, particularly for use with flows of gases which have lower conductivities than liquids. Substrate material selection, however, involves more

	k_s \ k_f	AIR	FREON	SILICON OILS	GLYCERINE	HUMAN BLOOD	WATER
		0.26 - 0.32	0.7	1 - 16	3	5.5	6.4 - 6.8
styrofoam	0.4	1.3 - 1.5	.57	.025 - .40	.13	.07	.059 - .063
plexiglass	1.5	4.7 - 5.8	2.1	.094 - 1.5	.50	.27	.22 - .23
bakelite	1.4 - 5.0	4.4 - 19	2.0 - 7.1	.31 - 5	.47 - 1.7	.25 - .91	.21 - .78
pyrex glass	11	34 - 42	16	.69 - 11	3.7	2.0	1.6 - 1.7
quartz	19	59 - 73	27	1.2 - 19	6.3	3.5	2.8 - 3.0
Cd-Te	35 - 70	110 - 270	10 - 50	2.2 - 70	12 - 23	16 - 13	5.2 - 11
steel	170 - 600	530 - 2300	240 - 860	10 - 600	57 - 200	31 - 110	27 - 250
silicon	750 - 1500	2300 - 5800	1100 - 2100	47 - 1500	250 - 500	140 - 2700	110 - 220
aluminum	900 - 2600	2800 - 10000	1300 - 3700	56 - 2600	300 - 870	160 - 470	130 - 400

k_f and k_s expressed in $\frac{\text{BTU}}{\text{cm°C}}$; property values from Kaminski (1977)

Table 4.2 Ratios of Substrate to Fluid Thermal Conductivities for Various Substances.

than thermal concerns. Structural properties, bonding of the film to the substrate, and fabrication are all important. Such concerns have, in the past, usually led to the selction of quartz or pyrex as the substrate material, although some plastics have been used. It appears, then, that one is faced with having a large component of substrate conduction for air flows - a K of at least 1 and more likely 10-60 or more. Water flows have values of K that are lower by about a factor of 20. The most common conductivity ratios currently in use then are for quartz/water (K=3), quartz/air (K=65), and perhaps "plastic"/water (K=0.2-1.0) and "plastic"/air (K=4-20).

Operating Conditions of Previous Researchers

As an illustration of the wide ranges of the governing parameters that occur in practice, table 4.3 provides a list of the values of Pe, K, and b/a as well as the liquid and substrate materials and some comments on the flow conditions of a number of previous investigations which have employed hot-film shear stress probes. The values here are only best estimates from the information available. Calibrations are usually not made in dimensionless form, and so the governing parameters must be estimated. In some cases, necessary information was not available and an estimate of a particular parameter is not presented.

RESEARCHER	FLUID	SUBSTRATE	PECLET NUMBER	ASPECT RATIO	COMMENTS
Blinco & Simons (1974)	water	quartz/plexiglas	300 - 3000	4	instantaneous turbulence measurements
Reichardt & Azad (1977)	air	quartz	10 - 125		
Bellhouse & Schultz (1967)	air	pyrex/nylon plug		circular	
Gougat, et. al. (1966)	air	teflon	20 - 120	5	mean turbulence measure
Brown (1967)	air	pyrex		3	laminar & turbulent flow
Brown & Davey (1971)	air	pyrex	0.1 - 1.0	3	laminar flow

Table 4.3 Probe Operating Conditions of Other Selected Researchers.

We also list here, as an indication of typical hot-film design, the nominal size and composition of several "off-the-shelf" probes (DISA 1980 and TSI, Inc 1978):

	TSI 1237, 1237W, 1268	DISA 55R45, 55R46	DISA 55R47
dimensions (mm)	0.4 x 1.2	0.2 x 0.75	0.1 x 0.9
b/a	3	3.75	9
substrate	quartz	quartz	polyimid foil
sensor	platinum	nickel	nickel

The DISA 55R47 is made similar to a strain gauge and is glued onto the surface. Some flow disturbance might be expected from this, and one would also expect an effect of the thermal conductivity of the wall. It is not coated to be used in liquid flows. The other two designs are of that described previously - mounted in the wall flush with the surface.

4.2 Comparison of Predictions with Previous Theory

As discussed in Chapter 1, all previous theories are less

comprehensive than ours and involve a number of approximations and simplifications (table 1.1). Nevertheless, it is instructive to investigate the differences between the present theory and previous ones and to check for consistency under conditions for which the simplifications apply. In this Section, we first present the predictive comparison with other theory and the appropriate asymptotic limits.

Figure 4.3 presents our predictions of probe Nusselt number for various values of K and b/a over four orders of magnitude of Pe. These results are compared to the appropriate asymptotic limits for zero flow and for two-dimensional adiabatic wall high Pe flow (the classical Leveque solution). The low Pe asymptotic behavior comparison is seen to be excellent. (The low Pe asymptote is the zero-flow limit. No asymptotic zero Pe limit is shown for two-dimensional probe since this limit does not exist for a uniform heat generation source.) The high Pe behavior is seen to tend toward the Leveque approximation except with an offset due to the influence of conduction and probe geometry.

This figure also indicates the strong influence of probe geometry and of even modest amounts of substrate conductivity. Departures from simple limiting behavior are seen to be largest at intermediate values of Pe - the condition of many hot-film applications. It also appears that the approach of the probe Nusselt number to the 1/3 power of Peclet number occurs at larger Pe for larger values of K and for smaller b/a

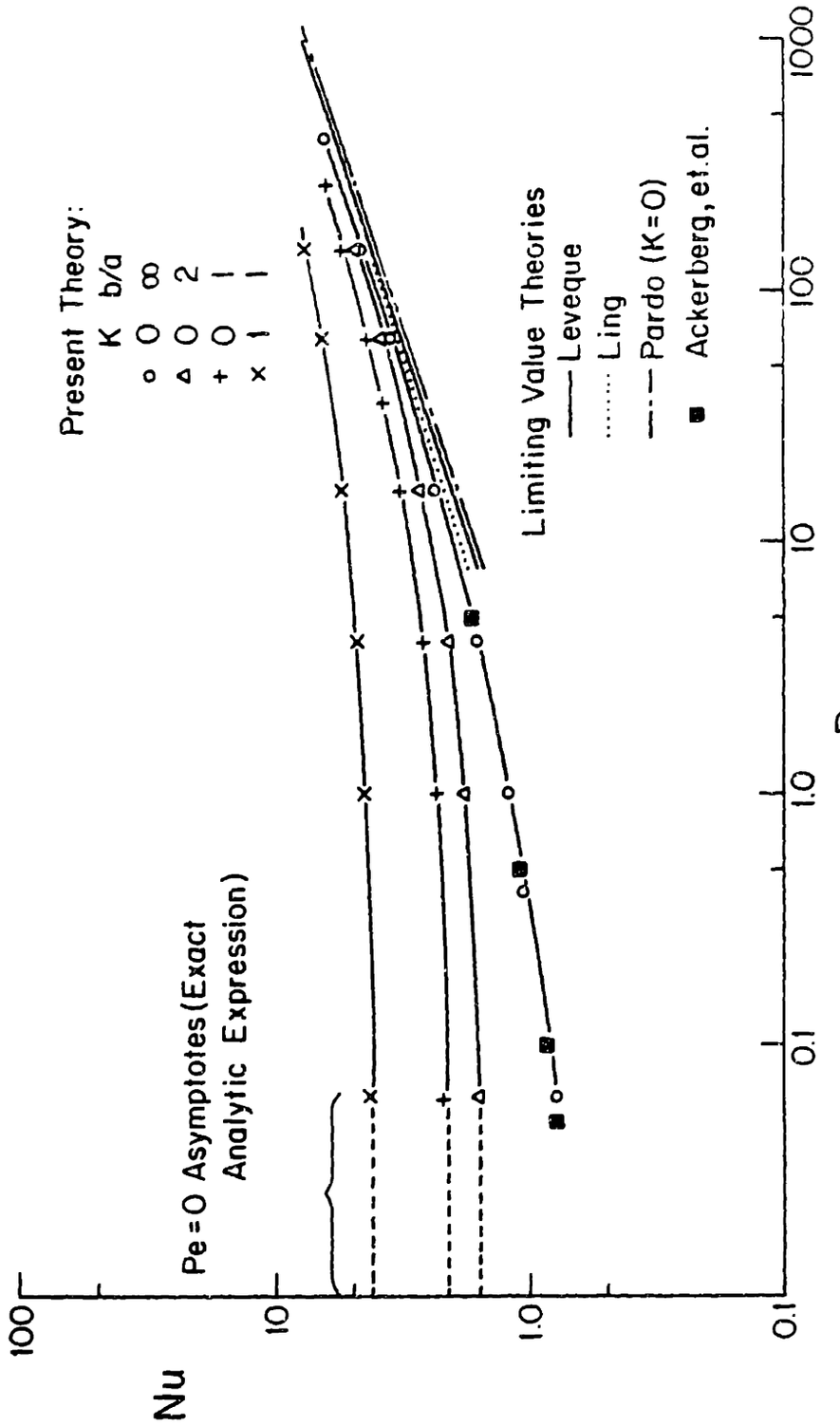

Figure 4.3 Predicted probe Nusselt numbers compared with limiting value theories.

- both contributing to departures from the balance of convection with fluid conduction normal to the surface. However, one must not draw the conclusion that probe sensitivity to flow departs dramatically from the 1/3 power form. At higher values of K much of this behavior is obscured in this log-log plot by the large background offset due to substrate conduction. It is more appropriate to investigate this question by referring to predicted calibration curves (figures 3.12-3.16) and to curves of the "flow-sensitive" portion of the Nusselt number (Section 4.4). Examination of this information shows that substrate conductivity does not play a major role in the approach to the 1/3 power law.

Plotted on this figure are the predictions of the two-dimensional adiabatic wall low Pe theory of Ackerberg, et al. (1978). Our model predictions compare extremely well to those of the two-term matched asymptotic expansion used in this small Pe model.

The predictions of Ling (1963) and Pardo (1980) are also displayed here. It should be noted that while there are many limiting value theories, for similar conditions, the predictions of these theories vary little. Application of any of them to non-limiting value situations can result in large error.

Our theory can be analytically simplified to yield the limiting value behavior exhibited by our predictions. Such simplification is aided by a minor, physically equivalent

reformulation of our expressions. These reductions to limiting value behavior are presented in Appendix F.

4.3 Comparison of Predictions with Experiment

Comparison of our predictions with experiment is difficult due to the paucity of calibration curve data in the literature which can be reduced to Nusselt number - Peclet number form. Often, one or more necessary operating conditions are not reported. Many calibrations are carried out in turbulent flows which may not correspond to the conditions of our model (see Chapter 5). Probes are often mounted such that the resulting substrate configurations consist of a number of different materials to lend support or, more commonly, to thermally isolate the probe and thus decrease the extent of its thermal penetration. (Air gaps have also been used for this purpose.) These configurations complicate the substrate heat transfer process and render the data of questionable use in validating our homogeneous substrate model. We have discovered an unexpected effect of these multiple conductivity substrates that is discussed in Section 4.5.

Despite these difficulties, our predictions are consistent with the data available. The qualitative shapes of the observed curves are well predicted throughout the investigated range. We present in figure 4.4 a comparison of

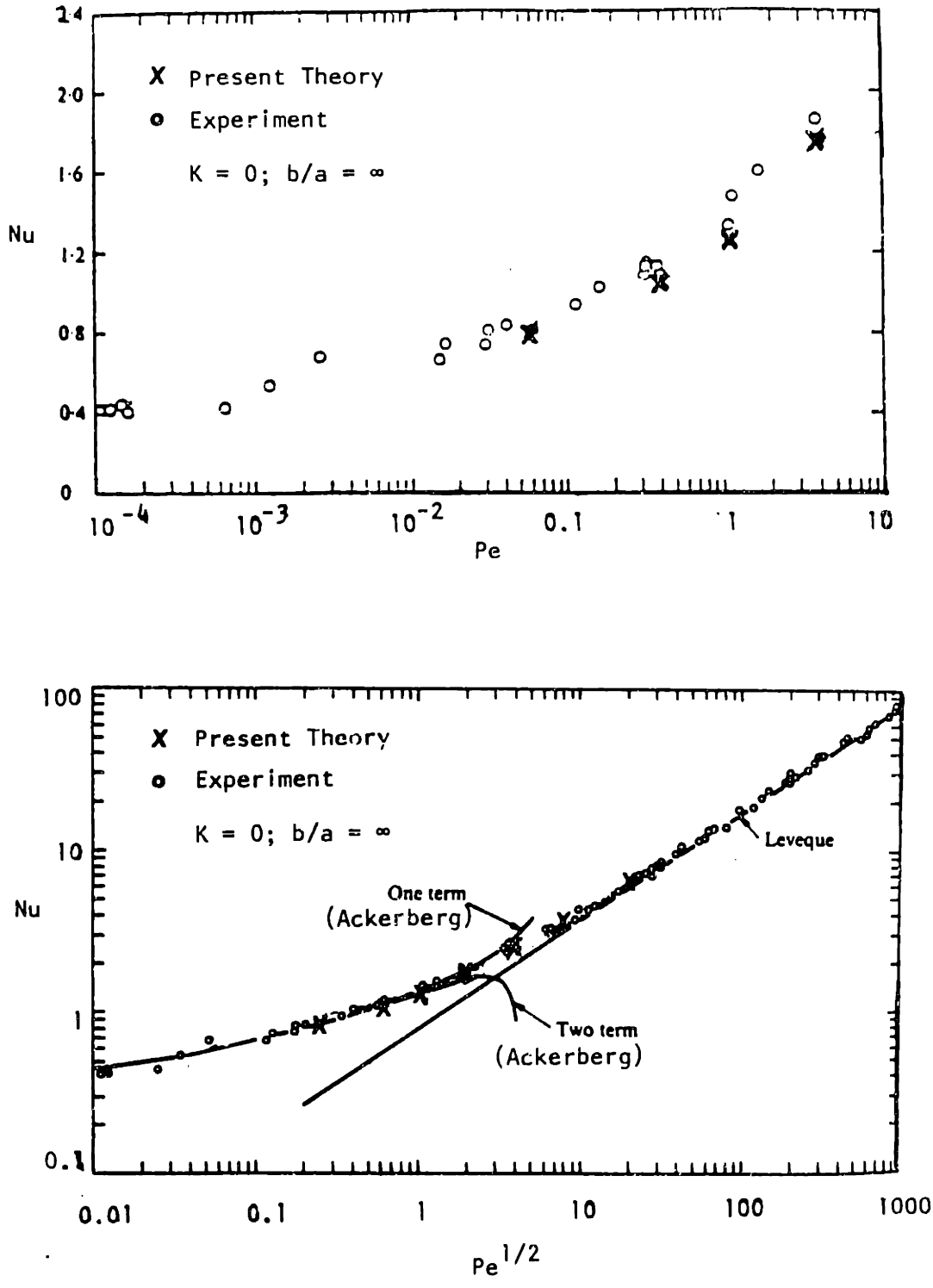

Figure 4.4 Predicted probe Nusselt numbers compared with experiment and limiting value theories (Ackerberg, et. al. 1978).

our two-dimensional adiabatic wall predictions to data taken by Ackerberg, et. al. (1978) with electrochemical probes (for which the conditions of two-dimensionality and K=0 are appropriate). Agreement with this set of data is excellent over several orders of magnitude in Pe. (It should be noted that the other theories presented in this figure only attempt to fit the data over limited ranges of Pe.)

We also compare predictions to some data from Gougat, et al. (1966) for a turbulent air flow. Here, our best guess of the experimental conditions yield K=11 and b/a=5, and we compare total probe Nusselt numbers:

Pe	Model	Experiment
64	16.3	18.6-19.2
144	17.4	20.7-21.2

It can be seen that our predictions are about 15-20% low. Comparison of the flow-sensitive portion of the Nusselt number (see Section 4.4) shows our predictions to be low by about 50%. However, the exact experimental conditions are not adequately known and the flow is turbulent. The need for some carefully controlled and documented experiments is obvious.

4.4 Predictions of the Flow-Sensitive Portion of the Nusselt Number

The useful part of the total probe Nusselt number is that which is flow dependent. This can be obtained by subtracting out the heat transfer present when there is no flow. Experimentally, this quantity can be simply obtained by taking a steady state measurement at zero flow and then subtracting out this portion as a "d.c. offset". Our model considers this offset to be due to conduction in the substrate and fluid. In practice, heat transfer due to natural convection or radiation may also contribute to this zero-flow reading. These effects are discussed in Section 4.7 where it is shown that they are small compared to conduction under most circumstances.

It is useful to see how the flow-sensitive portion of the probe Nusselt number varies with the governing parameters. Tanner's (1967) calculations are primarily for a flow-sensitive Nusselt number. However, the evaluated results are valid only for large K. He does not include streamwise or spanwise fluid conduction, and thus the amount of conduction in the fluid is underestimated. Pardo (1980) implicitly considers the flow-sensitive heat transfer by investigating the partition of heat transfer between the fluid and the substrate, but does not explicitly present a flow-sensitive Nusselt number, nor correct for fluid conduction. He fits a general expression for probe Nusselt number to his numerical predictions:

$$Nu = 0.66\ K + 0.76\ Pe. \qquad (4.6)$$

The second term on the right can be viewed as an approximation to a flow-sensitive Nusselt number that does not depend upon the effects of fluid conduction; the first term on the right is attributable to substrate conduction.

As shown in Chapter 2, the Nusselt number at zero Peclet number is easily obtained. We can write

$$\begin{aligned} Nu(Pe=0,K,b/a) &= (K+1)\ Nu(Pe=0,K=0,b/a) \\ &= (K+1)\ Nu_{00} \end{aligned} \tag{4.7}$$

where the symbol Nu_{00} is introduced as a shorthand notation for Nu(Pe=0,K=0,b/a) and is a function solely of b/a. We define the flow-sensitive portion of the Nusselt number, Nu_{fs}, as the difference between the total probe Nusselt number for a given probe and the Nusselt number of that probe at zero flow:

$$Nu_{fs}(Pe,K,b/a) = Nu(Pe,K,b/a) - Nu(Pe=0,K,b/a). \tag{4.8}$$

Thus, the total probe Nusselt number can be expressed as:

$$\begin{aligned} Nu(Pe,K,b/a) &= Nu(Pe=0,K,b/a) + Nu_{fs}(Pe,K,b/a) \\ &= K\ Nu_{00} + Nu_{00} + Nu_{fs}(Pe,K,b/a). \end{aligned} \tag{4.9}$$

This form is very similar to that of Pardo (4.6). The first term on the right of (4.9) is due to conduction to the

substrate; the balance of the right hand side of - i.e., Nu_{00} + Nu_{fs} represents heat transfer to the fluid and is analogous to the second term on the right of (4.6).

Figures 4.5 and 4.6 present the flow-sensitive Nusselt numbers obtained by application of (4.8) to our predictions. Figure 4.5 displays the variation of the flow-sensitive calibration curves with probe aspect ratio for an adiabatic substrate. (For the two-dimensional probe, a zero Peclet number solution does not exist. Thus, the Nusselt number for K=0 and Pe=0.0625, the lowest value of Pe calculated, was taken as being an "effective" value of Nu_{00} to enable comparison of these calculations with three dimensional cases.) Nu_{fs} is seen to vary smoothly with b/a. The influence of b/a on Nu_{fs} is much smaller than its influence on the total Nusselt number (figure 3.15). The flow-senstitive curves all appear to approach the same slope as Pe increases, the larger aspect ratio probes approaching this asymptote more quickly. The larger aspect ratio probes also produce a larger Nu_{fs} for a given Peclet number. This is in contrast to the total probe Nusselt numbers which are larger at a given Pe for smaller aspect ratios. This is due to the rapid increase in the contribution of conduction as probe aspect ratio decreases. Failure to properly account for aspect ratio can lead to a sizable error in the inferred shear stress. As an example, for a square probe at Pe=64, Nu_{fs} = 2.17. If the Nu_{fs} curve for the two-dimensional probe were used instead of

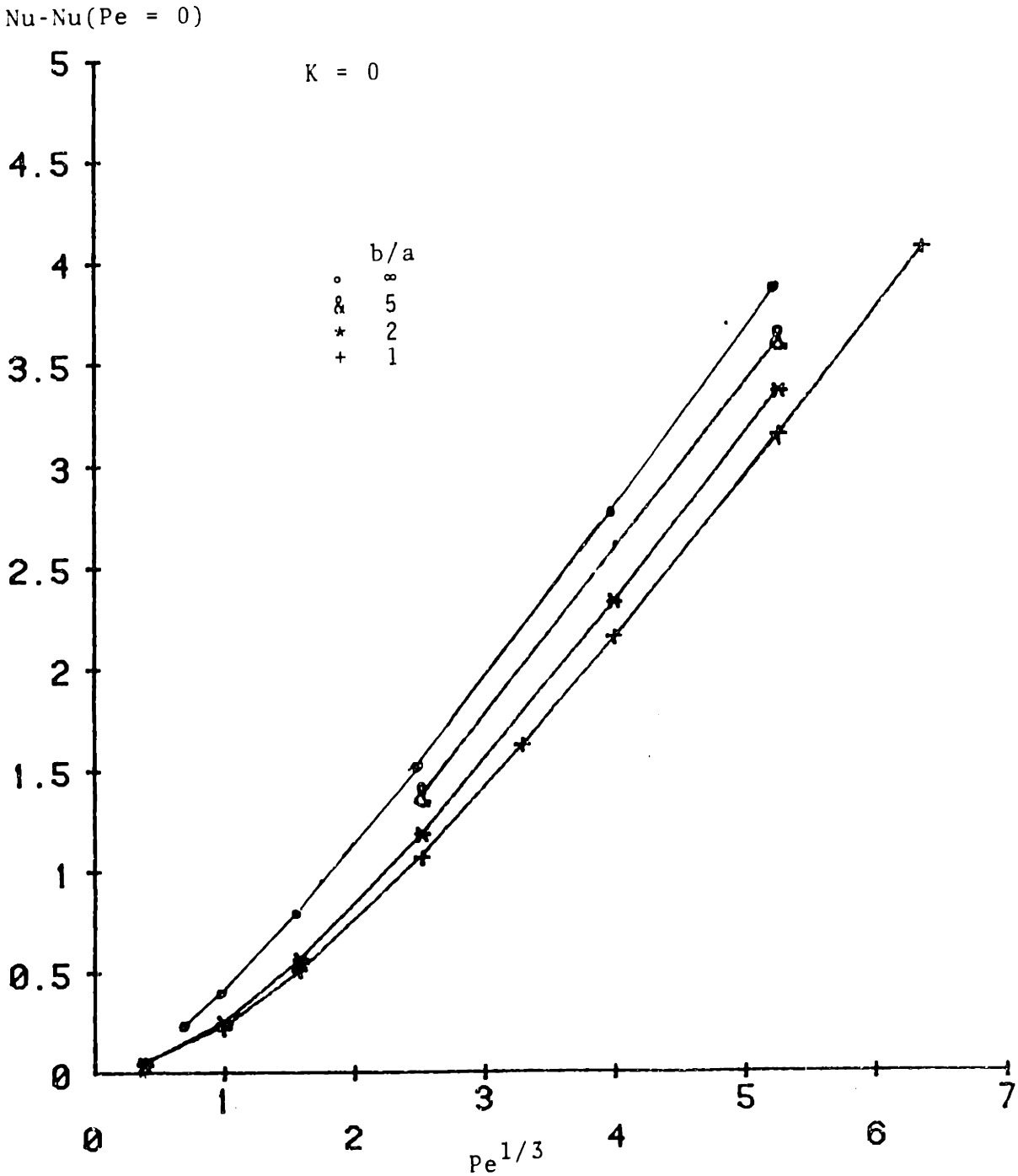

Figure 4.5 Variation with aspect ratio of the flow-sensitive portion of predicted probe calibration curves (K=0).

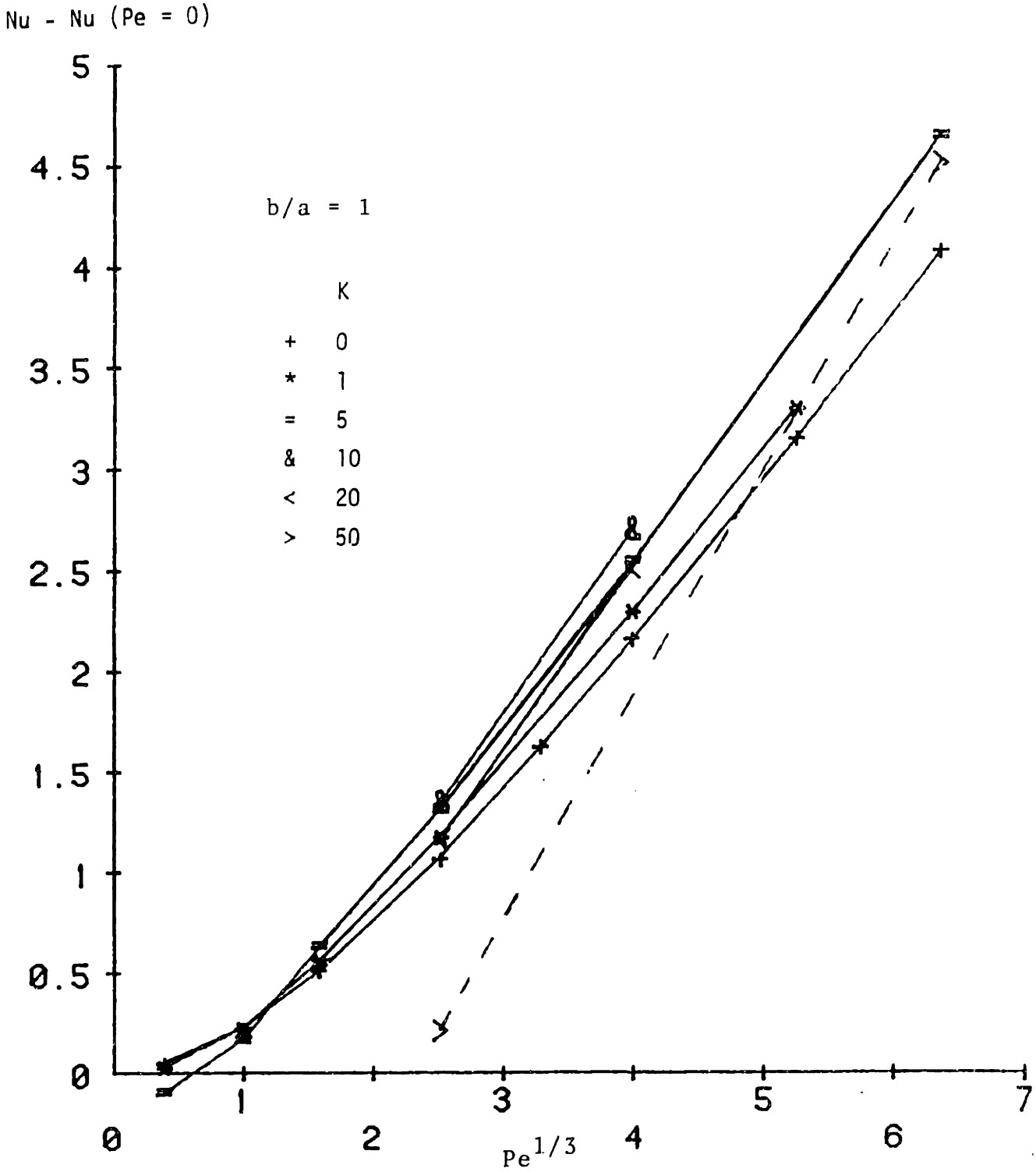

Figure 4.6 Variation of with conductivity ratio of the flow-sensitive portion of predicted probe calibration curves (b/a=1).

that for the square probe, this Nusselt number would be translated to a value of Pe=35. Thus the inferred shear stress would be low by a factor of nearly two.

Figure 4.6 presents the predicted variation of the flow-sensitive Nusselt number of square probes for conductivity ratios varying from 0 to 50. There is surprisingly little variation in these curves over this very large range of substrate conductivity. No general trends can be concluded, aside from the relative insensitivity of Nu_{fs} to substrate conductivity. It would appear that Nu_{fs} increases weakly with increasing K until K reaches a value between 10 and 20 and then decreases somewhat. However, the numerical uncertainty (1% of total probe Nusselt number) in the present calculations lead to an increasing uncertainty in Nu_{fs} as K increases. This uncertainty does not allow definitive determination of minor trends at large values of K. The slope of these curves also appears to increase with K. The somewhat anomalous behavior of the two calculated points for K=50 is most likely due to numerical error. The slightly negative value of Nu_{fs}(Pe=0.0625,K=5) is also attributable to the comparatively large amount of computation needed to resolve small differences in Nu for modest to large K at low Pe and b/a. It was not deemed worthwhile to better resolve these cases.

A complete listing of all predicted flow-sensitive Nusselt numbers is presented in Appendix E.

The relative insensitivity of the flow-sensitive Nusselt number to substrate conductivity variations indicates that the coupling between the conductive and convective modes of heat transfer or between the fluid and the substrate is weak. This suggests writing an expression to approximate the predicted total probe Nusselt number as:

$$Nu(Pe,K,b/a) = (K+1)\ Nu_{00} + \tilde{Nu}_{fs}(Pe,b/a) \qquad (4.10)$$

where $\tilde{Nu}_{fs}(Pe,b/a)$ is a best fit value of $Nu_{fs}(Pe,K,b/a)$ averaged over K and is expressed as a function solely of Peclet number and aspect ratio. If this value of Nu_{fs} is selected to be that at K=0, (4.10) can be rearranged and expressed as:

$$\begin{aligned} Nu(Pe,K,b/a) &= K\ Nu_{00} + Nu_{00} + \tilde{Nu}_{fs}(Pe,b/a) \\ &= K\ Nu_{00} + Nu(Pe,K=0,b/a). \end{aligned} \qquad (4.11)$$

Thus, the total probe Nusselt number is approximated as the sum of the Nusselt numbers for pure conduction to the substrate (bounded by a non-conducting fluid) and for flow over an adiabatic wall. The substrate conduction portion is available in analytic form, and the adiabatic wall flow requires relatively little computation.

Values of total probe Nusselt number calculated using this approximate decoupled expression (4.11) for 31 cases are

presented in Appendix E. The calculated values are seen to be within 4% or less of the results of the more detailed calculations. The prediction of flow-sensitive Nusselt numbers will, in general, not be this good. The adiabatic wall flow-sensitive Nusselt number is not the best expression to choose for Nu_{fs} for all K. Inspection of figure 4.6 shows that the flow-sensitive Nusselt number for K = 0 is lower than that of most other values of K. (Approximation (4.11) almost always under predicts the total probe Nusselt number - Appendix E.) Approximation (4.10) can be improved by selection of a different value of $\tilde{Nu}_{fs}$ such as a value for a K > 0 or an empirical best fit to the predictions. This would increase the accuracy of the predictions of total Nusselt number to better than 2% and significantly increase the accuracy of the decoupled flow-sensitive predictions.

As discussed previously, the lack of an expression for Nu_{00} for a two-dimensional geometry precludes application of (4.10) to two-dimensional probes. However, inspection of figure 3.19 suggests that a similar decomposition is possible over several ranges of K. This is seen to be the basis of Pardo's expression (4.6) for the Peclet numbers between 25 and 100.

The validity of this approximation does not rest solely on empiricism, but is qualitatively justified by an examination of the expressions for temperature distribution and Nusselt number in wavenumber space (Appppendix C). Such

an investigation suggests that this type of decoupling may also prove to be a good approximation for non-rectangular probes and other heat source distributions.

4.5 Effect of Streamwise Variation in Substrate Conductivity

In this Section we examine the effects of spatial variation of substrate conductivity such as commonly arises in practice due to the presence of materials of different thermal conductivity in the vicinity of the heated film. A simple analysis is presented which demonstrates that spatial variation of substrate conductivity can influence probe calibration curve slopes. This phenomenon is found to be capable of explaining the slopes of experimentally obtained calibration curves.

Most conventional probes consist of a metal film deposited on a substrate (typically quartz) of lateral dimensions comparable to those of the film. This assembly is mounted in the wall on which the shear stress measurements are desired. The wall is generally of a different material and thus has a different - often significantly different - thermal conductivity. (For example, in research applications, the wall is often made of plexiglass which has a thermal conductivity of about 0.1 that of the typically quartz substrate.) There are thus two different conductivity ratios to consider: one based on the conductivity of the substrate

material in contact with the heated film and the other based on the surrounding material. This surrounding material will affect the heat transfer from the probe because the region of thermal penetration extends for several probe lengths in all directions (Chapter 3).

Flow-Sensitive Conductivity Ratio

Our investigations of the wall heat flux (Chapter 3) show that virtually all the heat transfer from the probe to the fluid occurs upstream of or laterally adjacent to the probe, with the upstream component being generally larger than the laterally adjacent portion. This is consistent with the numerical study of Pardo (1980) and the experimental measurements of Pope (1971). Pope's measurements indicate that the heat flux is from the fluid to the substrate downstream of the probe and that its magnitude is much less than that upstream. Pardo predicts regions of transfer between the substrate and the fluid in both directions downstream of the probe. The majority of our predictions show downstream transfer to be into the substrate. However, although the direction of the predicted downstream heat transfer may vary, the various studies agree that its magnitude is much less than that of the upstream transfer. Thus, it should be necessary to look only in the upstream direction to obtain a rough estimate of the effect of

conductivity variation on probe performance.

The distance upstream over which this heat transfer occurs is flow dependent. As the shear stress - and thus the Peclet number - increases, this region is located closer to the probe; and the conductivity of the substrate material nearer the probe becomes more important relative to that of the surrounding material. In simplistic terms, one can think of this "multiple-conductivity substrate" as possessing an average or "effective conductivity" that depends upon the spatial arrangement and conductivities of the various materials in the vicinity of the heated film. Because the region of the substrate that influences probe performance is flow dependent, the "effective conductivity" must also depend on the flow and, thus, the Peclet number.

A qualitative investigation of this effect begins with the factors determining the upstream thermal penetration of the probe. A simple one-dimensional analysis balancing upstream fluid and substrate conduction with convection in the downstream direction (Appendix D) reveals that the upstream temperature field decays with distance from the probe with a characteristic length L_T^* and that the scaling of L_T^* is given by:

$$L_T^*/L_p^* \sim (K+1)/Pe^{1/2} \qquad (4.12)$$

where L_p^* is the streamwise length of the probe. For a

three-dimensional probe, aspect ratio comes into play. From the expressions for pure conduction in a stagnant fluid (Chapter 2) it is known that the temperature field shape is not dependent on K. Thus, at large values of $(K+1)/Pe^{1/2}$, L_T^*/L_p^* should asymptote to a constant value that depends only upon aspect ratio.

Predicted temperature distributions were examined to test this scaling law. L_T^* was arbitrarily selected as the distance upstream of the probe center (x=0) at which the computed wall temperature distribution along the line z=0 had decayed to 10% of the mean probe temperature. This was deemed to be a reasonable measure of upstream thermal penetration. Figure 4.7 presents this thermal penetration length for aspect ratios of 1, 5, and infinity, values of K between 0 and 50, and Peclet numbers from 0.0625 to 256. The agreement with the proposed scaling relation (4.12) is very good. The typical values of L_T^* are seen to be of the order of several probe lengths - a distance comparable to the typical distance from the hot-film of the change in substrate materials.

The effect on L_T^* of a step change in substrate conductivity can be expressed by performing a balance similar to that used to obtain (4.12). This derivation is performed in Appendix D and suggests the use of an average or "effective conductivity ratio", K_{eff}, which is defined to be:

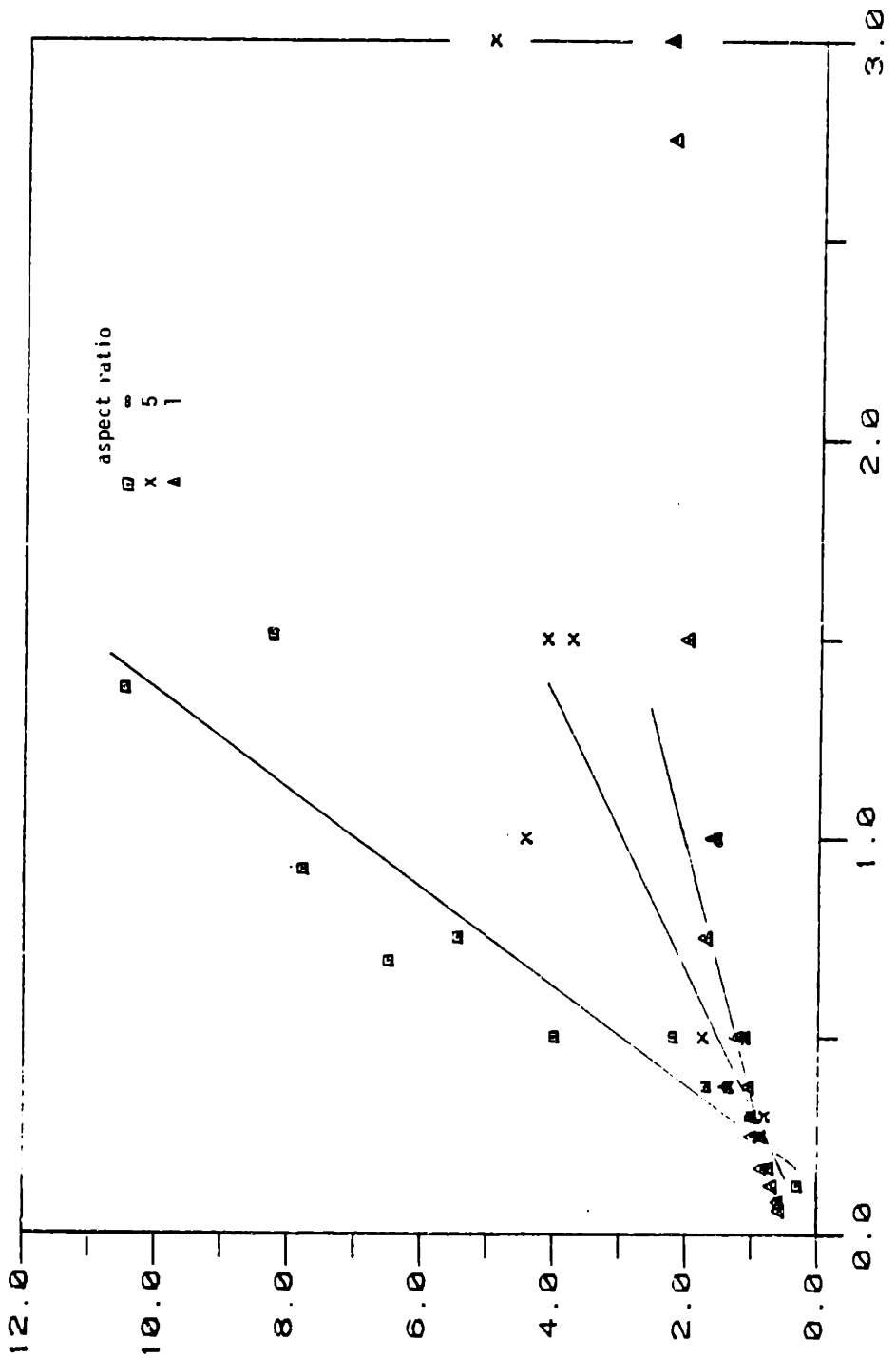

Figure 4.7 Scaling of the predicted upstream thermal penetration lengths. (Solid lines indicate regions of approximately linear behavior.)

$$K_{eff} \equiv \frac{L^*_T}{\frac{L^*_b}{K_i} + \frac{L^*_T - L^*_b}{K_o}} \quad . \tag{4.13}$$

Here, K_i is the conductivity ratio formed from the thermal conductivity of the "inner" substrate material near the probe, K_o is the conductivity ratio formed from the conductivity of the "outer" substrate material located upstream of the "inner" material, and L^*_b is the distance upstream of the probe that the step change between K_i and K_o occurs. This average is based on the relative contributions of the two substrate materials to the overall resistance to heat transfer from the probe (Appendix D). The Pe dependence of K_{eff} is implicit in the dependence of (4.13) on the upstream thermal penetration length L^*_T. The Pe dependence of K_{eff} can be explicitly examined by solving (4.12) for L^*_T using K_{eff} as K in (4.12) and making the approximation that $K_{eff+1} \quad K_{eff}$. When the resulting expression for L^*_T is substituted into (4.13) we obtain:

$$K_{eff} \sim K_o + \frac{L^*_b}{L^*_p} \sqrt{Pe} \left(\frac{K_i - K_o}{K_i} \right) . \tag{4.14}$$

This average conductivity ratio, K_{eff}, is dependent not only on the values of K due to each substrate material (K_i and K_o) and their location (L^*_b), but also on the Peclet number.

The effect on the relationship between Peclet number and probe Nusselt number in the presence of such a flow-sensitive

conductivity ratio can be qualitatively examined with the aid of (4.9) which expresses the predicted probe Nusselt numbers for a homogeneous substrate as the sum of a flow-sensitive portion and a background portion due to conduction heat transfer:

$$Nu(Pe,K,b/a) = (K+1)\ Nu_{00} + Nu_{fs}(Pe,K,b/a). \qquad (4.9)$$

If expression (4.14) for K_{eff} is used as K in (4.9), the result is:

$$Nu \sim (K_o + 1)Nu_{oo} + \frac{L^*_b}{L^*_p}\sqrt{Pe}\left(\frac{K_i - K_o}{K_i}\right) + Nu_{fs}. \qquad (4.15)$$

The second term of (4.15) introduces an added Pe dependence of the Nusselt number, thus leading to an increase in the slope of Nu-Pe calibration curves above that of Nu_{fs} associated with a homogeneous substrate. (The analysis presented here and in Appendix D is qualitative. Its purpose is to demonstrate that spatial variation of substrate conductivity influences the slope of the Nu-Pe probe calibration curve. The dependence on the half power of Pe in (4.12) and (4.14) is based on two-dimensional order of magnitude arguments (Appendix D). A more detailed analysis might have a somewhat different Pe dependence. However, this would not affect our basic conclusion of the effect of spatial variation of substrate conductivity.)

Consistency With Experimental Data

A major disagreement between previous theories and measurement is a large difference in the Nu-Pe calibration curve slopes. This disagreement has been almost universally attributed to the effects of simple substrate conduction. It has become common practice to introduce an effective streamwise probe length L^*_{eff} defined to be the probe length that would make the theoretical and experimental calibration curve slopes agree (Brown 1967, Pope 1971, etc.). The argument begins by saying that, for large enough Pe, probe calibration curves can be represented by a straight line (see figure 1.2),

$$Nu = A + B\ Pe^{1/3},$$

where the theoretical value for B is about 0.8 (Leveque 1928, Ling 1963, Pardo 1980, etc.). Experimental values of B are, however, usually a factor of several larger. Thus one can redefine the Peclet number to be based on an "effective length" of the probe that is larger than L^*_p:

$$Nu = A + B\ (s\ L^{*2}_{eff}\ /\alpha)^{1/3}$$

$$Nu = A + B\ (L^*_{eff}/L^*_p)^{2/3}\ Pe^{1/3}\ .$$

Thus

$$L^*_{eff} = L^*_p \, (B_m/B_t)^{1.5} \qquad (4.16)$$

where B_m and B_t are the measured and theoretical values of B, respectively. (The Leveque value 0.807 is usually chosen for B_t.) L^*_{eff} is typically a factor of 2-5 or more larger than the actual probe length. This enlarged probe length has been attributed to the increased area of heat transfer to the fluid due to substrate conduction.

Our work, however, includes the effects of three-dimensional homogeneous substrate conduction. Our predicted values of B can be found by reference to figures 3.13, 3.14, and 4.6. There is, in general, an increase in B over adiabatic wall theory, but not as large as that observed experimentally. For K less than or equal to 11, B is usually one or less. The predicted value of B does increase with K, however. For K = 50, we predict B to be approximately 1.1 and 1.9 for square and two-dimensional probes. (These represent values of L^*_{eff} of 1.15 and 2.6, respectively, using B_t = 0.807). Because of the large background component of heat transfer by conduction, the flow-sensitive portion of our predicted Nusselt numbers at large K are subject to a greater uncertainty (1% of the total Nusselt number) than at smaller K. Thus, these large K calculations should be refined for a

more quantitative comparison.

However, our low K predictions can be used with much more confidence. Measurements in water, for which values of K are much less than for air, also produce values of B larger than predicted by our theory or by previous theories. Pope (1971) finds B_m to be about 1.6 - operating at a conductivity ratio of about 1.7 (pyrex/water). This is significantly larger than our predictions for low K. The concept of a flow-sensitive "effective conductivity ratio" offers one explanation for these large observed values of B.

Additional support for the contention that homogeneous substrate conduction is not the sole mechanism producing the observed sensitivities to shear is provided by Tanner (1967) who dealt with rectangular probes having a uniform heat generation rate distribution. Our theory should be in agreement with Tanner's when both K and Pe are large. Tanner presents some predictions of probe Nusselt number as a function of a parameter proportional to $K/Pe^{1/3}$ which asymptote to fixed multiples of Leveque's predictions at large values of $K/Pe^{1/3}$ (figures 3 and 4 in Tanner's paper). The maximum calibration curve slope based on these predictions for b/a between 1 and 20 is between 1.5 and 1.9 times that of Leveque - or B = 1.2-1.7 approximately. Even these maximum values are lower than often observed.

The analysis of this Section is presented to provide a qualitative mechanistic explanation of the disagreement

between predicted and measured calibration curve slopes and to investigate the effects of commonly used experimental probe configurations that result in nonhomogeneous substrates. We do not wish to imply that this method can predict the calibration curves of probes in which more than one value of substrate conductivity is important. This analysis does suggest, however, that spatial variation of substrate conductivity can be used as a design option to elicit a desired shear sensitivity. This is a finding of potentially major import. One can conceive of using various conductivity gradations to enhance or inhibit the probe sensitivity to shear - perhaps differing with flow direction. A more elaborate examination of this phenomenon would, however, need to be performed to obtain any quantitatively accurate predictions.

To illustrate consistency with experiment, we present figure 4.8 where sections of a family of curves based on the predicted Nu-Pe behavior parametric in K for a probe of b/a=3 mounted on a homogeneous substrate are shown. These curves have been generated by interpolation between our predictions and by use of expression (4.11) where Nu_{00} is exactly computed for this b/a. Each curve of this family has the same slope for a given value of Pe, but differs in intercept. Superimposed on this curve family is an experimentally obtained calibration curve (Brown 1967) whose slope differs significantly from the predicted slopes. The intersections of

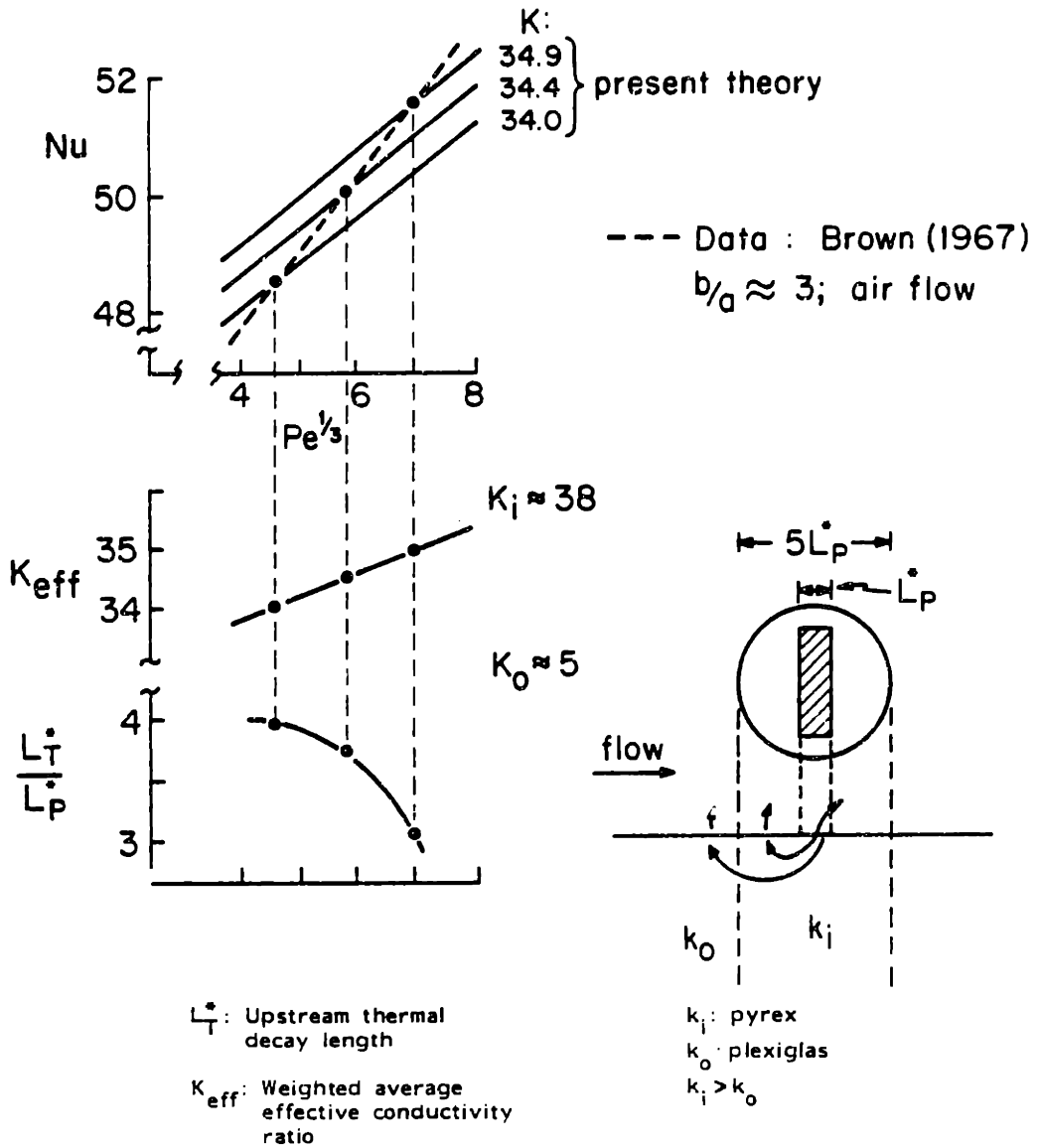

Figure 4.8 Illustration of the creation of a Peclet number dependent average conductivity ratio due to spatial variation of the substrate thermal conductivity.

the experimental and predicted calibration curves can be viewed as a series of probe operating points. The "effective conductivity" ratio at each operating point is the conductivity ratio of the predicted curve that intersects the experimental curve. Thus, in figure 4.8 the effective conductivity ratio varies from 34 to 34.9 over the Pe range of 95 to 330. This variation in "effective conductivity ratio" is bounded by the conductivity ratios for the two component substrate materials: pyrex/air (K=5) and plexiglas/air (K=38).

As a final step in this process, we investigate the inferrred behavior of L_T^* obtained by interpolation in figure 4.7 setting $K = K_{eff}$. The magnitudes of L_T^* inferred (also presented in figure 4.8) are seen to be comparable to the distance of the two-conductivity boundary to the hot-film. This distance, of course, varies spatially due to the circular nature of the boundary and the rectangular shape of the film. L_T^* is seen to move closer to the probe with incresing Pe, thus changing the relative influences of the two substrate materials.

4.6 Probe Thermal Condition

Our model treats the film sensing element as infinitesimally thin and possessing negligible internal heat conduction. The calculations presented consider a uniform distribution of heat generation although other distributions

can be incorporated into the model in a straightforward manner (see Chapter 2). Departures from this condition could be caused by conduction within the film (in any of the three directions), variation in the generation rate due to nonuniform film resistivity caused by the nonuniform temperature distribution of the probe, and nonuniformities in the film itself. In this Section, criteria are presented to estimate the effects of the first two of these factors. It is shown that, for typical current probe designs and for most realistic possible designs, these two effects are usually negligible. Nonuniformities in the material of the film itself is a manufacturing problenm and is not discussed here.

Conduction within the Probe

In the calculation of surface heat transfer coefficients, it is common to consider two simplified surface boundary conditions - uniform temperature and uniform heat flux. Such simplified conditions make analysis easier and, at worst, provide a guide to the behavior for more complicated conditions. In a like manner it has been common to assume one of these conditions for heat transfer from the probe. (A summary of probe conditions adopted by other authors is contained in table 1.1.) The real condition is a heat generation condition as assumed in our work and by Tanner (1967) and Davies and Kimber (1972). A uniform generation

rate reduces to a uniform flux to the fluid for the case of an adiabatic substrate. Pure conduction to a stagnant fluid and a conducting substrate results in a uniform flux to both the fluid and the substrate. A very large value of K will also produce a relatively uniform flux to both media. There has been some discussion as to which of these conditions is most realistic for modeling of hot-films. We demonstrate here that the uniform generation condition not only is based on the actual physics, but is much more general and can produce flux and temperature distributions of varying degrees of uniformity depending on the conditions to which the film is subjected. (The probe condition approaches uniform temperature, for example, for large values of K.)

Consider the two-dimensional edge view of a hot-film in figure 4.9. The film is modeled as composed of a homogeneous material of thermal conductivity k_p, streamwise length L_p^*, thickness t^*, and uniform volumetric heat generation rate W^*. Heat is lost by the probe by transfer to both the fluid and the substrate. We define H_x to be a total local heat transfer coefficient representing the combined local effects of transfer to both the fluid and the substrate:

$$Q_f(x^*) + Q_s(x^*) = H_x (T_p^* - T_\infty^*) .$$

To estimate the temperature gradient across the probe thickness, we calculate a Biot number that measures the ratio

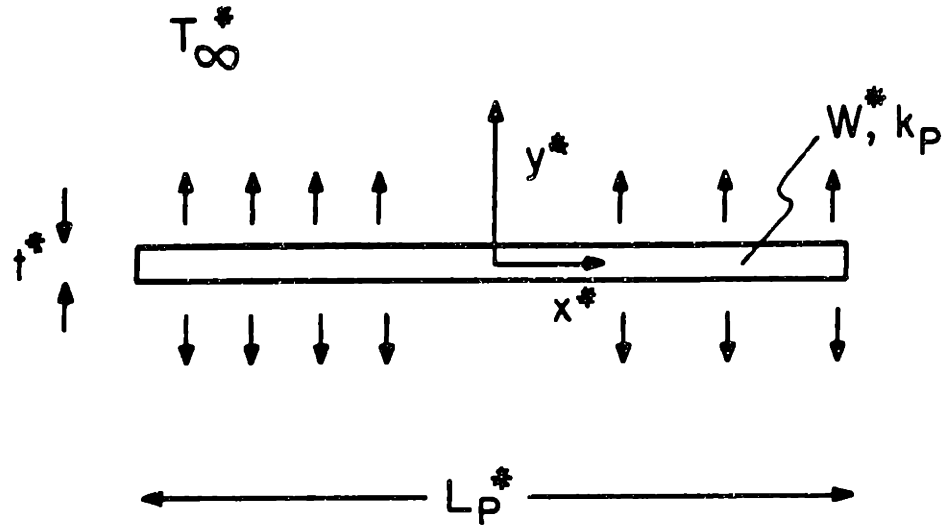

H_x : Total local external heat transfer coefficient

Figure 4.9 Probe modeled as a fin with internal heat generation.

of transfer from the surface to conduction in the y direction:

$$Bi = \frac{H_x t^*}{k_p} .$$

The average value of the total probe heat transfer coefficient, denoted by $\bar{H}$ can be obtained from calculated values of probe Nusselt numbers for total heat transfer:

$$Nu = \frac{\bar{H} L_p^*}{k_f}$$

$$\bar{H} = \frac{Nu\, k_f}{L_p^*}$$

$$Bi = Nu \frac{k_f}{k_p} \frac{t^*}{L_p^*} .$$

Approximate values for these quantities are:

$L_p^* \sim 0.01 - 0.1$ cm

$t^* \sim 0.00001$ cm

$k_f \sim 0.2 - 16 \ \frac{mw}{cm^{2o}C}$

$k_p \sim 700 - 900 \ \frac{mw}{cm^{2o}C}$

$Nu \sim 2 - 100$.

Thus, $Bi \gtrsim 2 \times 10^3 - 4 \times 10^8$, and temperature gradients in y are therefore completely negligible. Similar arguments apply if the streamwise probe length is replaced by the spanwise dimension.

The magnitude of conduction within the probe in the streamwise and spanwise directions can be estimated from a "fin" type analysis. Referring again to figure 4.9, we can modify the standard fin equation (Rohsenow and Choi, 1961, p.107) to include the internal heat source W* and obtain:

$$k_p t^* \frac{d^2 T_p^*}{dx^{*2}} - H_x (T_p^* - T_\infty^*) + W^* t^* = 0 . \qquad (4.17)$$

The heat generated in the probe per unit area, $W^* t^*$, is balanced by internal conduction (the first term) arising from nonuniformities in the probe temperature and by heat transfer away from the probe governed by external local conditions (the second term). Let

$$\theta \equiv \frac{T_p^* - T_\infty^*}{\bar{T}_p^* - T_\infty^*}$$

where $\bar{T}_p^*$ is the average probe temperature. Then (4.17) can be written:

$$\frac{d^2 \theta}{d\left(\frac{x^*}{L_p^*}\right)^2} - H_x \frac{L_p^{*2}}{k_p t^*} \theta + \frac{W^* L_p^{*2}}{k_p (\bar{T}_p^* - T_\infty^*)} = 0 . \qquad (4.18)$$

We can estimate the relative sizes of the first two terms of (4.18) by taking their ratio. The order of magnitude of both θ and of the first term is one. Thus the ratio of the second to first terms is:

$$H_x \frac{L_p^{*2}}{k_p t^*} . \qquad (4.19)$$

If this expression is much larger than one, the first term can be neglected and (4.18) becomes:

$$\frac{H_x}{t^*} \theta = - \frac{W^*}{\bar{T}_p^* - T_\infty^*}$$

or,

$$T_p^* - T_\infty^* = \frac{W^* t^*}{H_x} . \qquad (4.20)$$

The probe temperature distribution is then determined solely by local external conditions (given here by H_x) and by the local internal generation rate - which is the assumption of our model. It should be noted that although H_x is a local quantity, it is influenced by the global environment.

We can evaluate expression (4.19) by referring to the above mentioned probe dimensions and the thermal conductivity values given above and in table 4.1. Thus:

$$L_p^* / t^* \sim 10^3 - 10^4$$

$$k_f/k_p \sim 4 \cdot 10^4 \text{ for air,}$$

$$\sim 7 \cdot 10^{-3} \text{ for water.}$$

Our calculations show that H_x is of the same order as $\bar{H}$, the

value of H_x averaged over the probe. Thus we can take $\bar{H}$ as an estimate for H_x, and (4.19) is of the order

$$\frac{\bar{H}\, L_p^*}{k_f} \cdot \frac{k_f}{k_p} \cdot \frac{L_p^*}{t^*}$$

$$= Nu \cdot \frac{k_f}{k_p} \cdot \frac{L_p^*}{t^*} .$$

For a quartz substrate our calculations show that

Nu 100, for air, and

20, for water.

We then can estimate:

$$Nu \frac{k_f}{k_p} \cdot \frac{L_p^*}{t^*} \sim 40 - 400 \text{ for air, and}$$

$$\sim 140 - 1400 \text{ for water.}$$

Thus, conduction within the probe is negligible and the amount of heat conducted within the probe is of the order of 0.07-2.5% of that generated. These estimates will, of course, vary for other materials. However, most probes in use have a quartz or glass substrate, and the thermal conductivity of these materials is typical of the range of conductivities of many other materials that might be used including most ceramics. Most plastic materials have a conductivity about a factor of ten lower (e.g., plexiglass). The use of such a material will lead to a value of Nu_x about 0.1 of those above and the value of (4.19) will also be of the order of 0.1 of those above. These estimates suggest that conduction within

the probe may be of some significance for the smallest probe length to thickness ratios. (The use of plastics as substrate materials presents certain manufacturing difficulties not discussed here.)

In the absence of internal conduction, the probe temperature distribution will be as uniform or nonuniform as the heat generation rate and the external transfer conditions. The calculated probe temperature actually becomes much more uniform as K increases. For example, for Pe=16 and b/a=1, the peak probe temperature is 27% above the mean for K=0, and 15% above the mean for K=50.

Effect of Temperature Dependent Resistivity

The assumption of a uniform volumetric heat generation rate depends upon a homogeneous film material with a uniform power dissipation which, in turn, requires a uniform current density and resistivity. However, resistivity is temperature dependent. Indeed, this temperature sensitivity is central to the operation of a hot-film probe. A spatially varying probe temperature may produce a spatially varying resistivity and a concomitant spatially varying power dissipation. However, as we show in this Section, the nonuniformities in power dissipation resulting from this resistivity variation are not large for typical probe conditions. The effect on calculated probe Nusselt number should be even less due to the averaging

process: a higher temperature results in a larger resistivity and a lower power dissipation which in turn means less heat needs to be transferred away locally, and thus the local probe temperature will be lowered. The effect of such resistivity variations is to raise the probe temperature when it is below the mean and to lower it when it is above the mean.

To estimate this effect, consider the expression for the resistivity of the film:

$$\rho/\rho_0 = 1 + \alpha\left(T^* - T_0^*\right) \tag{4.21}$$

where ρ is the resistivity at temperature T^*, ρ_0 is the resistivity at a reference temperature T_0^*, and α is the temperature coefficient of resistivity. By integrating this quantity over the probe, a total resistance can be found and, utilizing the voltage drop across the film, one can relate the local and average dissipation rates. Expressing this as source density we write:

$$\frac{Q^*(x,z)}{\bar{Q}^*} = \frac{\bar{\rho}}{\rho(x,z)} = \frac{1 + \alpha(\bar{T}_p^* - T_0^*)}{1 + \alpha(T_p^*(x,z) - T_0^*)} . \tag{4.22}$$

Here, $\bar{Q}^*$ is the average heat dissipation per unit area (total power divided by probe area).

For typical heated-film materials, α = 0.001 - 0.006 / °C. From our calculations, we find that for the large values of K

typical of air flows, the local probe temperature deviates from the mean by less than 20%. For the lower conductivity ratios associated with water flows, the deviation is less than 30%. Using typical probe operating temperatures, we estimate in table 4.4 the deviation of the local power dissipation from its mean value to be less than 13% for air and less than 7% for water flows for the higher value of α. For the lower value of α, these limits are 4% and 1% respectively. These represent maximum local deviations; the mean of the absolute value of the local deviations would be about half of these maximum values. The change in the average probe temperature and thus the Nusselt number is also smaller due to the averaging effect.

4.7 Other Modes of Heat Transfer

Two modes of heat transfer not accounted for by our analysis may play a part in probe performance - natural convection and radiation. We demonstrate in this Section that radiation is unimportant for typical probe operating conditions and that natural convection is usually negligible, but can have a modest effect at low Peclet number under some conditions. To compare the magnitudes of the various modes of heat transfer, we estimate a dimensionless heat transfer coefficient for each mode. This coefficient has the same form as the Nusselt number and is therefore denoted as an

	air	water
$T_p^* - T_o^*$ (°C)	225	45
$\frac{T_p^* - T_o^*}{\bar{T}_p^* - T_o^*}$	0.8 - 1.2	0.7 - 1.3
$Q^*/\bar{Q}^*$ (α = 0.006/°C)	1.13 - 0.90	1.07 - 0.94
$Q/\bar{Q}^*$ (α = 0.001/°C)	1.04 - 0.97	1.01 - 0.99

Note: Reference temperature T_o^* taken to be 20°C

Table 4.4 Estimate of the influence of temperature dependent resistivity on probe power distribution.

"effective Nusselt number" for that mode. Thus, if h_i is the heat transfer coefficient of mode i, we define the effective Nusselt number of that mode to be:

$$Nu_i = \frac{h_i L_p^*}{k_f}$$

where L_p^* is the streamwise probe length.

Radiation

The heated film at an average temperature $\bar{T}_p^*$ radiates heat to its environment at temperature T_∞^*. An estimate of the magnitude of this radiation can be made from:

$$Q^* = \sigma \varepsilon \, (\bar{T}_p^{*4} - T_\infty^{*4})$$

where, $\sigma = 5.67.10^{-9} \frac{mw}{cm^2 {}^\circ K^4}$

ε = emissivity of probe surface

Q^* = radiative flux $\left(\frac{mw}{cm^2}\right)$

Take ε=1 as an upper bound and define the heat transfer coefficient due to radiation, h_{rad} as

$$h_{rad} = Q^* (\bar{T}_p^* - T_\infty^*)$$

$$= \sigma \frac{\bar{T}_p^{*4} - T_\infty^*}{\bar{T}_p^* - T_\infty^*} .$$

Taking L_p^*=0.02cm, a nominal conservative value, and T*=20 °C,

we evaluate the magnitude of radiative transfer (here, $\bar{T}_p^*$ is selected as typical of that used for the given fluid and k_f is evaluated at the the "film" temperature - the average of the $\bar{T}_p^*$ and T^*):

fluid	air	water
$\bar{T}_p^*$ (°C)	250	65
h_{rad} $\frac{mw}{cm^2 °C}$	1.7	0.72
k_f $\frac{mw}{cm°C}$	0.32	6.3
Nu_{rad}	0.1	0.002

These values are very small compared to the computed probe total Nusselt numbers. At low air flow rates, radiation may be of some concern relative to the flow sensitive portion of the probe Nusselt number, but the value of the conductive component is very large (of the order of 20 - 100 for a quartz substrate), and the radiative component may be subtracted out with the zero-flow component.

Natural Convection

The effect of natural convection will be greatest at low flow rates, and its fraction of the total heat transfer will be largest for zero flow. The magnitude of this mode of heat

transfer, unlike other modes, depends upon the probe orientation relative to any body force vectors - e.g., gravity, centrifugal forces, etc. We consider the most common such force, gravity, here. Of three selected orientations, natural convection will be largest when the probe is mounted vertically - i.e., parallel to the gravity vector, next largest when mounted horizontally facing upwards, and least when mounted horizontally facing downwards. (The magnitude for other angular orientations will vary between the values for these cases.) For a vertically mounted probe, the orientation with the shorter side vertical provides the largest natural convection contribution.

Natural convection is a function of the Grashof-Prandtl number product. The Grashof number, Gr, is defined as

$$Gr \equiv \frac{g \beta (\bar{T}^*_p - T^*_\infty) L^{*3}}{\nu^2}$$

where,

g = acceleration of gravity

β = thermal volumetric expansion coefficient, and

L*= characteristic dimension of the heated surface.

As an upper bound to the magnitude of the heat transfer due to natural convection, we consider a probe mounted vertically with its shorter side vertical. Taking T*=20 °C and L*=0.1cm, a characteristic spanwise probe dimension and conditions typical of the the particular fluid, we can find the average

Nusselt number for natural convection from experimental correlation (Holman, p.216, 1972). We estimate the effective Nusselt number due to natural convection, Nu_{NC}, as:

fluid	air	water
$\frac{g\beta\ Pr}{\nu^2}\ (cm^3{}^\circ C)^{-1}$	31	$4.2 \cdot 10^4$
$\bar{T}_p^* - T_\infty^*(°C)$	45	230
$Gr \cdot Pr$	7.1	1900
Nu_{NC}	1.2	2.2

These values should be compared to the zero-flow Nusselt numbers for pure conduction (Appendix E). Thus, natural convection represents a small, sometimes non-negligible, component of heat transfer that is much more important for water than air despite the higher temperature at which the probe is commonly operated in air than in water. This is further emphasized when it is realized that the zero-flow Nusselt numbers are much less for water than for air due to the lower conductivity ratios achieved with water.

It is difficult to find measurements of natural convection at such low values of GrPr. However, it is safe to say that natural convection will be less important for other probe orientations. For somewhat higher values of GrPr, correlations show that the heat transfer from a downward

facing heated surface is about half that from an upward facing surface (Holman, p.218 1972; Hassan and Mohamed 1970) which, in turn, is much less than for a vertical surface. For orientations at an angle from the vertical, the heat transfer can be predicted by forming Gr with the component of gravity parallel to the surface (Hassan and Mohamed (1970)). This is true for angles from the vertical as large as 75 degrees.

5. Extensions and Implications of the Theory

In this Chapter we further discuss the implications of our theory and findings for probe use and design and for future research. We also briefly investigate the ways that our theory might be expanded to handle more complicated flow conditions and discuss implications for unsteady flow calculations. Applications to related velocity and shear measuring techniques and to more general problems of heat, mass, and vorticity transfer to a wall bounded shear flow are discussed.

5.1 Implications for Probe Use and Design

Our calculations indicate that probe performance can vary greatly depending on ambient conditions and probe design. Essentially, all three governing parameters (Pe, K, b/a) are at least partially controllable by design. A caveat must be issued here that features desirable for steady flow performance may not be best for unsteady performance. As an example, to maximize the flow sensitive portion of the total heat transfer, it is desirable to have a low K. This can be achieved by finding a low conductivity substrate. However, for a good frequency response in unsteady flows, a large thermal diffusivity is desirable. While thermal conductivity and thermal diffusivity are not the same, they are

proportional to one another, and thus a tradeoff exists.

It has been demonstrated that larger aspect ratio probes both have a greater shear sensitivity (larger calibration curve slope) at low and moderate Peclet numbers and a lower background or zero-flow heat transfer. Both of these are desirable features. They also exhibit a large directional sensitivity. A potential disadvantage of large aspect ratio probes is that they respond to the average of the local shear stress over a large spanwise area.

Ideally, it is desirable to operate at large Peclet numbers both to increase the shear sensitivity and to increase the flow-sensitive fraction of the total heat transfer. This can be achieved by use of a large enough streamwise probe length. Once the fluid and the expected shear stress range is known, an operating Peclet number range can be fixed by specification of the streamwise probe length. In practice, a small length is desirable both from a spatial resolution standpoint and from the desire to confine the probe's thermal boundary layer to the linear region of the fluid velocity field. One may choose to operate at a lower Peclet number and use our theory to predict probe performance.

Substrate conduction has been seen to often be the dominant mode of heat transfer. However, the primary role of conduction is to increase the background or zero-flow heat transfer. Its coupling to the flow-sensitive heat transfer is seen to be very mild for homogeneous substrates, particularly

for low aspect ratio probes. It may thus be feasible to determine a universal flow-sensitive calibration curve for a given geometry probe over a fairly wide range of conductivity ratios. The zero-flow value would vary, but could be obtained from a single stagnant flow measurement (or prediction).

Our simple analysis has shown that streamwise variation in substrate conductivity can strongly influence probe sensitivity to shear. This suggests the possibility of designing a probe composed of more than one subtrate material to elicit a desired shear sensitivity. Probe directional sensitivity (or insensitivity) might also be achieved by this mechanism. Common experimental probe configurations composed of a typically pyrex or quartz substrate surrounded by other materials, air gaps, etc. complicate the prediction of probe performance. The performance of a probe with a homogeneous substrate large enough to contain the region of thermal influence of the probe would be more easily predicted by our theory.

Pernaps the greatest implication of our theory for probe design is that new designs can be tested in detail before the costly and time-consuming process of fabrication is begun. Parametric studies can be performed with ease.

5.2 Extensions to More Complex Conditions

Other Probe Conditions

The specification of a uniform generation rate for the heated film was shown in Chapter 4 to be a good approximation to current probe designs. However, if desired, a nonuniform generation rate can be simply specified as the source function in (2.9). Depending upon the complexity of that distribution, it may be necessary to obtain its form in wavenumber space numerically. Source geometry need not be rectangular. This allows analysis of probes of various shapes. Other shapes that have either been used or proposed include V-shaped probes (McCroskey and Durbin 1972), circular (Aggarwal 1978), and ring-shaped probes. Such configurations enable the determination of the direction as well as the magnitude (V-shaped) of the shear or are relatively insensitive to shear direction (circular and ring) - of great advantage when the local flow direction is either not known or varies with time. Investigation of multiple-film probes is also feasible - either through the use of a multi-part source function or by taking advantage of the linearity of the governing equations and superposing the solutions for individual films. Such devices can be used to detect flow direction in locally reversing flows. (Rubesin, et. al. 1975 used multiple heated wires imbedded in the wall surface for this purpose.)

Nonlinear Velocity Profiles

Our analysis specifies the velocity field in the vicinity of the probe as being linear. This presumes that the thermal boundary layer over the probe is contained entirely within the approximately linear region of the velocity field. Due to the small streamwise length of the typical probe (of the order of 0.1mm), this assumption is valid when the momentum boundary layer has begun to develop upstream of the probe, when Pr >> 1 as is the case for most liquids, or when the conditions for linearity are imposed by the flow geometry as in Couette flow or flow in a pipe whose diameter is very large compared to the probe streamwise length.

Spence and Brown (1968) have estimated the effect of a quadratic velocity profile set up in a laminar boundary layer by the presence of streamwise pressure gradients. If desired, our analysis can be modified to consider velocity profiles that are not linear. This involves modification of the fluid energy equation (2.6) and results in a different fluid-side ordinary differential equation to be solved in wavenumber space. Once this solution is obtained, the balance of our solution procedure can be followed with the Airy functions of (2.27-2.29) replaced by other expressions.

Unsteady and Turbulent Flows

The analysis of the response of hot-film probes to unsteady flows is much more complicated than the steady flow

analysis. Introduction of the independent variable of time adds a fourth dimension to an already three-dimensioanl calculation. Perhaps more important are additional physical phenomena that come into play. These include the need to adequately account for the thermal capacities of both the fluid and the substrate, and to determine the details of the velocity field unsteadiness including the very important determination of whether there is local flow reversal. Analytically, the problem is more complicated than a time-varying boundary condition or source function since the dependence is contained in the convective term of (2.1). Thus, taking a Fourier or Laplace transform in time involves the transformation of a product of two terms that are functions of time - the shear and the streamwise temperature gradient. This introduces a convolution integral and much difficulty. Attempts to look at hot-film performance in unsteady flows have often been based on small perturbations superimposed on the steady shear flow or on the two limiting cases of quasi-static performance and high frequency fluctuations (Fortuna and Hanratty 1971). Dewey and Huber (1982) and Hanratty and Campbell (1982) provide comprehensive reviews of both the analytic and experimental literature concerning hot-film probe use in unsteady and turbulent flows.

It is hoped that some of the insights gained in our steady flow analysis will be helpful in examining the unsteady case. Results that offer particular promise in simplifying

unsteady calculations include: the prediction that the downstream region of the substrate participates much less in the heat transfer process than the balance of the substrate; the ability to calculate the extent of thermal penetration in the substrate and fluid as functions of the governing parameters; and the weak coupling of the fluid and substrate heat transfers leading to a relatively easily calculated approximation for probe Nusselt number (4.10).

Turbulent flows can be viewed as an extreme of unsteady flows - possessing a spectrum of fluctuation time scales. Measurement of the mean value of the turbulent shear is more tractable than measurement of the instantaneous shear. A number of researchers have investigated the question of whether a universal calibration curve can be obtained for a given probe for use in both laminar and mean turbulent flow measurements, and various criteria have been proposed (Brown 1967, Pope 1971, 1972). The basic concept relies on the existence of a viscous sublayer near the wall which can be thought of as a uniform shear region. In general, the criteria involve confining the probe's thermal boundary layer to the viscous sublayer or some fraction of it. Under these conditions, our theory might be applicable for measurement of the mean turbulent shear. However, there are a number of uncertainties: probe frequency response limitations are not included; corrections to the measured mean shear are needed due to the nonlinear relation between heat transfer and shear

(Sandborn 1979); the effects of cross-stream shear fluctuations on the heat transfer are not accounted for; and a comprehensive universally accepted model of the sublayer does not exist. It thus seems prudent that, until further investigations are performed, our theory should be used only as a guide for probe use in turbulent flow.

5.3 Related Measurement Techniques

The electrochemical technique for shear stress measurement relies on mass transfer principles governed by equations identical to those for heat transfer. The major conceptual difference in operation is the lack of participation by the substrate in the transfer process. Thus all of our predictions for an adiabatic substrate ($K = 0$) are directly applicable to elctrochemical probes. We have used this attribute in comparing some of our predictions with electrochemical measurements (Chapter 4). Hanratty and Campbell (1982) provide an excellent review of the use of electrochemical techniques.

Heated wires embedded in the wall surface have also been used to measure wall shear stress (Liepmann and Skinner 1954, Murthy and Rose 1978). Operation is similar to that of a hot-film probe. The small streamwise dimension (the wire diameter) in general leads to operation at lower Peclet numbers. Adaptation of our theory to these devices involves

specifying a finite length line source as the source function in (2.9).

A problem that has plagued investigators desiring fluid velocity measurements close to the wall is that of heat transfer to the wall from a hot-wire or hot-film velocity probe. One should be able to obtain a good estimate of the effect of this wall interference by inclusion of a finite length line source in the fluid at the appropriate wire location. This involves modification of the governing equations (2.6) and (2.9). The finite length line source leads to an inhomogeneous term in the fluid equation (2.6) that has the form of the product of a delta function and a top-hat function. The surface source term in (2.9) would then be set to zero. This requires a different solution of the resulting ordinary differential equations in y, but the procedure should be similar.

A recent technique developed by Ajagu, Libby, and LaRue (1982) combines a hot-wire near the wall with a surface hot-film used as a guard heater that aids in overcoming the problem of heat transfer to the wall. Such a device is also a likely candidate for analysis by adaptation of our theory. In addition to the finite length line source discussed above, the source function in eq (2.9) must be set to model the surface hot-film.

5.4 Related Problems

The form of the governing equations and the nature of our solution procedure suggest application to a much broader class of problems involving transfer processes. These related problems are briefly discussed in this Section.

Mass and Vorticity Transport

The transport of mass and vorticity in shear flows are physical processes precisely analogous to the transport of heat. Mass transport has been briefly discussed in relation to electrochemical probes above. Equation (2.6) has an exact parallel in the linearized vorticity transport equation for a uniform shear flow:

$$\frac{1}{Re} \nabla^2 \omega - s y \frac{\partial \omega}{\partial x} = 0$$

where Re is the flow Reynolds number and ω is the z component of the vorticity defined as $\frac{\partial v}{\partial x} - \frac{\partial u}{\partial y}$. Here v is the velocity in the y directon and u is the streamwise velocity deviation from the linear profile. Equations of similar form also govern the transport of passive contaminants in a uniform shear flow. In general, it is difficult to imagine the mass or vorticity transport analogs to the thermally conducting substrate. Thus, the adiabatic wall predictions would seem most applicable to mass and vorticity transfer.

Wall Point Source in a Uniform Shear

A problem of fundamental interest is the determination of the temperature distribution from a point source of heat on a wall with a uniform shear flow. Completely analogous problems are point sources of mass or vorticity. Although solutions are known for point sources in unbounded shear flows (Elrick 1962) and for a point source suspended in a bounded shear flow (Berlyand 1959, 1961) no solution has been found for a bounded shear flow with a point source on the wall. Our model is able to analyze this problem for both conducting and insulated walls by use of a point source function in (2.9).

Surface Source Distributions

Due to the linear nature of the governing equations and solution formulation in terms of an arbitrary surface source distribution, it is possible to use our formulation for the much more general problems of heat or mass transfer to a uniform shear flow bounded by a conducting wall on which there is an arbitrary but specified surface source distribution. Such an applications might include the cooling of a radiatively-heated surface by a shear flow if the distribution of absorbed heat at the surface can be specified or the transfer of mass from a surface of prescribed concentration.

6. Conclusions

A comprehensive three-dimensional theory for the performance of flush-mounted hot-film wall shear stress probes in steady incompressible flows has been developed. The theory involves solution of the complete coupled three-dimensional fluid and solid energy equations to obtain selected detailed temperature and heat flux distributions. The combined analytic and numerical evaluation enables calculations to be carried out along any plane parallel to the wall thus achieving the efficiency of a two-dimensional calculation while retaining all of the three-dimensional physics. The solution by a Fourier transform technique results in the finding of a Green's function in wavenumber space for heat transfer to a uniform shear flow over a conducting wall. The specification of an arbitrary probe geomatry and heat source distribution permits the investigation of wide ranges of probe designs and renders the theory applicable to problems of flow over solids possessing surface heat source distributions. The theory is also directly applicable to the analogous problems of mass and vorticity transport.

We have implemented the theory for the case of a rectangular uniform heat source probe to obtain predictions over wide ranges of the governing parameters of Peclet number, the ratio of substrate to fluid conductivities, and probe aspect ratio. The results of a parametric study of probe

Nusselt number over the ranges of:

$$0.06 \leq Pe \leq 400$$

$$0 \leq K \leq 50$$

$$0.5 \leq b/a \leq \infty ,$$

illustrate both the versatility of our theory and the importance of geometry and substrate conduction. Of particular interest is the coupled effect of geometry and substrate conduction.

The probe Nusselt number based on total heat transfer can be expressed as the sum of two components: a flow-sensitive portion that varies with the applied shear and a flow-insensitive or "background" component due primarily to conduction in both the fluid and the substrate. This component is not useful in shear measurement and can be subtracted from the total Nusselt number to obtain the flow-sensitive portion. An exact analytic expression for the probe heat transfer at zero flow - i.e., heat transfer to a conducting substrate and a stagnant fluid - has been found. The zero-flow Nusselt number is found to be strongly influenced by probe aspect ratio: it is at a minimum for a two-dimensional probe and increases with decreasing aspect ratio. Its value is directly related to the ratio of substrate and fluid conductivities and is often much larger than the flow-sensitive portion of the total Nusselt number. This is particularly true for air flows because the thermal conductivity of air is low. Experimentally obtained values

of the heat transfer at zero flow may also contain contributions due to radiation and natural convection. Estimates show that the contribution of radiative heat transfer is negligible for typical operating conditions. The effects of natural convection are estimated to vary with particular conditions. In general, natural convection effects should be insignificant for air flows, but may be of some consequence for water flows depending upon probe orientation. This should only be a concern at low flow rates or for zero-flow measurements.

Investigation of the partition of heat transfer from the probe shows that for many practical applications the component of heat transferred directly to the substrate is much larger than that transferred directly to the fluid - an expected finding based on the relative sizes of the flow-sensitive and zero-flow portions of the probe Nusselt number. To a first approximation, the heat generated at the probe divides between the fluid and the substrate in proportion to their relatve thermal conductivities. This division is exact for the zero-flow pure conduction case.

The small influence of substrate conductivity exhibited by the predicted flow-sensitive Nusselt numbers suggests that the coupling between the fluid and substrate heat transfer is weak. This behavior can be exploited to express the probe Nusselt number as the sum of two components:

$$Nu(Pe,K,b/a) = (K+1)\ Nu_{00} + \tilde{Nu}_{fs}(Pe,b/a) \qquad (4.10)$$

This expression has been found to predict total Nusselt number to within 4% of the coupled calculations over all values tested if $\tilde{Nu}_{fs}$ is evaluated as the Nusselt number for K=0. If $\tilde{Nu}_{fs}$ is evaluated as some average value over a range of K, the accuracy is better than 2%.

Detailed heat flux and temperature fields vary widely with the governing parameters. Analysis shows that all of the heat transferred directly into the substrate flows through the substrate into the fluid. The region upstream of the probe and laterally adjacent to the probe are seen to contain the majority of this heat exchange. The heat exchange between the fluid and the substrate downstream of the probe is of much smaller magnitude and its direction is dependent upon probe aspect ratio. The downstream transfer is usually from the fluid to the substrate, but can be from the substrate to the fluid over a portion of the downstream area for larger aspect ratio probes. The heat transfer is completely from the substrate to the fluid for two-dimensional probes.

Our predictions show excellent agreement with limiting value theories throughout the range of investigation. Direct comparison with experiment is difficult due to the paucity of data available for which calibration curves in dimensionless form can be obtained and the non-ideal conditions under which many experiments are conducted. However, predictions are

consistent with available data. The need for experiments in which the conditions are carefully controlled and documented is apparent.

A simple analysis has shown that streamwise variation of substrate conductivity can create a flow-sensitive average or "effective" substrate conductivity that can have an important effect on probe sensitivity to shear. Investigation of common experimental probe configurations in which the sensor substrate is surrounded by material of a different thermal conductivity indicates that this mechanism can qualitatively account for observed calibration curve slopes. Such slopes are not accurately predicted by models that assume the substrate possesses a single homogeneous thermal conductivity.

References

Abramowitz, M. and Stegun, I.A., Eds. (1972), Handbook of Mathematical Functions with Formulas, Graphs, and Mathematical Tables, National Bureau of Standards, Washington, D.C.

Ackerberg, R.C., Patel, R.D., and Gupta, S.K. (1978), J. Fluid Mech., 86, 49.

Aggarwal, J.K. (1978), J. Phys. E.: Sci. Inst., 11, 349.

Ajagu, C.O., Libby, P.A., and LaRue, J.C. (1982), Rev. Sci. Instrum., 53, 1920.

Bellhouse, B.J., and Schultz, D.L. (1966), J. Fluid Mech., 24, 379.

Bellhouse, B.J., and Schultz, D.L. (1967), J. Fluid Mech., 29, 289.

Bellhouse, B.J., and Schultz, D.L. (1968), J. Fluid Mech., 32, 675.

Bender, C.M., and Orszag, S.A. (1978), Advanced Mathematical Methods for Scientists and Engineers, McGraw-Hill Book Company, New York.

Berlyand, O.S., Inzhenerno-Fizicheskii Zhurnal, No. 5, 1959, 70.

Berlyand, O.S., International J. Heat and Mass Transfer, Vol 4, 1961, 127.

Blackwelder, R.F. (1981), Hot-wire and Hot-film Anemometers, In Methods of Experimental Fluids, Vol. 18, Part A, Emrich, R.J., Ed., Academic Press, New York, 259.

Blinco, P.H., and Simons, D.B. (1974), J. Eng. Mech. Div., Proc. ASCE 100, EM2, 203.

Brown, G.L. (1967), Proc. 1967 Heat Transfer and Fluid Mechanics Institute, Stanford U. Press, 361.

Brown, G.L., and Davey, R.F. (1971), Rev. Sci. Inst., 42, 1729.

Carslaw, H.S., and Jaeger, J.C. (1959), Conduction of Heat in Solids, Oxford University Press, Oxford.

Davies, P.A.O.L., and Kimber, G.R. (1972), in Conference on Fluid Dynamic Meas. in the Industrial and Medical Environments, Vol. I., D.J. Cockrell, Ed., Leicester U. Press, Leicester, 236.

Dewey, C.F., Jr., and Huber, P.W. (1982), Fluid Mechanics Laboratory Publication 82-4 (Department of Mechanical Engineering, Massachusetts Institute of Technology).

References

DISA Electronics (1980), Probe Catalog, Denmark.

Elrick, D.E., Australian J. Physics, Vol. 15, 1962, 283.

Fortuna, G., and Hanratty, T.J. (1971), Int. J. Heat & Mass Transfer, 14, 1499.

Gougat, P., Kestin, J., and Brun, E.A. (1966), Comptes Rendus de l'Academie des Sciences de Paris, 263, 810.

Hanratty, T.J., and Campbell, J.A. (1982), "Measurement of Wall Shear Stress", in Fluid. Mech. Meas. (R.J. Goldstein, Ed.), Hemisphere Publ. Corp. (in press).

Hassan, K., and Mohamed, S.A. (1970), Int'l. J. Heat & Mass Transfer, 13, 1873.

Holman, J.P. (1972), Heat Transfer, McGraw-Hill Book Company, New York

Kaminski, D.A., Ed. (1977), Heat Transfer and Fluid Flow Data Books, General Electric Co. Corporate R & D, Schenectady, New York.

Kreysig, E. (1967), Advanced Engineering Mathematics, 2nd ed., Wiley, New York.

Leveque, M.A. (1928), Annales des Mines, 13, 201.

Liepman, H.W., and Skinner, G. (1954), "Shearing stress measurements by use of heated element," NACA TN 3268.

Ling, S.C. (1963), J. Heat Trans., 85C, 230.

McCroskey, W.J., and Durbin, E.J. (1972), Trans. ASME (J. Basic Eng'g.), 94, 46.

Murthy, V.S., and Rose, W.C. (1978), AIAA Paper 78-798.

Pardo, D.F., S.M. Thesis, M.I.T. Department of Mechanical Engineering, September 1980.

Pope, R.J. (1971), "The Use of Thin-film heated Elements in Water Flows," Ph.D. Thesis, Oxford U. See also AIAA J., 10, 729 (1972).

Reichert, J.K., and Azad, R.S. (1977), Rev. Sci. Instrum., 48, 341.

Rohsenow, W.H., and Choi, H. (1961), Heat, Mass, and Momentum Transfer, Prentice-Hall, Inc., Englewood Cliffs, New Jersey.

References

Rubesin, M. W., Okuno, A.F., Mateer, G.G., and Brosh, A. (1975), Int'l. Congress on Instrumentation in Aerospace Simulation Facilites, Sept. 22-24, Ottawa, Canada.

Sandborn, J.A. (1979), ASME Paper 79-WA/FE-17.

Spence, D.A., and Brown, G.L. (1968), J. Fluid Mech., 33, 753.

Tanner, R.I. (1967), Trans. ASME (J. Appl. Mech.), 34, 801.

TSI Inc. (1978), Hot Wire-Hot Film Anemometer Systems, St. Paul, MN.

White, F.M. (1974), Viscous Fluid Flow, McGraw-Hill, New York.

Winter, K.G. (1977), Prog. Aerospace Sci., 18, 1.

Appendices

A. Numerical Evaluation of Airy Functions

The Airy function and its first derivative found in integrand (2.29) and related expressions are evaluated by series expansions. A Taylor series expansion is used for small values of the argument, and an asymptotic series is used for larger values of the argument (Abramowitz and Stegun 1970, Bender and Orszag 1978). The Taylor series is given by:

$$\mathrm{Ai}(z) = 3^{-2/3} \sum_{n=0}^{\prime} \frac{z^{3n}}{9^n n!\,\Gamma(n+\frac{2}{3})} - 3^{-4/3} \sum_{n=0}^{\prime} \frac{z^{3n+1}}{9^n n!\,\Gamma(n+\frac{4}{3})}.$$

The asymptotic series representation is:

$$c_0 = 1,\ c_k = \frac{\Gamma(3k-\frac{1}{2})}{54^k k!\,\Gamma(k+\frac{1}{2})} = \frac{(2k+1)(2k+3)\ldots(6k-1)}{216^k k!},$$

$$d_0 = 1,\ d_k = -\frac{6k+1}{6k-1}\, c_k \qquad (k=1, 2, 3, \ldots)$$

$$\zeta = \frac{2}{3} z^{3/2}$$

$$\mathrm{Ai}(z) \sim \frac{1}{2}\pi^{-1/2} z^{-1/4} e^{-\zeta} \sum_{0}^{\infty} (-1)^k c_k \zeta^{-k} \qquad (|\arg z| < \pi)$$

$$\mathrm{Ai}'(z) \sim -\tfrac{1}{2}\pi^{-1/2} z^{1/4} e^{-\zeta} \sum_{0}^{\infty} (-1)^k d_k \zeta^{-k} \qquad (|\arg z| < \pi)$$

For our purposes, the argument z is usually η or η_0 (expressions (2.19) and (2.25), respectively).

Asymptotic series may initially converge, and then begin

to diverge as the number of terms is increased. Thus, tests were conducted to find the optimal number of terms needed. Tests were also performed to determine the argument value at which to change from evaluation by one series to evaluation by the other. The value chosen was $|z| = 2.2$. For $|z| < 2.2$, a five term Taylor series is used. For $|z| > 2.2$ a four term asymptotic series is used. Tests indicate that this yields an accuracy of better than 0.2 % when compared to tabulated values (Abramowitz and Stegun 1970). The accuracy is significanly better for values of $|z|$ not near 2.2 since the Taylor and asymptotic series become better approximations for smaller and larger arguments, respectively. Four is the optimum number of terms in the asymptotic series for values of $|z|$ near 2.2. For larger argument values, the optimum number of terms increases thus increasing the maximum possible accuracy. However, the accuracy of a fixed number of terms (e.g., 4) also increases with larger arguments. Thus the number of terms was fixed at four, with 0.2 % as a lower bound on the accuracy. In no cases for $|z| > 2.2$ has the asymptotic series begun to diverge with four terms.

B. Numerical Consiserations

In this Appendix, we present some of the details of the numerical implementation of the analysis we develop in Chapter 2. Some of the more important numerical attributes are discussed in Section 2.3. Our discussion in this Appendix is is concentrated in three areas: evaluation of the singularity which occurs in (2.32) and related expressions, presentation of an inequality constraint between the discretizations of p and q, and comments on the selection of the discretization and truncation.

Singularity evaluation

The integrand (2.32) of the temperature field inversion integral is singular at $(p,q)=(0,0)$, as it should be. This, however, poses a problem for the numerical evaluation because there is no direct method for incorporating an infinite value over an infinitesimal interval in a discretized scheme. We overcome this difficulty by realizing that the value of the integrand at some point of a numerical integration actually takes the place of an averaged value of the integrand over the discretization interval associated with that point. Although our integrand is singular at $(p,q)=(0,0)$, the integrated value of it over a small interval surrounding (0,0) is finite. Thus, we average (2.32) over the discretization interval

centered at (0,0) by integraing over this interval and use this integrated average value as the value of (2.32) at (0,0).

To take into acount calculations of the temperature field, we investigate the behavior of the more general expression (2.31) for $y \geq 0$. This expression can be rewritten as:

$$\hat{G} = \frac{e^{\pi\lambda/6}}{(2\pi p)^{1/3}} \frac{A_\lambda(\eta)/A_\lambda(\eta_0}{K \frac{2\pi\sqrt{p^2+q^2}}{(2\pi p)^{1/3}} e^{\pi\lambda/6} \frac{A_\lambda(\eta_0)}{A_\lambda'(\eta_0)} - 1}$$

$$= \frac{e^{\pi\lambda/6}}{(2\pi p)^{1/3}} \frac{A_\lambda(\eta)/A_\lambda'(\eta_0)}{K\sqrt{\eta_0} \frac{A_\lambda(\eta_0)}{A_\lambda'(\eta_0)} - 1} \qquad \text{(B.1)}$$

where, as before,

$$\eta = \frac{(2\pi p)^{1/3}}{e^{\pi\lambda/6}} \left(y + i2\pi \frac{p^2+q^2}{p} \right) \qquad \text{(B.2)}$$

$$\eta_0 = \eta_{y=0} = \frac{e^{\pi\lambda/3}}{(2\pi)^{4/3}} \frac{p^2+q^2}{p^{2/3}} \qquad \text{(B.3)}$$

The limiting value of (B.3) is:

$$\lim_{(p,q)\to(0,0)} \eta_0 = 0 \qquad \text{(B.4)}$$

This is true if the p and q go to zero alomg any line other than the q axis - i.e., other than p=0. The behavior in this case can be ignored. The limit of η is the same. However,

since we will be investigating the behavior for small values of p and the second term on the right of (B.2) approaches zero much faster than the first, we retain the first term and say

$$\eta \sim e^{-\pi i/6}(2\pi p)^{1/3} y \qquad as\ (p,q)\to(0,0) \tag{B.5}$$

Thus, we approximate (B.1) near (p,q)=(0,0) as:

$$\hat{G} \sim -\frac{e^{\pi i/6}}{(2\pi p)^{1/3}} \frac{A_i\left(\frac{(2\pi p)^{1/3}}{e^{\pi i/6}} y\right)}{A_i'(0)} \tag{B.6}$$

We expand Ai in (B.5) in a Taylor Series (Abramowitz and Stegun 1970):

$$A_i(z) = A_i(0) + A_i'(0)\cdot z + \cdots$$

Thus, (B.6) becomes

$$\hat{G} \sim \frac{e^{\pi i/6}}{(2\pi p)^{1/3}} A - y \tag{B.7}$$

where

$$A \equiv -\frac{A_i(0)}{A_i'(0)} = 1.3717\ldots \tag{B.8}$$

The integrated average value of (B.7) over the discretization interval centered at (0,0) is given by:

$$\frac{1}{\delta p\,\delta q}\int_{-\delta p/2}^{\delta p/2}\int_{-\delta q/2}^{\delta q/2}\left\{A\frac{e^{\pi i/6}}{(2\pi p)^{1/3}} - y\right\} dp\,dq$$

$$= \frac{A\, e^{\pi i/6}}{(2\pi)^{1/3}} \cdot \frac{3}{4} \left[\left(\frac{\delta p}{2}\right)^{2/3} - \left(-\frac{\delta p}{2}\right)^{2/3} \right] \Big/ \delta p/2 \; - y \qquad \text{(B.9)}$$

If we take the lowest phase complex root to evaluate the second term of the numerator of (B.9), (B.9) becomes:

$$\frac{3}{4} A \frac{e^{\pi i/6}}{(2\pi)^{1/3}} \left(\frac{\delta p}{2}\right)^{-1/3} \left(e^{\pi i/6} - e^{5\pi i/6}\right) - y \qquad \text{(B.10)}$$

This is the value we use for the integrand at $(p,q)=(0,0)$.

We also evaluate espression (B.1) for points along the q axis - i.e., where p but not q is zero. Under these circumstances, both η and η_0 go to infinity. Using the asymtotic behavior of Airy functions for large arguments (Appendix F), (B.1) becomes:

$$\hat{G}_{\substack{p\to 0 \\ q\neq 0}} \sim \frac{1}{2\pi(K+1)\,|q|} \qquad \text{(B.11)}$$

This value is used for the integrand along the q axis, except at the origin where (B.10) is used.

Constraint between the p and q discretizations

The use of (B.10) and (B.11) introduces a constraint between the sizes of p and q which amounts to a consistency

in the use of approximations (B.10) and (B.11). Basically, the approximated behavior of the integrand as q approachews zero along the q axis (given by (B.11)) must be consistent with the approximated average behavior of the integrand over the interval near the origin (given by (B.10)). Conceptually, the integrand must continue to increas along the q axis until in gets to the origin. Since (B.10) varies inversely with p, but (B.11) is independent of δp, (B.11) can actually be larger than (B.10) if δp is sufficiently larger than δq. This, of course is inconsistent since the integrand increases to infinity as the origin is approached along the q axis. In practice, we have found that when (B.11) is not sufficiently smaller than (B.10), errors in the temperature fields in physical space occur. This is often manifested by ripple and calculated temperatures significanly less than zero.

To derive a criteria for the needed relation between the discretizations, we consider (B.11) evaluated at $q = \delta q$ and (B.10) evaluated at y=0, and require

$$\frac{(B.11)}{(B.10)} < C \qquad (B.12)$$

Evaluating this expression, we find:

$$\frac{(2\pi)^{4/3}}{2\pi(K+1)\cdot\frac{3}{4}\cdot A\left(e^{\pi 1/6}-e^{5\pi 1/6}\right)} \cdot \frac{(\delta p/2)^{1/3}}{\delta q} < C$$

$$\frac{0.13}{K+1}\left(\frac{\delta p}{\delta q}\right)^{1/3} < C \qquad \text{(B.13)}$$

We have found the value of C to be about 0.55 - 0.6 through numerical experimentation. A surprisingly small increase over these values can lead to problems. Selection of a value of the integrand ratio significanly less than 0.6 does not seem to produce any problems of the type discussed here, although such a selction may not be reasonable due to other factors such as adequate resolution, etc.

Discetization and Truncation Selection

Some of the factors affecting the choice of the discretization and truncation of the inversion integrals are discussed in Section 2.3. Some additional details are discussed here.

To best represent the decaying sinusoidal nature of the integrand with a source distribution whose transform is of the form of (2.44). we have found it advisable to select the discretization sizes such that an integral number of steps is incuded within the half period of the sinusoids of (2.44). This enables the zeroes of this function to be sampled exactly. Failure to do this has resulted in the introduction of spurious conmponents into the com puted temperature and heat flux fields.

We have found it advisable to truncate the integrand such that there is little difference between its value at the beginning and end of the truncation interval. (This precludes jumps between these values in the discrete inversion. These arise from the fact that Fourier transformation treats the truncated function as one period of an infinite periodic function, thus effectively placing the first and last points of this function together.) Ideally, the integrand will have decayed to zero at these points. In practice, this may involve calculation over a much larger range than is desirable or otherwise necessary. For the temperature field calculations, we have found it useful to make the truncation points zeroes of the sinusoidal source function, and thus also of the integrand. Thus, the maximum of p or q are integral numbers of half-periods of the respective sinusoidal source components.

For the heat flux calculations, we have found it necessary to perform the truncation at a maximum or a minimum of the sinusoids. Thus the maximum values of p and q are integral numbers of half-periods plus a quarter period of the respective sinusoids. We believe this to be due to the step-like change in the heat flux at the probe edges. Truncation in the manner used for temperature fields results in a distribution in physical space of the calculated points such that the probe boundaries pass through points of calculation. This is fine for the temperature field because

it is relatively smooth. However, the step-like behavior of the flux is a problem for this arrangement of the calculated points. The alternate arrangement that we use for the heat flux, results in a distribution of points in physical space such that the probe boundary passes midway between two points at which the flux is calculated.

C. Expressions in Wavenumber Space for Decoupling the Fluid and Substrate Heat Transfer

As discussed in Section 4.4, our predictions indicate that the coupling between the fluid and substrate heat transfers is weak and that accurate approximations of probe Nusselt number can be obtained from simplified expressions based on this weak coupling. In this Appendix, we investigate the conditions under which the fluid and substrate heat transfers can be decoupled and show that they are completely decoupled if the source function Q is the product of a pure sinusoid in x and in z. The fact that coupling is weak over the wide range of cases we have investigated indicates that the nonlinear effects due to the inclusion of many Fourier components in Q - i.e., to create a uniform rectangular source - are not large. This suggests that simplified predictive schemes based on this decoupling may also work well for other conditions and probe geometries.

We investigate the behavior of our solution in wavenumber space using the Green's function formulation of (2.31)-(2.32). We investigate the surface (y=0) temperature distribution and, for brevity, denote $\hat{G}_0$ simply as $\hat{G}$. The Green's function for flow over an adiabatic wall is found by setting K=0 in (2.32) and denoted by $\hat{G}_f$. We have:

$$\hat{G}_f = \frac{-e^{i\pi/6} Ai(\eta_0)}{(2\pi p)^{1/3} Ai'(\eta_0)} \qquad (C.1)$$

The Green's function for pure conduction to the substrate is given in Appendix F. We separate out the coductivity ratio and define:

$$\hat{G}_s = \frac{1}{2\pi\sqrt{p^2+q^2}} \tag{C.2}$$

Comparison of (2.32), (C.1), and (C.2) shows that

$$\frac{1}{\hat{G}\hat{Q}} = \frac{K}{\hat{G}_s\hat{Q}} + \frac{1}{\hat{G}_f\hat{Q}} \tag{C.3}$$

Section 4.4 shows that with complete decoupling of the fluid and substrate heat transfers, the probe Nusselt number is expressible as:

$$Nu(Pe,K,b/a) = K\,Nu(Pe=0,K=0,b/a) + Nu(Pe,K=0,b/a).$$

This suggests that the temperature field might be expressible as:

$$\frac{1}{T} = \frac{K}{T(Pe=0,K=0)} + \frac{1}{T(K=0)} \tag{C.4}$$

We know that

$$T = F\{\hat{G}\hat{Q}\} \tag{C.5}$$

$$T(P_e=0, K=0) = F\{\hat{G}_s \hat{Q}\} \tag{C.6}$$

$$T(K=0) = F\{\hat{G}_f \hat{Q}\} \tag{C.8}$$

where F denotes inverse Fourier transformation. Thus, we would like to know when

$$\frac{1}{F\{\hat{G}\hat{Q}\}} = \frac{K}{F\{\hat{G}_s\hat{Q}\}} + \frac{1}{F\{\hat{G}_f\hat{Q}\}} \tag{C.9}$$

From (C.3) we know that

$$F\left\{\frac{1}{\hat{G}\hat{Q}}\right\} = K \cdot F\left\{\frac{1}{\hat{G}_s\hat{Q}}\right\} + F\left\{\frac{1}{\hat{G}_f\hat{Q}}\right\} \tag{C.10}$$

The question then is when is (C.9) true given (C.10). This is the case if $\hat{Q}$ is a product of delta functions:

$$\hat{Q} = \delta(p-\tilde{p})\,\delta(q-\tilde{q}) \tag{C.11}$$

Use of (C.11) reduces both (C.9) and (C.10) to the smae expression (after cancellation of the exponentials from the transforms):

$$\frac{1}{\hat{G}(\tilde{p},\tilde{q})} = \frac{K}{\hat{G}_s(\tilde{p},\tilde{q})} + \frac{1}{\hat{G}_f(\tilde{p},\tilde{q}}$$

Thus, the decoupling is exact when $\hat{Q}$ is of the form (C.11) - i.e., Q is of the form $Q = \sin 2\pi\tilde{p}x \sin 2\pi\tilde{q}z$.

D. Derivation of Scaling Expressions for Upstream Thermal Penetration

In this Appendix, we derive expressions for the scaling of the upstream thermal penetration length L_T^* of the temperature field at y=0 due to heat transfer from a probe mounted on a substrate of homogeneous thermal conductivity (4.12) and on a substrate in which there is a step change in thermal conductivity at some distance L_b^* upstream of the probe.

Consider first the homogeneous substrate case as sketched in figure D.1: a fluid with a linear velocity profile u = sy, thermal conductivity k_f, density ρ, and specific heat c, flows over a substrate of homogeneous thermal conductivity k_s on which is mounted a two-dimensional probe of streamwise length Lp*. The temperature at any point along the substrate surface (y=0) at a distance L_T^* upstream of the probe center can be estimated using an energy balance. In steady state, the heat conducted upstream (through both the substrate and the fluid) is balanced by that convected downstream by the fluid. The net convection of heat between a location L_T^* upstream of the probe and the location of the probe center is of the order of:

$$\frac{Q}{A} \sim \rho c U \Delta T \qquad (D.1)$$

Here, T is the temperature difference between the two

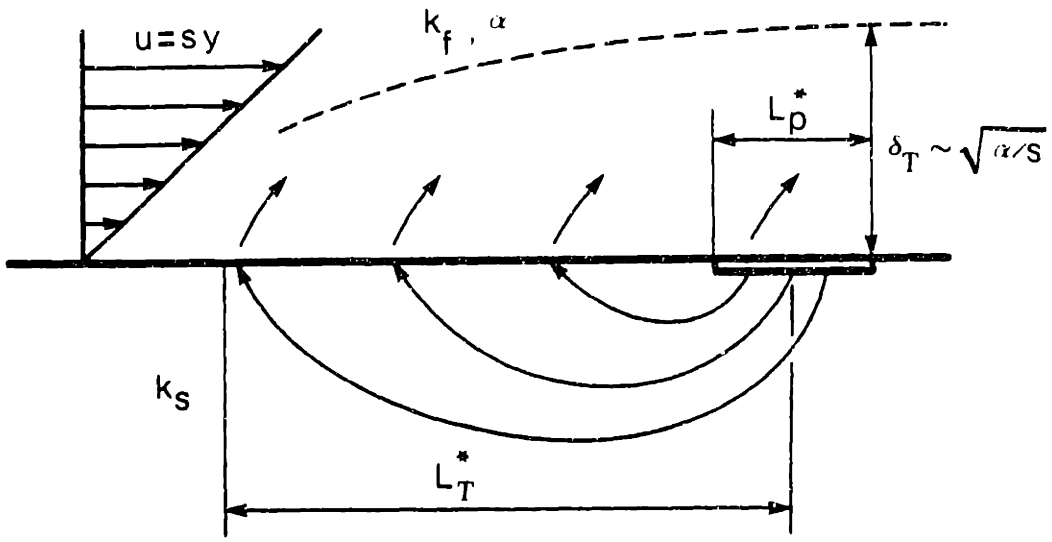

Figure D.1 Scaling of the upstream thermal penetration length for a substrate of homogeneous conductivity.

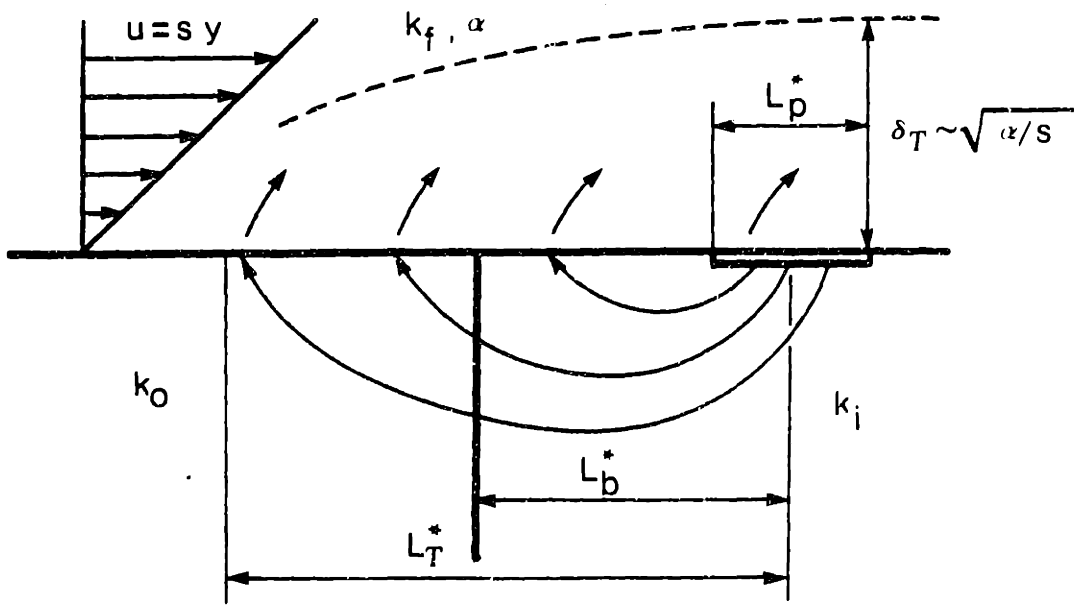

Figure D.2 Scaling of the upstream thermal penetration length for a substrate possessing a step change in conductivity.

locations and U is the velocity characteristic of this convection. Let us take U to be a velocity characteristic of the thermal boundary layer - i.e., the velocity at $y = \sqrt{\alpha/s}$. Then U is proportional to $(\sqrt{\alpha/s})(s) = \sqrt{\alpha s}$, or

$$\frac{Q}{A} \sim \rho c \sqrt{\alpha s}\, \Delta T \tag{D.2}$$

If we consider simple one-dimensional conduction from the probe a distance L_T^* upstream by two parallel paths - one through the fluid and one through the substrate - we can express the net upstream heat conduction as:

$$\frac{Q}{A} \sim \left(\frac{1}{L_T^*/k_f} + \frac{1}{L_T^*/k_s} \right) \Delta T \tag{D.3}$$

Equating (D.2) and (D.3) we have:

$$L_T^* \sim \frac{k_f + k_s}{\rho c \sqrt{\alpha s}}$$

Realizing that $\alpha = k/\rho c$, rearranging, and introducing the dimensionless parameters K and Pe we finally obtain:

$$\frac{L_T^*}{L_p^*} \frac{K + 1}{\sqrt{\frac{s}{\alpha}}\, L_p^*} = \frac{K + 1}{\sqrt{Pe}} \tag{D.4}$$

The analysis for a substrate with a step change in thermal conductivity proceeds in the same mannar except that the substrate is composed of an "inner" material in the

vicinity of the probe possessing a thermal conductivity k_i and an "outer" surrounding material further upstream with conductivity k_o. The boundary between these two conductivities is located a distance L_b^* upstream of the probe center. We investigate the substrate surface temperature a distance $L_T^* > L_b^*$ upstream of the probe center. Equation (D.2) for the convective heat transfer remains the same. The upstream conduction of heat again occurs via two parallel paths -- one in the fluid and one in the substrate. However, the substrate path is now broken into two parts in series: that through each of the regions of conductivity k_i and k_o. Thus the conduction heat transfer can be estimated to be:

$$\frac{Q}{A} \sim \left(\frac{1}{L_T^*/k_f} + \frac{1}{L^*_b/k_i + (L_T^* - L_b^*)/k_o} \right) \Delta T \qquad (D.5)$$

Equating (D.2) and (D.5) and rearranging terms in the same way as done for the homogeneous substrate case, we find

$$\frac{L_T^*}{L_p^*} \sim \frac{1}{\sqrt{Pe}} \left(1 + \frac{L^*_T}{\frac{L_b^*}{K_i} + \frac{L_T^* - L_b^*}{K_o}} \right) \qquad (D.6)$$

where K_i and K_o are the conductivity ratios formed with substrate conductivities k_i and k_o, respectively. Expressions (D.4) and (D.6) have the same form if the second term in the parentheses of (D.6) is defined to be some effective

conductivity ratio weighted by the relative influences of the two substrate materials on the heat transfer process. This approach is taken and expanded upon in Section 4.3.

E. Table of Predicted Nusselt Numbers

In this Appendix we provide a complete tabulation of the results of our parametric study of Nusselt number for rectangular probes. Also presented are tables of the flow-sensitive portion of the predicted probe Nusselt number and Nusselt number predictions based on approximation (4.10).

Table E.1 Predicted probe Nusselt numbers for zero flow - i.e., $Nu(Pe = 0, K = 0) = Nu_{00}$

b/a	Nu_{00}
0.5	3.08
0.7	2.55
1.0	2.11
2.0	1.54
5.0	1.10
8.0	0.95
∞	—

$$Nu(Pe = 0, K) = (K + 1)Nu_{00}$$

Table E.2 Predicted total probe Nusselt numbers - list.

("99" denotes b/a = ∞)

Pe	K	b/a	Nu
4.0000	0.0	1.0	2.63
16.0000	0.0	1.0	3.19
36.0000	0.0	1.0	3.75
64.0000	0.0	1.0	4.28
144.0000	0.0	1.0	5.28
256.0000	0.0	1.0	6.20
16.0000	0.0	0.5	4.14
16.0000	0.0	2.0	2.73
16.0000	0.0	5.0	2.48
16.0000	0.5	1.0	4.30
16.0000	1.0	1.0	5.41
16.0000	5.0	1.0	14.00
144.0000	0.0	99.0	4.64
4.0000	1.0	1.0	4.79
64.0000	1.0	1.0	6.53
4.0000	0.0	2.0	2.11
64.0000	0.0	2.0	3.88
144.0000	0.0	2.0	4.92
64.0000	5.0	1.0	15.24
144.0000	1.0	1.0	7.54
144.0000	0.0	5.0	4.73
144.0000	0.0	0.5	6.09
16.0000	1.0	2.0	4.35
16.0000	1.0	99.0	3.20
16.0000	1.0	5.0	3.67
16.0000	1.0	0.5	7.33
16.0000	1.0	0.7	6.26
16.0000	4.1	8.0	6.57
64.0000	4.1	8.0	7.82
4.0000	5.0	1.0	13.32
64.0000	10.0	1.0	25.96
1.0000	1.0	1.0	4.46
16.0000	5.0	2.0	10.64
0.0625	1.0	1.0	4.26
0.0625	0.0	2.0	1.59
0.0625	0.0	1.0	2.17
16.0000	10.0	1.0	24.60
16.0000	5.0	0.5	19.80
16.0000	5.0	5.0	8.20
16.0000	0.5	0.5	5.74
16.0000	0.5	5.0	3.08
16.0000	5.0	99.0	5.94
16.0000	0.5	99.0	2.79
64.0000	0.0	99.0	3.56
16.0000	0.2	1.0	3.62
16.0000	0.2	5.0	2.72
16.0000	0.2	99.0	2.53
1.0000	0.0	99.0	1.22
0.0625	0.0	99.0	0.80
0.4096	0.0	99.0	1.04
4.0000	0.0	99.0	1.64
16.0000	0.0	99.0	2.35
400.0000	0.0	99.0	6.44
64.0000	11.0	5.0	16.27
144.0000	11.0	5.0	17.43
16.0000	11.0	5.0	14.83
1.0000	0.0	1.0	2.35
1.0000	0.0	2.0	1.80
1.0000	5.0	1.0	12.86
0.0625	5.0	1.0	12.59
64.0000	20.0	1.0	46.91
64.0000	5.0	99.0	7.44
144.0000	5.0	99.0	8.63
144.0000	10.0	99.0	11.94
64.0000	10.0	99.0	10.58
16.0000	20.0	1.0	45.55
256.0000	5.0	99.0	9.66
256.0000	5.0	1.0	17.33
256.0000	10.0	99.0	13.10
16.0000	50.0	1.0	108.00
256.0000	50.0	1.0	112.30
256.0000	50.0	99.0	34.41
16.0000	10.0	99.0	8.23
64.0000	50.0	99.0	30.04

Table E.3 Predicted total probe Nusselt numbers - tabulation.

aspect ratio= 0.50000

pe/k	0.00	0.20	0.50	1.00	4.10	5.00	10.00	11.00	20.00	50.00
0.0625	0.00	0.00	0.00	0.00	0.00	0.00	0.00	0.00	0.00	0.00
0.4096	0.00	0.00	0.00	0.00	0.00	0.00	0.00	0.00	0.00	0.00
1.0000	0.00	0.00	0.00	0.00	0.00	0.00	0.00	0.00	0.00	0.00
4.0000	0.00	0.00	0.00	0.00	0.00	0.00	0.00	0.00	0.00	0.00
16.0000	4.14	0.00	5.74	7.33	0.00	19.80	0.00	0.00	0.00	0.00
36.0000	0.00	0.00	0.00	0.00	0.00	0.00	0.00	0.00	0.00	0.00
64.0000	0.00	0.00	0.00	0.00	0.00	0.00	0.00	0.00	0.00	0.00
144.0000	6.09	0.00	0.00	0.00	0.00	0.00	0.00	0.00	0.00	0.00
256.0000	0.00	0.00	0.00	0.00	0.00	0.00	0.00	0.00	0.00	0.00
400.0000	0.00	0.00	0.00	0.00	0.00	0.00	0.00	0.00	0.00	0.00

aspect ratio= 0.70000

pe/k	0.00	0.20	0.50	1.00	4.10	5.00	10.00	11.00	20.00	50.00
0.0625	0.00	0.00	0.00	0.00	0.00	0.00	0.00	0.00	0.00	0.00
0.4096	0.00	0.00	0.00	0.00	0.00	0.00	0.00	0.00	0.00	0.00
1.0000	0.00	0.00	0.00	0.00	0.00	0.00	0.00	0.00	0.00	0.00
4.0000	0.00	0.00	0.00	0.00	0.00	0.00	0.00	0.00	0.00	0.00
16.0000	0.00	0.00	0.00	6.26	0.00	0.00	0.00	0.00	0.00	0.00
36.0000	0.00	0.00	0.00	0.00	0.00	0.00	0.00	0.00	0.00	0.00
64.0000	0.00	0.00	0.00	0.00	0.00	0.00	0.00	0.00	0.00	0.00
144.0000	0.00	0.00	0.00	0.00	0.00	0.00	0.00	0.00	0.00	0.00
256.0000	0.00	0.00	0.00	0.00	0.00	0.00	0.00	0.00	0.00	0.00
400.0000	0.00	0.00	0.00	0.00	0.00	0.00	0.00	0.00	0.00	0.00

Table E.3 Continued

aspect ratio= 1.00000

pe/k	0.00	0.20	0.50	1.00	4.10	5.00	10.00	11.00	20.00	50.00
0.0625	2.17	0.00	0.00	4.26	0.00	12.59	0.00	0.00	0.00	0.00
0.4096	0.00	0.00	0.00	0.00	0.00	0.00	0.00	0.00	0.00	0.00
1.0000	2.35	0.00	0.00	4.46	0.00	12.86	0.00	0.00	0.00	0.00
4.0000	2.63	0.00	0.00	4.79	0.00	13.32	0.00	0.00	0.00	0.00
16.0000	3.19	3.62	4.30	5.41	0.00	14.00	24.60	0.00	45.55	108.00
36.0000	3.75	0.00	0.00	0.00	0.00	0.00	0.00	0.00	0.00	0.00
64.0000	4.28	0.00	0.00	6.53	0.00	15.24	25.96	0.00	46.91	0.00
144.0000	5.28	0.00	0.00	7.54	0.00	0.00	0.00	0.00	0.00	0.00
256.0000	6.20	0.00	0.00	0.00	0.00	17.33	0.00	0.00	0.00	112.30
400.0000	0.00	0.00	0.00	0.00	0.00	0.00	0.00	0.00	0.00	0.00

aspect ratio= 2.00000

pe/k	0.00	0.20	0.50	1.00	4.10	5.00	10.00	11.00	20.00	50.00
0.0625	1.59	0.00	0.00	0.00	0.00	0.00	0.00	0.00	0.00	0.00
0.4096	0.00	0.00	0.00	0.00	0.00	0.00	0.00	0.00	0.00	0.00
1.0000	1.80	0.00	0.00	0.00	0.00	0.00	0.00	0.00	0.00	0.00
4.0000	2.11	0.00	0.00	0.00	0.00	0.00	0.00	0.00	0.00	0.00
16.0000	2.73	0.00	0.00	4.35	0.00	10.64	0.00	0.00	0.00	0.00
36.0000	0.00	0.00	0.00	0.00	0.00	0.00	0.00	0.00	0.00	0.00
64.0000	3.88	0.00	0.00	0.00	0.00	0.00	0.00	0.00	0.00	0.00
144.0000	4.92	0.00	0.00	0.00	0.00	0.00	0.00	0.00	0.00	0.00
256.0000	0.00	0.00	0.00	0.00	0.00	0.00	0.00	0.00	0.00	0.00
400.0000	0.00	0.00	0.00	0.00	0.00	0.00	0.00	0.00	0.00	0.00

Table E.3 Continued

aspect ratio= 5.00000

pe/k	0.00	0.20	0.50	1.00	4.10	5.00	10.00	11.00	20.00	50.00
0.0625	0.00	0.00	0.00	0.00	0.00	0.00	0.00	0.00	0.00	0.00
0.4096	0.00	0.00	0.00	0.00	0.00	0.00	0.00	0.00	0.00	0.00
1.0000	0.00	0.00	0.00	0.00	0.00	0.00	0.00	0.00	0.00	0.00
4.0000	0.00	0.00	0.00	0.00	0.00	0.00	0.00	0.00	0.00	0.00
16.0000	2.48	2.72	3.08	3.67	0.00	8.20	0.00	14.83	0.00	0.00
36.0000	0.00	0.00	0.00	0.00	0.00	0.00	0.00	0.00	0.00	0.00
64.0000	0.00	0.00	0.00	0.00	0.00	0.00	0.00	16.27	0.00	0.00
144.0000	4.73	0.00	0.00	0.00	0.00	0.00	0.00	17.43	0.00	0.00
256.0000	0.00	0.00	0.00	0.00	0.00	0.00	0.00	0.00	0.00	0.00
400.0000	0.00	0.00	0.00	0.00	0.00	0.00	0.00	0.00	0.00	0.00

aspect ratio= 8.00000

pe/k	0.00	0.20	0.50	1.00	4.10	5.00	10.00	11.00	20.00	50.00
0.0625	0.00	0.00	0.00	0.00	0.00	0.00	0.00	0.00	0.00	0.00
0.4096	0.00	0.00	0.00	0.00	0.00	0.00	0.00	0.00	0.00	0.00
1.0000	0.00	0.00	0.00	0.00	0.00	0.00	0.00	0.00	0.00	0.00
4.0000	0.00	0.00	0.00	0.00	0.00	0.00	0.00	0.00	0.00	0.00
16.0000	0.00	0.00	0.00	0.00	6.57	0.00	0.00	0.00	0.00	0.00
36.0000	0.00	0.00	0.00	0.00	0.00	0.00	0.00	0.00	0.00	0.00
64.0000	0.00	0.00	0.00	0.00	7.82	0.00	0.00	0.00	0.00	0.00
144.0000	0.00	0.00	0.00	0.00	0.00	0.00	0.00	0.00	0.00	0.00
256.0000	0.00	0.00	0.00	0.00	0.00	0.00	0.00	0.00	0.00	0.00
400.0000	0.00	0.00	0.00	0.00	0.00	0.00	0.00	0.00	0.00	0.00

Table E.3 Continued

aspect ratio= 99.00000

pe/k	0.00	0.20	0.50	1.00	4.10	5.00	10.00	11.00	20.00	50.00
0.0625	0.80	0.00	0.00	0.00	0.00	0.00	0.00	0.00	0.00	0.00
0.4096	1.04	0.00	0.00	0.00	0.00	0.00	0.00	0.00	0.00	0.00
1.0000	1.22	0.00	0.00	0.00	0.00	0.00	0.00	0.00	0.00	0.00
4.0000	1.64	0.00	0.00	0.00	0.00	0.00	0.00	0.00	0.00	0.00
16.0000	2.35	2.53	2.79	3.20	0.00	5.94	8.79	0.00	0.00	0.00
36.0000	0.00	0.00	0.00	0.00	0.00	0.00	0.00	0.00	0.00	0.00
64.0000	3.56	0.00	0.00	0.00	0.00	7.44	10.58	0.00	0.00	30.04
144.0000	4.64	0.00	0.00	0.00	0.00	8.63	11.94	0.00	0.00	0.00
256.0000	0.00	0.00	0.00	0.00	0.00	9.66	13.10	0.00	0.00	34.41
400.0000	6.44	0.00	0.00	0.00	0.00	0.00	0.00	0.00	0.00	0.00

F. Reduction of Theory to Limiting Value Expressions

In this Appendix, we first reformulate our governing equations such that the probe streamwise length rather than the thermal diffusion length is used as the characteristic length for nondimensionalization. With this formulation, the Peclet number appears explicitly in the solution in wavenumber space allowing the limiting value behavior as Pe approaches zero or infinity to be more easily obtained. (A disadvantage of this formulation is that the fluid energy equation is less general in that the Peclet number appears in it as a parameter.) We then present the limiting value behavior.

The set of dimensionless governing equations utilizing L_p^* as the characteristic length dimension are then simply (2.11) and (2.7)-(2.10) - where (2.7)-(2.10) are based on the probe length as the length scale. Following the same procedure as in Section 2.2, Fourier transformation is carried out in the x and z dirctions. Equations (2.15)-(2.18) remain the same, and (2.14) is replaced by

$$\hat{T}_f'' - 4\pi^2\left(p^2+q^2 - i\,\frac{pPe}{2\pi}\,y\right)\hat{T}_f = 0 \qquad \text{(F.1)}$$

The change of independent variable analogous to (2.19) is:

$$\eta = e^{-\pi i/6}(2\pi pPe)^{1/3}\left(y + i\,2\pi\,\frac{p^2+q^2}{pPe}\right) \qquad \text{(F.2)}$$

Use of (F.2) in (F.1) again produces (2.20). Solution of this set of equations in wavenumber space again produces (2.27) and (2.28), but (2.29) is replaced by:

$$\hat{T}_o = \frac{\hat{Q}}{K \cdot 2\pi\sqrt{p^2+q^2} - e^{-\pi i/6}(2\pi p Pe)^{1/3}\dfrac{Ai'(\eta_o)}{Ai(\eta_o)}} \qquad (F.3)$$

where η is given by (F.2) and η_o is found by evaluating (F.2) at y=0:

$$\eta_o = \eta_{y=0} = e^{\pi i/3}(2\pi)^{4/3}\frac{p^2+q^2}{p^{2/3}\,Pe^{2/3}} \qquad (F.4)$$

The limiting value behavior of the ratio of the Airy function to its derivative is given in Abramowitz and Stegun (1972) as:

$$\frac{Ai(0)}{Ai'(0)} = -1.3717\ldots \equiv A_0 \qquad (F.5)$$

$$\frac{Ai(z)}{Ai'(z)} \sim -\frac{1}{\sqrt{z}} \quad \text{as } z \to \infty \qquad (F.6)$$

For large values of K, the first term in the denominator of (F.3) dominates the second, and (F.3) reduces to:

$$\hat{T}_o = \frac{\hat{Q}}{2\pi K\sqrt{p^2+q^2}} \qquad (F.7)$$

For small values of Pe, the argument of the Airy functions (F.4) becomes large and using (F.6), expression (F.3) reduces

to:

$$\frac{\hat{}}{T_0} = \frac{\hat{Q}}{2\pi (K+1)\sqrt{p^2+q^2}} \qquad \text{(F.8)}$$

This is the case of pure conduction in both the fluid and the solid. Expression (F.7) represents pure conduction in the substrate alone - the fluid being neglected. These are the same expressions obtained if one starts with the the energy equations for zero flow as is done in Section 2.5. The approach used in Section 2.5 leads to a convolution integral. However, if the governing equations in physical space for pure conduction in two adjacent media are first transformed and then solved in wavenumber space, (F.8) is obtained identically. The solutions to the resulting differential equations in wavenumber space would both be of the form of (2.22) before application of boundary conditions.

As Pe becomes large, η_0 approaches zero, (F.5) applies, and the first term in the denominator of (F.3) can be neglected. (F.3) then reduces to:

$$\frac{\hat{}}{T_0} = \hat{Q} \cdot \frac{-e^{\pi i/6} A_0}{(2\pi p)^{1/3} Pe^{1/3}} \qquad \text{(F.9)}$$

This leads to the dependence of the Nusselt number on the one-third power of the Peclet number at sufficiently large Pe as is seen here:

$$\hat{T}_0 \sim \frac{1}{Pe^{1/3}}$$

$$Nu \sim \frac{1}{\bar{T}_p} \sim \frac{1}{T_0}$$

$$T_0 \sim \hat{T}_0$$

$$Nu \sim Pe^{1/3}.$$